UNIVERSITY OF CALIFORNIA, SAN DIEGO

3D printing of Static and Hybrid Dynamic Biomaterial Scaffolds for Tissue Engineering

A dissertation submitted in partial satisfaction of the requirements for the degree Doctor of Philosophy

in

Nanoengineering

by

John Jamison Warner

Committee in charge:

Professor Shaochen Chen, Chair
Professor Michael Heller, Co-Chair
Professor Shengqiang Cai
Professor Zhaowei Liu
Professor Liangfang Zhang

2017

The Dissertation of John Jamison Warner is approved, and it is acceptable in quality and form for publication on microfilm and electronically:

_____

_____

_____

_____
Co-Chair

_____
Chair

University of California, San Diego

2017

DEDICATION

To a lifetime of mentors young and old, that provided the resources and skills towards this endeavor and to those who challenged me, strengthening my resolve and making them mentors after all; I am truly fortunate for both.

EPIGRAPH

Do not rely on following the degree of understanding that you have discovered, but simply think, *This is not enough*.

Tsunetomo Yamamoto

TABLE OF CONTENTS

LIST OF FIGURES

LIST OF TABLES

ACKNOWLEDGEMENTS

I would like to acknowledge Professor Shaochen Chen for support as the chair of my committee. His guidance in academic research and his understanding of such audiences has proved to be invaluable.

I would also like to acknowledge Professor Michael Heller as co-chair of my committee. His guidance in preparing his students for industry has improved my perspective.

I would also like to acknowledge the previous Nanoengineering chair, Professor Ken Vecchio, without whom my research could not have been completed without access to his NEMRC facility and its personnel, Sabine Faulhaber, Wayne Nelson, and Tyler Harrington. It is their support that helped me in an immeasurable way.

I would like to acknowledge all of the Nanoengineering graduate office support staff and safety officers that provided the infrastructure and logistics for the Nanoengineering program, whom are rarely thanked. Specifically, I must thank Tara Slaughter for trudging through the early dysfunctional procurement system with me to acquire the equipment required to setup Dr. Chen's laboratory in a reasonable timeframe. I must also acknowledge Keiko Scott and Satomi Saito for their help with this and patience fixing it. I thank Carolynn Sheehan for her trust in letting me set up the second new laboratory in SME. I thank Renee Gramlich for working with me to find weaknesses in the early Nano curriculum. However I am most fortunate for Dana Jimenez, who always fought for me, always had my back, and always kept me on track.

I must in good conscience acknowledge my wife for her support of this endeavor and staying by my side despite the stress and disappointments, while reminding me to celebrate my accomplishments.

Chapter 2, in full, is a reprint of the material as it appears in Warner, John; Soman, Pranav: Zhu, Wei; Tom, Matthew; Chen, Shaochen, “Design and 3D Printing of Hydrogel Scaffolds with Fractal Geometries”, ACS Biomaterials Science & Engineering, vol. 8, 2015. The dissertation author was the primary investigator and author of this paper.

Chapter 3, in full, has been submitted for publication of the material as it may appear in Warner, John; Wang, Pengrui; Mellor, William M.; Hwang, Henry H.; Pyo, Sang-Hyun, Chen, Shaochen, “A Photopolymerizable and Composition Tunable Polyurethane with Green ‘Click’ Chemistry.” The dissertation author was the primary investigator and author of this paper.

Chapter 4, in full, is currently being prepared for submission for publication of the material. Warner, John; Gillies, Allison; Hwang, Henry H.; Zhang, Hong; Lieber, Richard L.; Chen, Shaochen, “Printed Biomaterials with Regional Auxetic Properties”. The dissertation author was the primary investigator and author of this material.

VITA

Professional Experience

Consultant: Angel Investment Technology Assessment	2014
Consultant: Genentech-Roche: FDA Response	2012
Consultant: HLPC resin synthesis / manufacturing	2010
Genentech-Roche	2005-2009
Biogen	2004-2005
IDEC Pharmaceuticals	2002-2004
UC BERKELEY, Nutritional Science Toxicology Lab (Vulpe Lab)	2000

Education and Training

Degrees:

PhD. Nanoengineering, University of California, San Diego	2017
M.S. Nanoengineering, University of California, San Diego	2012
B.S. Molecular Cell Biology, University of California, Berkeley	2001

Technical Training:

Micro MBA Program (Rady's Business School)	2013
Protein Formulation	2007
Protein Characterization	2007
HPLC design (Chromatography Institute of America)	2004
Statistical Analysis (Statistical Designs)	2003

Management Training:

Project Management (PMBOK®)	2008
Crucial Conversations	2008

ABSTRACT OF THE DISSERTATION

3D Printing of Static and Hybrid Dynamic Biomaterial Scaffolds for Tissue Engineering

by

John Jamison Warner

Doctor of Philosophy in Nanoengineering

University of California, San Diego, 2017

Professor Shaochen Chen, Chair

Professor Michael Heller, Co-Chair

Fueled by research that biological cells respond strongly to physical cues as well as to molecular signals, we used continuous projection stereo lithography to create 3D printed biomaterial scaffolds for mammalian cells. Relying on the high resolution and flexibility of our system, we demonstrate the utility of transferring complex designs into various photopolymerizable materials. This capability affords us the opportunity to mimic natural structures. Under certain circumstances, some natural structures which represent optimized configurations created by physical processes occurring in one medium are able to be transferred to another material, thus conferring these

attributes to a new environment. This fabrication method has also been implemented in creating dynamic multilayer auxetic mesh skeleton structures to similarly convey counter-intuitive negative Poisson's ratio manipulations of force and movement to an outer-skin material absent of such characteristics. We also show the versatility in spatially patterning various biomaterials to both localize and couple multiple material properties including adhesive hydrogels and modular green-chemistry polyurethanes. Based on this data, pattern complexity may be useful in helping understand simple underlying trends behind cell organization, mechanical energy storage of tendon models, and choosing materials for biomaterial scaffolds.

Chapter 1: Printing Biomaterial Scaffolds for Tissue Replacement

Biological cells respond to geometric cues, as well as to biochemical and mechanical stimuli[1–4]. Recent progress in micro- and nano-technology has allowed researchers to create simple microtopographies that can be used to examine the effect of geometric cues on cellular behavior[5,6]. Knowledge of changes in cell mechanics and morphology in response to geometric cues is important for understanding the basic behavior of cells during development and pathological processes. With such information, tissue engineering directed towards creating artificial complex organs and consistent controlled organ-system models is closer to realization. Current methods resort to harvesting[7] tissue with few synthetic options, however understanding geometric cues enables us to build biomaterial constructs for tissue models and eventually tissue replacement.

Some weaknesses in the current model of standardized medicine are being increasingly addressed by the concept of individualized medicine, which may better accommodate more efficient and less toxic patient treatment. However with this transition, efficiency priorities must also shift. Currently, cost per treatment and length of stay are primary metrics. However, because individualized medicine requires higher complexity solutions in terms of delivering treatment and diagnosis, higher initial operating costs with more permutations of individualized drugs are likely predicted. This focus moves the emphasis of efficiency towards longer term goals, such as engineering more

flexible products to meet the specifics of each patient and repairing aliments rather than merely treating symptoms.

Gene therapy, epigenetic modification, and microflora replacement are ideal means of utilizing the body's machinery to repair itself. However for mechanic-like repair, few can argue that replacement tissue is not advantageous. 3D fabrication methods capable of generating multiple specific "perfect" pieces from a "common" stock material match the concepts found in personalized medicine and avoid the potential for large "dead" inventories and wasted or expired material. As an example, a minimum stock of every replacement part need not be kept if you can 3D print those specific pieces.

The source and means of acquiring such replacement tissue is often a moral debate. However steps towards tissue regeneration, such as tissue replacement and tissue models for drug testing and diagnostics, provide a means to help the aging population live more productive and potentially more fulfilling lives that otherwise might be met with debilitation. Using biomaterials to replace tissue and provide individualized tissue models for testing, biomaterial scaffolding can provide more specific ways to extend the functional life of people.

Cells require organization to facilitate tissue formation, and the majority of cell types show increased viability when attached to a scaffold. We anticipate the physical cues provided by micro-topographies of 3D printed biomaterial scaffolds with tunable stiffness as the best, although most infantile, means to create synthetic scaffolds for cost effective implementation. Organ

transplants are often limited by availability and allogenic rejection criteria (MHC/HLA matching). Advancements using intact decellularized organ extra-cellular matrix (ECM) seeded with autologous cells as a transplant organ, provide exceptional promise, but also at exceptional cost. This methodology directs scientists towards one inevitable pathway of intense moral and ethical debate of organ harvesting initially from animals, however as an extreme measure, possibly using cloned human parts or chimeras. Because of these reasons, synthetic scaffold technology needs to be explored more thoroughly. Figure 1.1 visually explains this concept with a rudimentary vision of mimicking portions of natural tissue via synthetic or “designed” methods, and reintegrating these structures, coatings, and cell mixtures together to create a functioning artificial tissue.

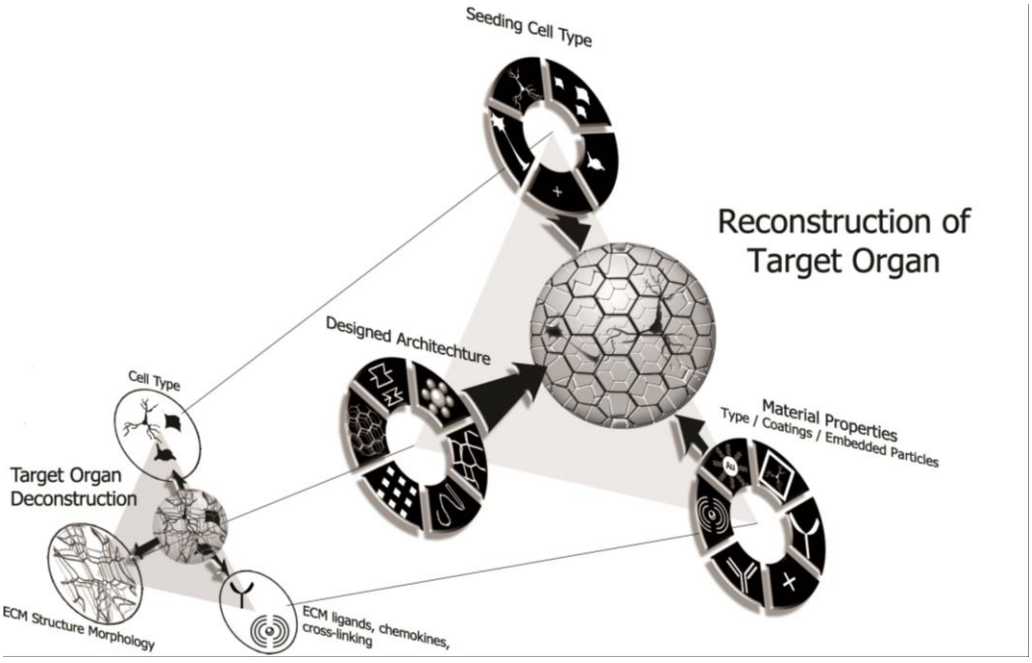

Figure 1.1: Illustration of a concept of tissue deconstruction for systematic synthetic reconstruction. Natural tissues are compartmentalized into synthetic “controllable” equivalents for reassembly into a reconstructed designed organ.

1.1 Cell Dependence on Simple Physical Cues

Cell scaffolds are important because physical cues in the immediate nano- and micro-environments affect cell fate and function. Although signaling molecules are an integral component of nearly all signaling cascades affecting gene regulation, which result in differentiation, a portion of these role modifying pathways may be initiated or influenced by physical means alone. Solely altering physical cues such as topography has been shown to facilitate cell alignment, positioning, loading capacity, migration, survivability and effect proliferation[2,3,6]. Simply varying the stiffness of bulk material is one method being used to differentiate progenitor cells; the mechanism seems to involve strain sensitive mechano-proteins (talin / viculin) found at focal adhesion sites near the cell exterior, which inevitably lead to later transcription events[3]. Consequently, two major components of cell behavior 1) growth (proliferation / migration) and 2) differentiation can be modified merely by various physical stimuli. As such, these components are the primary means to utilize with synthetic scaffolds.

1.2 Scaffolds to Mimic the Desired Cellular Environment

Areas of regenerative medicine take advantage of this localized phenomenon, seeking to mimic native cell microenvironments to achieve organized cell function appropriate for natural tissues or organs. This has been most notably achieved through reusing natural (i.e., allogenic) organ scaffolds. In 2007, a functional rat heart valve was recreated in a bioreactor from a

decellularized heart extracellular matrix and seeded cells[8]. Although complex organs still require a natural decellularized ECM template, simpler organs (i.e. bladder) have been created with completely artificial scaffolds. Spin-off theories involve mimicking early developmental forms of the tissue or organ to facilitate the nascent flexibility of cells to more seamlessly integrate with repaired tissue. Provided that natural "early-development" scaffolds or matrices will be more difficult or unavailable to isolate due to ethical and technical constraints, there may exist a stronger need to attune artificial scaffolds to create such conditions. Additionally, faster and more flexible tools may be desirable to facilitate the many permutations required to create such nascent cellular environments for influencing cell behavior.

1.3 Materials to Mimic Potential Forces in Cellular Environments

Materials for cellular scaffolds more recently tend toward polymers of various materials that exhibit elastic or less rigid behavior with highly malleable properties that can be tuned to largely mimic the native environment of cells. Hydrogels provide water absorbent elastic properties that are often biocompatible. Though many polymerizable hydrogels can be easily adapted for photo-polymerization, the feature resolutions associated with rigid materials are not obtainable (DMD-PP ~1 $x10^3$ nm, TPP ~2 $x10^2$ nm, CMOS ~19 nm). Despite this drawback, these highly porous materials can be increasingly cross-linked to vary the Young's modulus and pore size over the entirety of the bulk. In addition, due to the ability for photo-polymerization, these materials

are conducive for building mechanical structures from patterns of light or light-based templates. Examples include: polyethylene glycol diacrylate (PEGDA), colagen, gelatin, hyluronic acid, and gelatin methacrylate (GelMa) polyacryalmide.

1.4 Dynamic Mechanical Structural Patterns

Scaffolds need not be passive or static. Some experiments show that pulsatile tension and fluid flow can encourage interconnection and alignment of cells[9]. Individual cell studies observe that tension force exerted on a cell is transmitted throughout the cell via the cytoskeletal elements. Microtubules, a portion of the cytoskeletal network, happen to connect cell junctions[10], so this provides intuitive support for how mechano-pulsation may interact with biological pathways to increase cell junctions[11], and thus increase cell-cell connectivity and interaction leading to tissue formation.

Many biomaterials used for scaffolds are polymers created in bulk. We can impose a more complex superstructure to modulate force without affecting the elasticity of the bulk material. Structurally dynamic scaffolds can be used in place of slabs, if the architecture is sufficiently small. Implementing a dynamic structure provides an extra layer of customization to mimic biological systems, or optimize a material for a particular biological role. Internal and external physical forces can be made more uniform, concentrated, mitigated, redirected, or coupled to perform alternate tasks. This allows the structure to be a preprogrammed tool for the user to control stress. As an example, the

easiest way to stretch a cell is not using nano-tweezers. Due to the small area and forces involved, this may tear the cell. Optical trapping via light tweezers or microclamping might be more suitable, though may be time prohibitive when dealing with a tissue composed of a million or more cells. Imbuing scaffolds with dynamic properties to affect “systems” of cells instead of individual cells is sometimes more favorable.

Most previous research in this area has focused on cell responses to two-dimensional simple structures because of the difficulty of fabricating such microstructures. Mask-less dynamic optical projection stereolithography (DOPsL) printing was chosen over other technologies because of design and material flexibilities for numerous micro-geometric cues, localized stiffness moduli, biocompatibility, and scalability[12,13]. The flexibility is attributed to the digital mask-less design with the scalability for production arising from the parallel projection methodology. This additive manufacturing process provides more flexibility than contact-based physical stamps or moulds that often require ion milling at some point in the mask fabrication process, which makes template tunability expensive and slow. Despite a ~10+ fold resolution advantage and innate 3D polymerization confinement, two-photon lithography is less ideal because of instrument cost and the relatively slow serial light-writing method. Scale-up, given the current state of technology is expensive, if created in parallel without two-photon hologram polymerization[14]. Inkjet printing is closer in comparison, providing faster fabrication times than other serial methods and has some advantages in creating 3D structures with

overhanging features. However the system still requires printing temporary supports, microfluidics delivery, slower scale-up while maintaining resolution, and shows more difficulty with increasingly viscous polymer materials. Materials were chosen to facilitate photo-fabrication on the DOPsL platform and localize stress moduli conducive to cell objectives using hydrogels, polyurethane acrylates, polyurethane thiol-ene, and DNA.

1.5 Fabrication of Hydrogel/PU/DNA Structures

Scaffolds can be produced via photo-polymerization. As alluded to, these fabrication methods utilize light to spatially localize polymerization within a liquid gel. Two notable methods to achieve direct photo polymerization include 1) using a Digital Mirror Device (DMD) for spatial light modulation as a digital template or “virtual mask” for nano-projection printing and 2) exploiting two photon polymerization (2PP) characteristics of a condensed Ti-sapphire pulse laser beam to draw a structure. Both DMD projection printing (DMD-PP) and 2PP can use polymers which can be optimized through varying concentrations of photoinitiator, quencher, and absorber to achieve desired fabrication results.

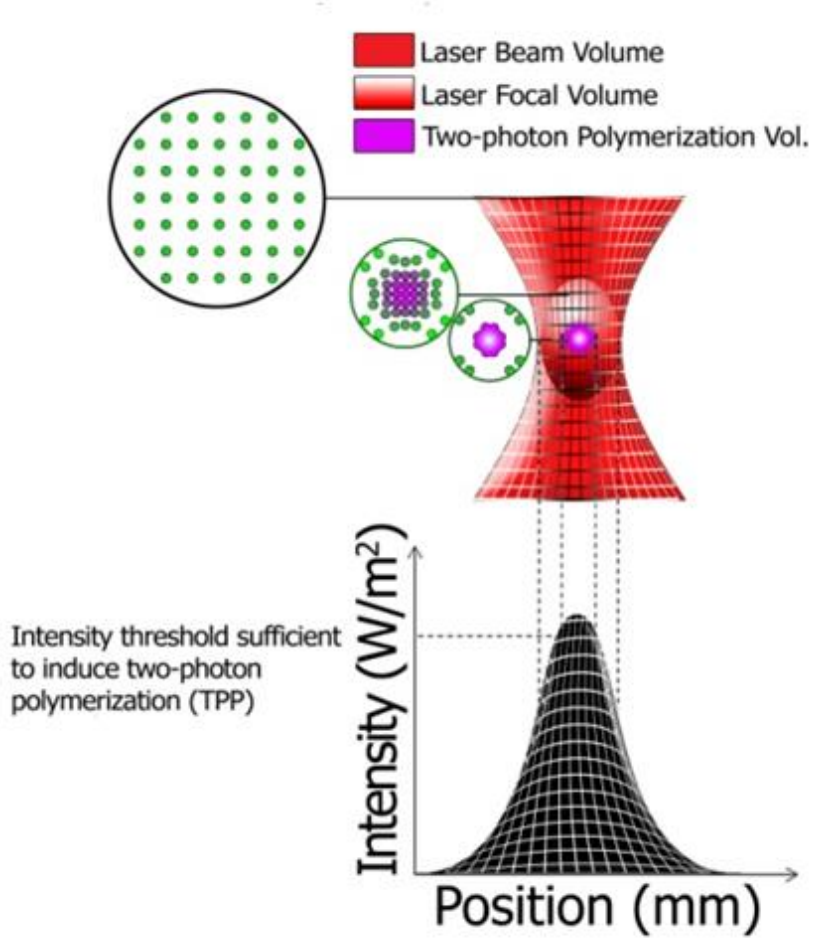

Figure 1.2: Two Photon Polymerization (2PP) volume of pulse laser beam with associated photon density cross-sectional z-stack correlated to intensity and position.

The key differences in the technologies are speed, resolution, and the method of construction of multilayer or 3D segments. The DMD-PP fabricates scaffolds as layer cross-sections relatively quickly in parallel production fashion due to the image projection photopolymerization method employed. The scaffold materials are constrained to energy in the UV-visible spectrum of light currently tolerated by the DMD chip responsible for the maskless design of DOPsL. The digital image mask generated by the DMD can be electrically changed to virtually any 2D image slice of 1920 x 1080 pixels in fractions of a

second, which eliminates the need for more expensive and slower to produce masks. The 2PP is slower because the design is currently limited to serial fabrication. The focal point of the laser draws the structure thus requiring complete harmonization of relative speed, movement, and energy intensity. However, as seen in Figure 1.2, 2PP has a higher resolution for the same wavelength of light as DOPsL. The two-photon event is probabilistic based on spatial and temporal location of one photon relative to another photon in the same phase. 2PP appears as a threshold event at a certain density along a normal distribution, normally only achieved within the focal point of a pulse laser. The higher energy from a 2PP event can be absorbed by a photoinitiator molecule, which is normally unaffected by lower wavelength energy. Though this resolution can be substantially higher, current constraints of materials require less energetic light normally used in the DMD-PP.

The DMD-PP is capable of multilayer construction of 3D scaffolds or simple 3D layers and is readily scalable and relatively easy because template directed layer polymerizing occurs simultaneously. Comparatively, 2PP can be focused more precisely within a focal plane, therefore is capable of more complex designs (hollowed features). However, more careful consideration of the order of construction must be taken when using softer materials as there exists an increased potential of collapse or shifting under the structures own weight, when building in a serial fashion.

Using the DMD-PP methodology, we demonstrate a high resolution fabrication method capable of transferring optimized static patterns over

relevant scales to other mediums, transferring programmed macrostructure architectures to unit-cells in order to escape normal property constraints of bulk structures, and using of modular chemistries to further increase the elastomeric property localization of biomaterial scaffolds for cells.

Scaffold microtopography has been relatively underexplored and remains poorly understood, despite the fact that it too has been shown to strongly influence cell behavior. Microgrooved substrates have been used to support the adhesion, alignment, and proliferation of various cell types, while cyclic stretching of mesenchymal stem cells on substrates enhances differentiation into vascular cells[6,15]. Pursuit of this field of expertise is required to gain underlying insight to build soft tissue replacement scaffolds and tissue models important for individualized medicine.

Chapter 2: Design and 3D Printing of Hydrogel Scaffolds with Fractal Geometries

2.1 ABSTRACT

Structures that exhibit fractal geometries are typically self-similar and iterative. Fractal patterns appear in nature as approximations of mathematical abstractions, yet exist as artifacts of specific processes having reached optimized conditions in the presence of various forces and movements. In this paper, we focus on 3D printing of fractal geometry using computer designed and user adjusted patterns. Various biocompatible hydrogel structures were printed from a photopolymerizable poly (ethylene glycol) diacrylate via maskless stereolithography. This digital micromirror device based projection printing platform is capable of imbuing fractal topographic patterns into a more cell accommodating medium. Several fractal structures were printed mimicking the energy and material pattern optimization achieved by fractal geometries found in nature. The resulting structures were confirmed with bright field and SEM microscopy. Complex geometries were obtained at many angles, and various heights that exhibited self similar geometries. The surfaces of the hydrogel structures were conjugated with fibronectin cell adhesion protein and then seeded with cells. Fluorescent staining of actin and nuclei for both murine myoblast cells and human mesenchymal stem cells were conducted to determine the feasibility of these designed cell adhesive topographies to influence aggregate cells. This flexible and versatile platform

can be extended to fabricate other complex biomimetic designs for biological applications, such as tissue engineering.

Keywords:3D printing, hydrogel, fractal, DMD, DOPsL

2.2 INTRODUCTION

Fractal geometry structures are typically iterative self-similar patterns[16,17]. Fractal patterns in nature are artifacts of conditions reached during specific processes that represent useful optimization when organizing materials with regards to forces within a specific medium[18,19]. Such natural optimization can be found in the bifurcation of lungs[19–23], wild-type and cancerous pulsatile vasculature networks[18,23–26], the columnar packing of the liver[27], and the packing of the seeds in sunflowers and pineapples[28,29]. With the ubiquitous existence of fractal patterns in nature, there has been great interest in the bioengineering field to engineer and utilize fractal patterns to study biological questions, such as identifying diseased afflicted cell growth[24–26], screening cells[21,25,30,31], and investigating cell proliferation behaviors[32,33].

Several manufacturing methods have been used to fabricate different designs of engineered fractal scaffolds, including freeze-drying[34,35], salt leaching[36,37], electrospinning[35,38], and fiber deposition[35,37]. Most of these approaches are limited to the overall control of the bulk property of the scaffold and lack the flexibility to tune the fractal design regionally and precisely. The resulting geometries from many of these conventional manufacturing methods are typically fibrous in nature, and “randomly” organized. These primary

characteristics emphasize a “roughened” surface area which improves cell growth[6,22,31] and explains the continued use in bio-applications. However, in order to fabricate geometries with precise control, micro and nano-manufacturing approaches, such as photolithography[18,22,39,40], inkjet printing[35], laser sintering[41–45], fused deposition[18,22,37], have been used instead. However, these manufacturing techniques have limitations in resolution, speed or 3D-fabrication capability. Highly complex fractal structures involving large scales can be time-consuming to fabricate with these precision manufacturing methods.

The digital micromirror device (DMD) based projection printing emerges as a high-throughput 3D micro/nano manufacturing technique, offering micrometer resolution, superior fabrication speed[46,47] and a high degree of pattern flexibility[48] and scalability. Recently, we have demonstrated a dynamic optical projection stereolithography (DOPsL) method for printing complex 3D micro-architectures[12] with various photopolymerizable materials such as poly (ethylene glycol) diacrylate (PEGDA), glycidal methacrylate-hyaluronic acid, and gelatin methacrylate[42,49]. These printed hydrogels have shown great biocompatibility for cell seeding and encapsulation[50].

Here we report the development and application of the DOPsL platform to engineer biomimicking and user-defined fractal patterns. 3D hydrogel structures were printed according to simple mathematical models and complex biomimetic fractal designs. Various structures composed of channels and ridges of varying height and width were printed for the biomimetic fractal

patterns. Murine myoblast cells were seeded on the printed fractal scaffolds to demonstrate the biocompatibility of these printed fractal scaffolds in the biological studies. With the superior flexibility and versatility of the DOPsL platform, we were able to fabricate closely packed fractal structures featuring highly complex designs.

2.3 EXPERIMENTAL SECTION:

2.3.1 Material preparation

Acrylic acid, 5-Benzoyl-4-hydroxy-2-methoxybenzenesulfonic acid (HMBS), poly (ethylene glycol) diacrylate (PEGDA, Mn = 575), and 2,2,6,6-tetramethylpiperdine 1-oxyl (TEMPO) were purchased from Sigma-Aldrich. High purity water was produced by an in-house Millipore® system with a resistivity reading 18.2 MΩ upon collection. Irgacure 651, Irgacure 819 and Irgacure 2959 were purchased from Ciba Chemistry. They are photoinitiators generating chemical free radicals when exposed to ultraviolet (UV) light. The solubility of Irgacure 651 is suitable for 100% PEGDA solution, while Irgacure 2959 is suitable for 50% PEGDA in water solution. Irgacure 819 is soluble in 100% PEGDA and has an optical profile more comparable to the UV light source used, despite being more reactive to ambient light. TEMPO mitigates free radical migration distance thus reducing structure bleeding while creating higher aspect ratio structures. HMBS absorbs UV light and increases a gradient against UV light penetration into the structure, providing a better means to control structure height. Acrylic acid polymerizes into the acrylate

polymerization chain, anchoring carboxylate functional groups for later chemical conjugation to a peptide. For the 50% PEGDA in water solution, equal volumes of PEGDA and MilliQ® water were mixed in a glass container protected from light. TEMPO [0.01% w/v], HMBS [0. 1% w/v], acrylic acid [1.0% v/v] and Irgacure 2959 [1.0% w/v] were added to the solution. The mixture was stirred with a magnetic bar while heated to 60˚C for 1-3 hours. The resulted 50% PEGDA solution was used to fabricate the structures presented in Figure 1, Figure 2, Figure 4, and Figure 5 image A. Figure 3 was printed with TEMPO [0.01% w/v], HMBS [0.1% w/v], and Irgacure 819 [1.0% w/v] to demonstrate z control of the increased polymerization penetration. For the final 100% PEGDA solution, Irgacure 651 [2.00% w/v] and TEMPO [0.04% w/v] were added to PEGDA. The resulting 100% PEGDA was used to fabricate the structure presented in Figure 4 image B.

2.3.2 DOPsL system setup

Figure 1A shows the laboratory built DOPsL system used for fabrication of hydrogel fractal geometries. 3D digital models built with computer-aided design software (Autodesk® Inventor / Autodesk® AutoCAD) or a simple indexed color map relating height in .png format[51] are converted to 2D bitmap slices (MATLAB) and uploaded to the DMD chipset (1920x1080, Discover 4000 digital light processing (DLP), Texas Instruments). This bitmap information is translated to spatially tilt a pattern of micromirrors on the DMD chip. The UV light is reflected by the micromirrors and projected through the

condensation optics to a focal point within the stage area. A stage controller (Newport) is used to manage the 3-axis stage movement, while the UV source light (Omnicure S2000) was directed via a light guide toward the DMD chip at a specific angle to facilitate light reflection through the projection optics to the stage. The Omnicure halogen bulb produces a light spectrum filtered to 320nm~500nm. A Newport (model 1918) power meter was used to determine the light intensity (1.3×10^3 mW/cm^2 for polymers prepared with I2959 and I651; 6.5 mW/cm^2. Exposure times ranged from 7 to 20 seconds depending on the aperture of light. The DMD chip, the stage and the UV light source are controlled by a desktop computer. The pre-polymer is confined between a coverslip and a slide and can be transitioned through the z dimension as the pattern changes. Additionally, the structure can be removed once printed, rinsed, and printed with another layer of a different prepolymer solution.

2.3.3 Scaffold functionalization

Available carboxyl groups from the copolymerization of acrylic acid and PEGDA were utilized for amine-carboxyl mediated coupling of fibronectin to the hydrogel scaffold. A solution of 1-ethyl-3-[3-dimethylaminopropyl] carbodiimide hydrochloride (EDC) [0.15 M] (Thermofisher) and N-hydoxysuccinimide (NHS) [0.12 M] (Thermofisher) was prepared in 2-(morpholino)ethanesulfonic acid (MES) buffer at pH 5. The hydrogel scaffolds were immediately incubated in the prepared working solution for 2 hours. Samples were briefly rinsed with Dulbecco's phosphate-buffered saline

(DPBS, pH 7.4, Gibco) and then the excess solution was removed. Fibronectin at a concentration of 1mg/mL was dispensed on the sample surface and allowed to incubate for 24 hours at 4˚C protected from light. The residual fibronectin was rinsed and removed, and the samples were sterilized without solution under a UV lamp for ~30 minutes.

2.3.4 Cell culture and seeding

The human mesenchymal stem cells (hMSC's) were cultured in growth medium consisting of high glucose DMEM (Gibco), fetal bovine serum (10% v/v) (Hyclone), L-glutamine (1%) (Gibco), and penicillin / streptomycin (50 units/mL) (Gibco). Murine myoblasts C2C12 (ATCC) were cultured in growth medium consisting of high glucose DMEM (Gibco), fetal bovine serum (10% v/v) (Hyclone®), and penicillin / streptomycin (50 units/mL) (Gibco). Both cell lines were cultured at 37˚C with CO_2 (5.0%) and passaged prior to reaching confluence. Cells from passage 4-6 were seeded on the fibronectin conjugated hydrogel samples at a seeding density of ~2 x $10^4/cm^2$ and cultured for one week.

2.3.5 Bright field imaging

Primary bright field imaging was performed with a Leica DMI 6000B microscope. The images in Figure 2.5 were acquired using the tiling functionality of the Leica DMI 6000B at the 10x objective. All other bright field images were not tiled and scale bars of 100 microns are located in the lower right corner.

2.3.6 Immunofluorescent staining

After 1 week of culture, immunofluorescent staining was performed on the samples. The samples were first fixed with 4% paraformaldehyde (PFA), diluted from 16% stock PFA, with DPBS (pH 7.4) at room temperature for 10 minutes. Samples were then washed three times with room temperature DPBS (pH 7.4) for 5 minutes per wash. Fixed samples were simultaneously blocked and permeabilized with 1% BSA, 0.1% Triton-X100 mixture in DPBS (pH7.4) for 20 minutes. Each sample was incubated with 300 uL of a mixture of Fluor 488 phallodin (Invitrogen) (0.165μM) to stain actin and 6-diamidino-2-phenylindole (DAPI) (sigma-aldrich) (0.1μg/mL) to stain nuclei for 30 minutes at room temperature protected from light. A Zeiss Observer A1 fluorescence microscope was used to take fluorescent images of the samples.

2.3.7 Scanning electron microscopy (SEM)

The printed hydrogel structures underwent a gradient solvent transfer in order to reduce chance of fracture and were soaked in increasing concentrations of ethanol for 20 minutes per 10% incremental increases in concentration until ~100% was reached. Samples were removed from the 100% ethanol solution and placed in a vacuum chamber at room temperature for 24 hours. Samples were then sputter coated with iridium (Figure 2.3-carbon) and imaged via a field emission environmental microscope (FEI XL30 ESEM FEG). Images were acquired in scattering mode at 10kV.

2.4 Results and Discussion:

We used digital dynamic masks adapted from user-defined computer designed images to fabricate microscale geometries which can be extended to multiple centimeters when the pattern is tile printed (Figure 2.1A). The DOPsL method uses spatially modulated ultraviolet light to polymerize a liquid prepolymer into a solid 3D structure[35,41,46,48,52]. In essence the DMD chip is an array of reflective coated aluminum micro-mirrors, capable of creating patterns of light in fast succession, similar to displaying HD (high definition 1920 x 1080) video by controlling each micro-mirror state as being either ‘ON’ or ‘OFF’. Regions in the ‘ON’ state are photopolymerized, while in the “OFF” state, the pixel appears dark because the illuminated light is reflected away from the condensing projection lens. The micromirror pattern provides a dynamic photomask that can be modified continuously while the reservoir containing the prepolymer solution is translated through the focal plane of the projected image. The pre-polymer solidifies in a layer-by-layer fashion as per the user defined digital masks.

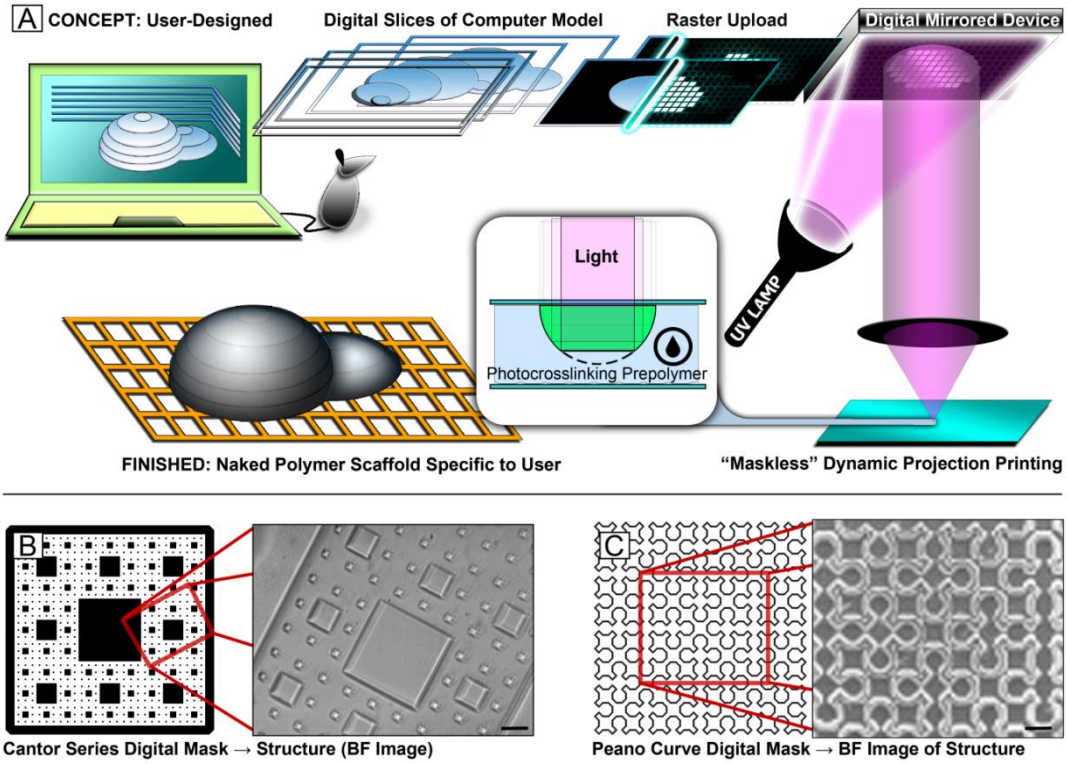

Figure 2.1: (A) Schematic of the DOPsL system: UV-light illuminates the DMD mirror array, which generates an optical pattern according to the images from the control computer. The optical pattern is projected through the optical lens and onto the photosensitive biomaterial to fabricate a 3D scaffold. Simple and complex masks can be used to fabricate fractal scaffolds in a variety of photocurable biomaterials. (B,C) Digital masks (.bmp or .png) and corresponding bright-field microscope images of the Sierpinski carpet and Peano curve fractal geometries fabricated in PEGDA biomaterial. Fabrication settings: (B) Power 1.3 W/cm^2, exposure time 12 ±2 sec. A narrowed aperture was used help taper smaller area squares to lower height. (C) P: 1.3 W/cm^2, time = 8 ± 2 sec (Scale bar = 100 μm)

Digital masks of typical non-biological vector-based, space filling fractal patterns (Serpinski carpet, Peano curve) were used to fabricate fractal scaffolds in PEGDA (Figure 2.1B&C). These patterns were chosen to examine DOPsL printing capabilities of a simple structure scaling over a large dynamic size range, and an extended single ridge fabrication without lateral stabilization from line intersection (normally found in grid designs). The Serpinski carpet pattern, a widely used Cantor series fractal abstraction in

mathematics, can be generated by dividing a large square into nine equal smaller squares, removing the central smaller square and reiterating this process a finite number of times. Despite being a purely mathematical abstraction, this structure retains self-similar objects at multiple scales. This scaling property has shown use in screening cell interactions at different scales[22,30]. This could be envisioned as an assembly of different size houses used to determine occupant preferences. The Peano curve is another variation of a space-filling curve [40] that provides increased surface area topography with contortion of a single loop or ridge (Figure 2.1C). Increased surface area has been used by other groups to facilitate better cell adhesion and faster growth[6,22,31,34].

PEGDA was used to build these non-biological patterns to provide an appropriate framework to create representative biological patterns to be extended to relevant biological applications. PEGDA is a synthetic non-degrading water containing gel (hydrogel). This material is considered to be biocompatible, easy to modify, and safe for use in humans. PEGDA can be readily conjugated with peptide adhesion motifs or coated with a physisorbed layer of fibronectin to promote cell adhesion. The mechanical properties of the polymerized PEGDA hydrogel that have been shown to influence cell proliferation and differentiation, such as stiffness and swelling, can also be tuned by the molecular weight, the concentration of the PEGDA monomer or the fabrication parameters (e.g. UV light exposure time and intensity). This

material flexibility provides a chemical means to tune biological patterns for biological use.

After demonstrating the ability to pattern more contrived mathematical patterns that explore scalable self-similarity and increased surface area through subdivision of space, we also developed several variations of the fractal tree digital masks to unify these concepts into a synthetic yet more organic or biological looking pattern. The trees (Figure 2.2) are comprised of elongated rectangles that in this case, bifurcate (divide in two) at angles deviating from the center-line of the previous iteration. These two new rectangles are reduced in dimension compared to the previous rectangle iteration by the indicated ratio. This is a simple synthetic fractal tree that encompasses a bifurcating morphology to more closely mimic the natural formation of branching biological structures. Lungs are organized based on scaling laws to maximize surface area with a volume. When we approximate this to a flattened organ we look for patterns that effectively fill space (Figure 2.4). One such ratio is the classic Fibonacci ratio “golden ratio”[19]. This ratio arises from the rate of growth found in later elements of the Fibonacci sequence (the sum of the two previous consecutive elements is equal to the value of the next element, where values are integers). This ratio is reported as, $\varphi = 1.618$ or $1 / 0.618$, which is significant as being an efficient use of building materials when trying to enclose a growing area with basic squares and claimed to be found in some biological systems. The normally associated 90˚ angle and the ratio φ have been decoupled as an example of design flexibility

to potentially isolate other aspects important to this ratio. Figure 2.2A shows the A45 R62 (angle 45 / ratio 0.62) tree template and the SEM images of fabricated branching channels featuring the fractal tree design with uniform depth (~50 µm). Fabrication of fractal structures in channels shows application in optimizing fluid flow, surface area to volume diffusion, and even pulsatile flows[19,20,22,53,54]. These patterns could also be used as molds for lab-on-chip applications[55].

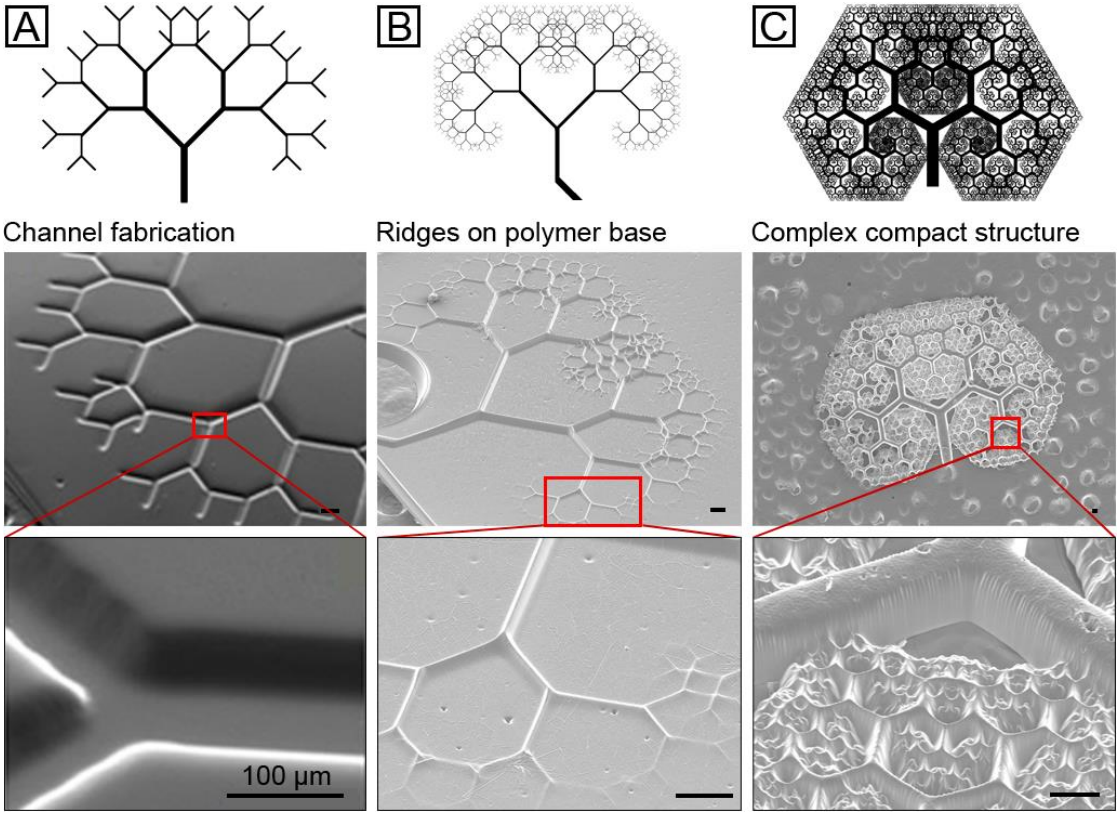

Figure 2.2: Digital masks of variations of fractal tree patterns. (A,B) SEM images of the A45 R62 tree (a basic bifurcation tree focusing on this ratio 1.618) demonstrate valleys and ridges using inverse masks. (C) SEM image of A60 R75.4 tree representing dimensions of the Pardovan sequence. Fabrication settings: (A) Power: 1.3 W/cm^2, exposure time 8 ±2 sec. (B) P = 1.3 W/cm^2, t = 15 ±2 sec. (C) P = 1.3 W/cm^2, t = 15 ±4 sec. (Scale bar = 100 µm)

Figure 2.2B demonstrates the fabrication of an A45 R62 fractal tree design with more iterations at higher resolution. Instead of channels, ridges of the fractal tree were printed to show the flexibility of the DOPsL platform. More importantly, this structure is fabricated within one exposure and features ridges stepping down at sequential iterations though narrowing the aperture. This is a unique advantage of DOPsL compared to a conventional photolithography method where it takes multiple process steps to prepare structures of variable heights.

Figure 2.2C further extends the complexity of synthetic bio-mimicking fractal tree designs and fills the empty spaces among the branches with iterating sub-trees. The Pardovan ratio (75.4) at 60˚ was selected as the scaling ratio between the consecutive iterations with a less acute spiral angle that more closely reflects hexagonal packing order of tissue within a layer (e.g. liver), and refines the amount of space-filling in the compact tissue. Variations in design can be developed by changing the degree of branching at each level, branch angle, branch width (pixel width) etc. to develop a library of fractal tree patterns to compare to other similar fractal assemblies. As such, this DOPsL platform is sufficient to create iterations across its scale regime to create hydrogel patterns mimicking many observed natural patterns.

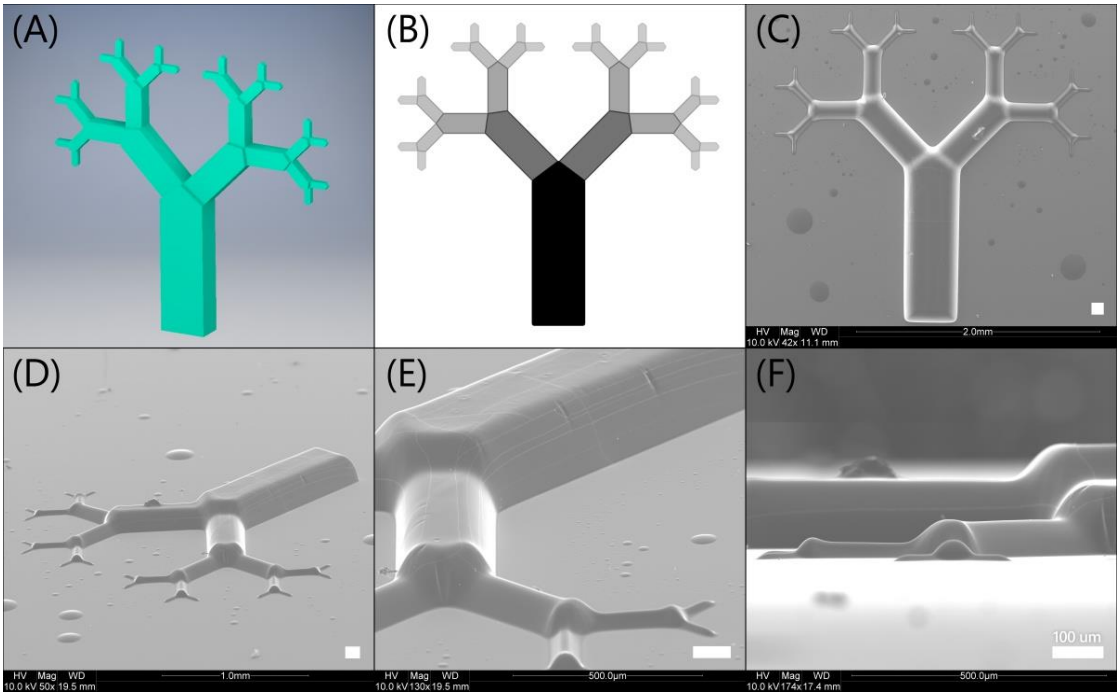

Figure 2.3: (A) 3D digital tree pattern with linear step profile, (B) corresponding stack of digital masks after applying square function correction to create linear steps (black regions represent mirrors that are "on" longest) (C – F) SEM images of fabricated 100% PEGDA hydrogel coated with carbon on methacrylated glass slide at various viewing angles and magnifications to determine printing fidelity. Fabrication settings: Power: 6.5 mW/cm2, exposure time: 10 ±1 sec. NOTE: 1.0% Irgacure 819 (photo-initiator) was intentionally chosen to achieve excessive penetration depths, in order to demonstrate z control by only generating a 250 microns structure within a 1mm prepolymer volume, despite reactivity to ambient light. (Scale bar = 100 μm)

Though spine (apex) construction was demonstrated in Figure 2.2B, linear step control in the z dimension is important in precisely controlling relative height and volume. The following linear stepped structure was printed to better illustrate the DOPsL's printing fidelity which may be determined when comparing the 3D model in Figure 2.3A to the SEM images in Figure 2.3C-F. This following structure was created in a 1 mm tall volume of solution despite only being 250 microns in height to demonstrate height control without exterior confinement. The 3D structure slices which make up the digital masks had a function algorithm applied to adjust for light intensity changes over distance in

order to create relatively linear step intervals. Figure 2.3B represents a z-stacked summation of these planar slice masks after applying the algorithm exposure shift. Figures 2.3C-F show the carbon coated fractal structure on glass at different angles. The SEM drying process causes some contraction more noticeable at the top of structure, and is evident in corner rounding. Although gradient slopes present little difficultly as seen in our laboratory's previous work[51], truly vertical sidewalls are difficult to achieve when using soft polymer compositions of HMBS without increasing TEMPO. Vertical sidewalls under high concentrations of TEMPO are presented in supporting information. This structure in Figure 2.3 presents a scaling fractal tree at user controlled heights decoupled from the length/width ratio to emphasis parametric tunability and printing fidelity of this synthetic branch pattern.

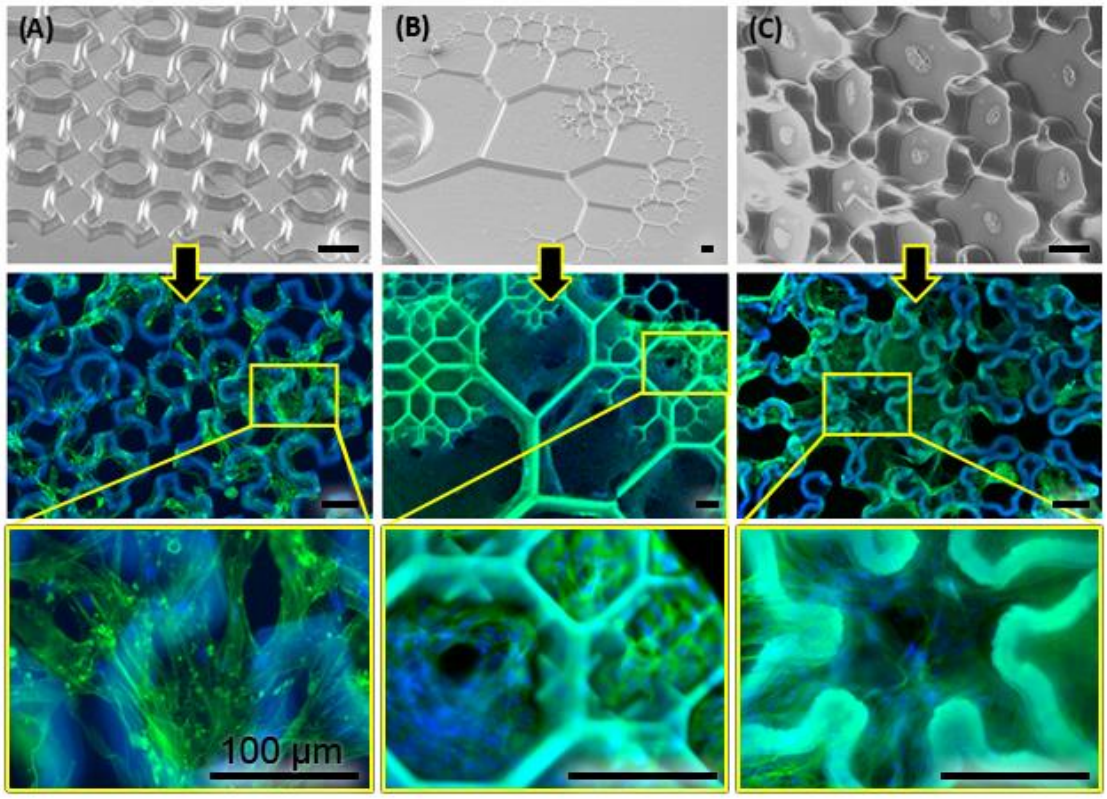

Figure 2.4: Cell interactions with fractal topographies. (Top row) SEM images of the corresponding hydrogel structures conjugated with fibronectin. (Middle row) fluorescent microscope images taken with 10x:5x:10x (A:B:C) objective DAPI/actin stain. (Bottom row) fluorescent microscope images taken with 40x objective DAPI/actin stain. (A) murine myoblasts (B,C) human mesenchymal stem cells. Fabrication settings: (A) –see Figure 2.1C; (B) – see Figure 2.2B; (C) P: 1.3 W/cm^2, exposure time: 9 ±2 sec on glass (Scale bar = 100 µm)

The scaffolds from the previous sections of mathematically abstract patterns (Figure 2.1C), to synthetic branching patterns (Figure 2.2B), and more organic hexagonal packing patterns were printed with a biocompatible polymer (PEGDA) and coated with the cell adhesive protein (fibronectin) to demonstrate the potential of 3D-printed scaffolds towards use in bioengineering. Figure 2.4 shows images of human mesenchymal stem cells (hMSCs) and murine myoblasts seeded on fractal structures made of PEDGA. In this case the PEDGA scaffolds from Figure 2.1C and Figure 2.2B were

coated with fibronectin, and cells were seeded (passage 4) and stained for actin fibers (phallodin 488 / green) and nucleus (DAPI / blue). Figure 2.4A shows the seeding of murine myoblasts on the Peano curve to effectively increase surface area and shows a cluster of murine myoblasts interacting with the printed curve structures. Figure 2.4B shows the seeding of hMSCs on the fractal tree design. The cells appear to show some direction bias related to the largest ridge topography, which is inconsistent across varying ridge heights. The magnified region of interest of Figure 2.4B shows a region of intersecting pattern overlap at the exterior edge. This region contains an area of moderate aspect ridges in close proximity to the single pixel topographies. The cells appear localized near the higher aspect ridges and filling these high sided wells or gaps while the cells appear to have grown over many of the smaller features which may provide increased surfaces for binding. Figure 2.4C shows the seeding of hMSCs on a hexagonal packing structure designed to reflect motifs of compacted cell clusters. More cells were observed spanning across the larger gaps, however this structure is on a glass substrate which may be influencing this cell behavior. The hydrogel structure was shown as sufficiently biocompatible to murine fibroblast 10T1/2's (supporting information). Both cell types were found to adhere and grow on the fractal geometry scaffolds. These results establish the feasibility of using fractal design for addressing biological questions[55,56].

Moving beyond simple geometries, several compact ordering models can be used as demonstrated in Figure 2.5. These ratios for compact

organization start with classic regular polygon growth systems in the form of Fibonacci and Pardov spirals. Starting from the center and moving to the periphery, these sequences produce enclosed areas at each iteration, and generate new area extension with lower resource cost by utilizing the neighboring “wall” of preexisting structures as seen in all compact spirals. This means that the entire structure as a whole can extend and grow, while the existing structure remains completely intact and functional (less vulnerable) during this period. Additionally the system is compartmentalized which improves robustness. These are two trends that are advantages to many systems including biological organisms. These basic structures can be inscribed with fractal patterns to improve surface area as shown in Figure 2.5A, and carried onto increasingly complex generations via computer, and then printed as shown in the bright field image (Figure 2.5A). This is an exercise demonstrating user-controlled complexities meshed with known optimizations of a packing order.

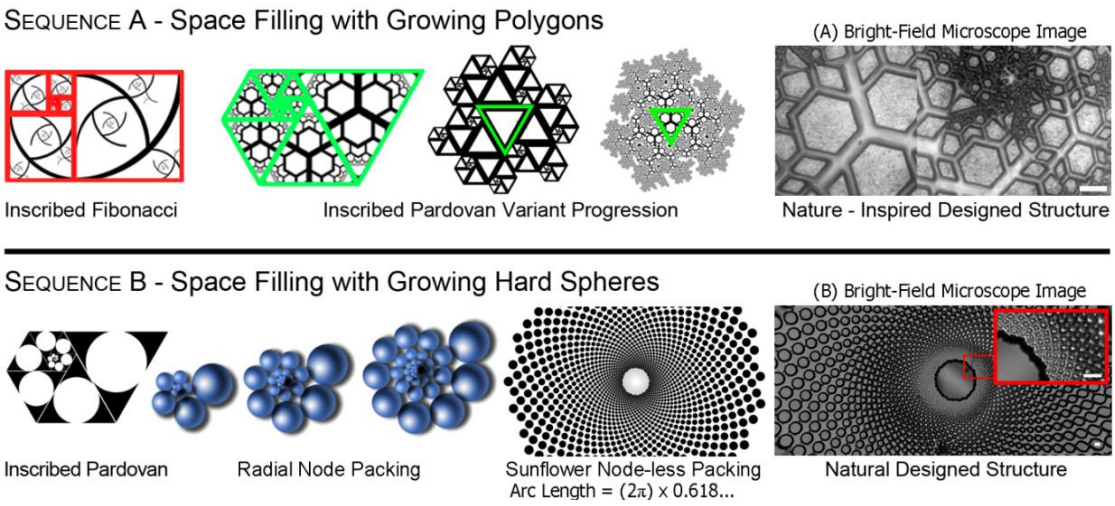

Figure 2.5: Several compaction models are developed to fill the space optimally. Sequence A: Evolution of simple synthetic fractal design. Fractal patterned tiles substituted or inscribed within solid tiles for generation of more complex structures. The original pattern is translocated, scaled, and repeated to generate organic structures that resemble broccoli heads or pine cones. Image A: The bright-field microscopy image of a printed hydrogel structure from the designed synthetic template. Sequence B: Packing models inscribing growing circles into Pardov's ratio not filling space. A simple hard sphere model showing radial alignment of spheres, also showing gaps in packing structure. Natural "sunflower" design to show more ideal node-less packing of a growing spiral system. The printed "sunflower" design in 100% PEGDA (INSET: detail is maintained close to center) Fabrication Settings: (A) Power: 1.3 W/cm^2, exposure time: 18 ±2 sec.; (B) P = 1.3 W/cm^2, t = 16 ±2 sec.; sidewall ratio is 6.5 to 1 (Scale bar = 100 μm)

This application is more clearly relevant, if we assume our structures of interest are spheres, or have circular footprints which find a packing shape as columnar structures. These columnar growth units become irregular polygonal prisms or hexagonal prism structures[27] when regularly packed as seen with bee honeycombs and liver tissue. However when we imbue Fibonacci sequence or a Padovan sequence ratio space filling models with inscribed circles we have some gaps as in Figure 2.4B. A simple model can be used to generate a radial aligned hard sphere packing approximation that can be applied to irregular polygons. This works for some shell structures, however tends to extend these structures farther into the z with volume. We can extend

the Fibonacci A+B = A' Boolean to wrap structures around a circle to achieve the patterns associated with sunflower seeds and pineapples[28]. This classic pattern of seed packing has been well studied and is noted for having an emanating growth center. Implementing such biomimicry, we can borrow this pattern from nature to create our own hydrogel pattern for "sunflower" node-less packing. This sunflower pattern was fabricated with PEGDA on a slab (Figure 2.5B). Many natural observed growth patterns deviate from the purely mathematical abstractions and DOPsL platform can accommodate building such structures.

However due to the minimal cross-sectional area from the design complexity, and lacking structural support due to the soft hydrogel material used, this approach is typically more applicable for complex flatter structures with height and depth but without overhanging ledges. From a manufacturing point-of-view, the advantage of manipulating the fractal dimension through control of surface fractality is very appealing when available during the onset of a design. This control is the primary driving force behind developing algorithm based topographies. Using this algorithm approach, self-similar fractal topographies such as vascular trees based on Lindenmayer models (Pardovan series) or based on Murray's bifurcation laws, can be obtained. Computer implementation to design such patterns also allows parametric design, and a multitude of variations in a design that can be carried out by changing the value of one parameter (for example, the angle, ratio, number of bifurcations, or a fluidic port addition, refer to Figure 2.5)[57],[58]. Incorporation of

tunable fractality at a design-stage using 3D printing approaches to print structure and localize cells will improve the capabilities of current tissue engineering strategies[59].

2.5 CONCLUSION

We have demonstrated the capabilities of the DOPsL platform as a flexible method to create various fractal forms in a medium conducive to cell growth. Fractal patterns that are purely mathematical, biologically inspired, and directly mimicking observed biological organization have been translated to biocompatible hydrogel photopolymer scaffolds. These moderately complex topographic patterns were implemented as channels or ridges of varying width and height and affect cell alignment as compared to a 2D slab. These results show the topographic possibilities of engineered surface structures to increase surface area, subdivide space in self-similar organization, and produce scaling structures reflecting compact growth. These topographies may have more immediate use in screening “scale” dependent characteristics of cells, however the goal of imposing optimized biological growth topographies in order to effectively organize cells is still desired. There are many natural systems, and thus many optimized structures to be created. With increasingly accurate computer models of forces, viscosity, diffusion, and aggregation, generating relevant scaffolds for each system is likely possible with the DOPsL platform.

2.6 ACKNOWLEDGEMENTS

The project described was supported in part by the Department of Defense (W81XWH-14-1-0522), California Institute for Regenerative Medicine (RT3-07899) and National Science Foundation (CMMI-1332681 and CMMI-1547005). We thank Dr. Shyni Varghese for kindly providing the MSC's and murine myoblasts and some microscope use for this work. We thank the UCSD Nanoengineering Materials Research Center for SEM imaging. We also thank Peter Chung, Adam H. Aitkenhead, Justin Liu, Xuanyi Ma and Dr. Donald Sirbuly for their assistance.

2.7 SUPPORTING INFORMATION:

-(SI 2.6) SEM of high aspect ratio PEGDA hydrogel with TEMPO [0.1%]

-(SI 2.7) Composite fluorescent microscope image of live/dead stain C2C12's on hydrogel

2.7.1 Manuscript statement (SI 2.6):

"Although gradient slopes present little difficultly as seen in our laboratory's previous work, truly vertical sidewalls are difficult to achieve when using soft polymer compositions of HMBS without increasing TEMPO."

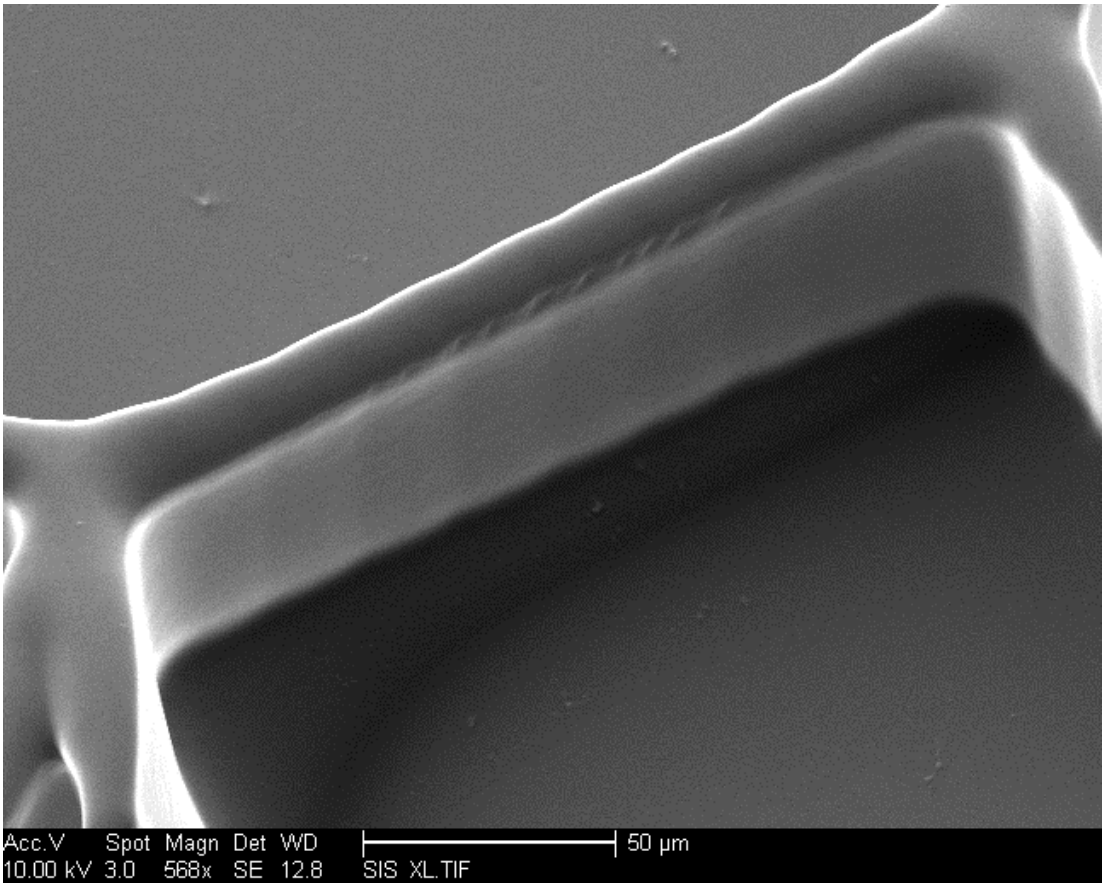

Figure 2.6: High aspect ratio hydrogel sidewall structure: Hydrogel structure fabricated at high TEMPO concentration without HMBS to demonstrate nearly vertical sidewalls. SEM image of a 20 x 50 micron extension of a branched single height fractal layer. Composition: PEGDA [~100%], Irgacure 2959 [1.0%], TEMPO [0.1%]. Fabrication: P = 1.3 W/cm^2 ; t = 8 ± 4 sec.

Since TEMPO has been shown to be cytotoxic in moderate doses, we intentionally have not used images of hydrogel structures containing higher concentrations of this particular free radical terminator to prevent potential confusion and misrepresentation of our data. This high TEMPO composition conflicts with our intent to use these structures in future work towards differentiating MSC's.

2.7.2 Manuscript statement (SI 2.7):

"The printed hydrogel structure was shown as sufficiently biocompatible to murine fibroblast 10T1/2's."

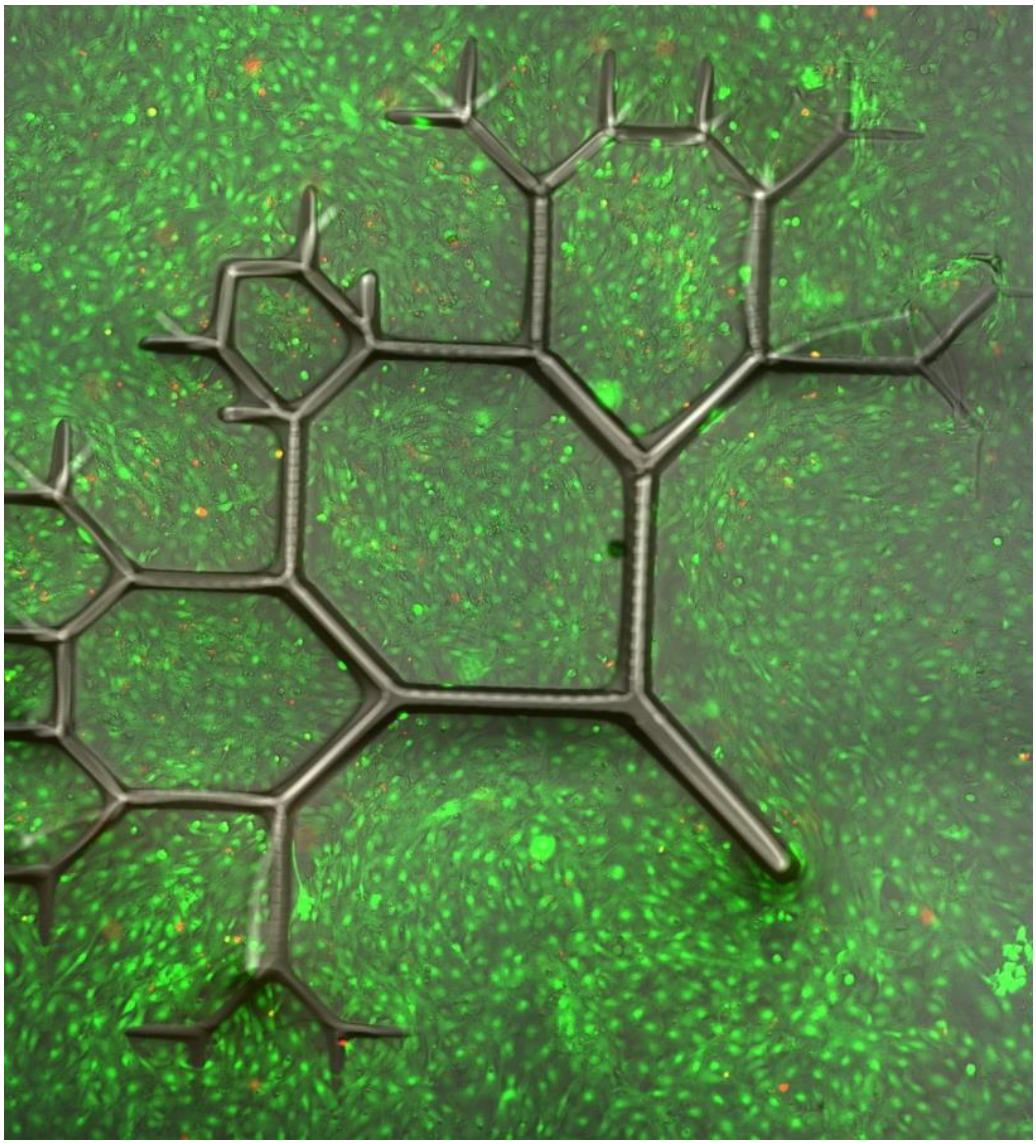

Figure 2.7: Printed hydrogel cell viability: Fluorescent microscope image of LIVE/DEAD (ThermoFisher) stain of murine fibroblasts 10T1/2 (ATCC) seeded on a fibronectin-conjugated photopolymerized PEGDA hydrogel. Day 5 of incubation on scaffolds. Channels: (Green = Live - Calcein AM), (Red = Dead-ethidium homodimer-1), and (Gray = bright field). Image assembled in Image J. Substrate Composition: 50% Poly (ethylene glycol) diacrylate PEGDA (Mn = 575), in water solution, 2,2,6,6-tetramethylpiperdine 1-oxyl TEMPO [0.01% w/v], 5-Benzoyl-4-hydroxy-2-methoxybenzenesulfonic acid **[**HMBS] [0.1% w/v], acrylic acid [1.0% v/v] and Irgacure 2959 [1.0% w/v]**.**

Chapter 2, in full, is a reprint of the material as it appears in Warner, John; Soman, Pranav: Zhu, Wei; Tom, Matthew; Chen, Shaochen, “Design and 3D Printing of Hydrogel Scaffolds with Fractal Geometries”, ACS Biomaterials Science & Engineering, vol. 8, 2015. The dissertation author was the primary investigator and author of this paper.

Chapter 3: Printed Biomaterials with Regional Auxetic Properties

3.1 Abstract

We use dynamic optical projection stereolithography (DOPsL) to build multilayered non-positive Poison's ratio cell scaffolds. With material-specific designs capable of tuning force-displacement curves of localized regions within a single cytocompatible structure at architecture scales consistent with tissue interaction, this construction technique may prove useful in stretch-mediated cell-differentiation, which is important to muscle and tendon regrowth or replacement. These 3D printed structures were embedded in an alginate-acrylate hydrogel to demonstrate partially coupled dynamic motion of the auxetic skeleton structure to a normally non-auxetic material. Though the coupled auxetic behavior was reduced compared to the multilayer auxetic skeleton, the skeleton encased structure demonstrated a means to locally tune the axial-transverse ratio of the structure within the full range of motion. This ability would be unique, providing better stretch-mediated criteria for various cell-types within the tendon-to-muscle tissue transition.

3.2 Introduction

Dynamic optical projection stereolithography (DOPsL) 3D printing of soft materials affords reiterative design improvement of the unit-cell structures to accommodate scale, force, dynamic range and material type optimization appropriate for muscle-tendon tissues [cite-Allison]. Utilizing various unit-cell structures, a single scaffold can be imbued with different "stretch" properties

which have been implicated in altering stem cell differentiation[1–3,15]. Though conventional positive Poisson's ratio stretching materials have been normally used, with the additive manufacturing process of DOPsL, both positive and negative Poisson's ratio materials can be created in the same structure permitting a means of creating supported tissue with multiple, physical, cell-differentiating cues. Additionally, during miniaturization of 3D printed dynamic unit-cell structures, material and design limitations were observed that exceed the conventional challenges of micron resolution static structures associated with bioengineering. These obstacles were overcome using Finite Element Analysis (FEA) of the dynamic regions to improve printed unit-cell performance according to material flexibility and limitations.

Auxetic structures are counter-intuitive in that axial elongation causes transverse expansion rather than contraction[60,61]. The degree of "auxetic-ness" is conveyed as a negative Poisson's Ratio (PR), which is expressed as the axial elongation over the transverse contraction or the axial contraction over the transverse elongation. Additionally, the PR is not necessarily a constant value and such deviation can be more apparent with unit-cell imbued structures. PR not only can vary with the amount of displacement, but also with the portion of the range of motion utilized by that displacement. These factors are determined by the unit-cell structure and the material. The increase in length and width translate to an increase in effective area when applying axial tension, while axial contraction causes the corollary effect with potential

to increase pressure. This behavior is critical in manipulating forces and physical cues responsible for cell differentiation.

Current industrial applications distributing force include impact-resistant vests, supportive clothing, and packing materials[60,62,63]. Interestingly, tendons also possess auxetic and tolerate large forces. Researchers have attributed the auxetic behavior of tendons to their polymeric helical sub-structure[64,65]. The helical structure functions as a coiled spring with the means to mechanically store energy. Translated to 2D, this helical spring appears as a continuous zigzag structure (z-line) from the side view. The z-line is not auxetic itself and requires coupling elements (CE) to sum (negative PR) or negate (zero PR) this lateral mechanical movement. Most bulk materials possess a positive PR, yet auxetic unit-cell patterning utilizes designed vacant space to accommodate mechanical translation of these internal elements to permit a macro negative PR characteristic. Even molecular NPR foams require space for conformational changes[62]. By imbuing a flexible unit-cell structure, the resulting “mesh” structure as a whole is more compliant overall than an equivalent slab related to reduction of cross-sectional area, programming auxetic movement at the cost of overall tensile strength. As such, unit-cell structure “meshes” necessitate using terms like “effective area” when describing macromolecular auxetics. Though designed 2D auxetic structures are predominant, 3D auxetic structures exist down to the molecular level as foams. Additionally, different auxetic unit-cell structures exist; applying z-line

structures as CE's on different axes can create rotational auxetics as opposed to re-entrant designs.

While other groups have found auxetic properties in tissue engineering for tendons and vasculature[54], our group had previously created auxetic hydrogel structures to examine effects on individual cells[66]. However these scaffolds were too small for tissue replacement and the NPR and ZPR ranges were limited by fragile material properties due to miniaturization. Synthetic and hybrid hydrogels are often used in biomaterial photo-printing in efforts to mimic the native mostly hydrogel extracellular matrix (ECM) of mammalian cells. This logical trend of cell environment recapitulation usually involves softer pre-differentiated materials in the form of slabs matching configurations found in vitro. As being notoriously soft materials, the usually fragile hydrogels are best for bulk slabs, static structures, and even larger unit-cell structures. However, when improving resolution, "tougher" materials are necessary to offset the reduced cross-sectional area of unit-cell structures. Using a more robust material for the mesh prevents structure collapse and enables translation of unit-cell forces over larger areas while maintaining similar overall stiffness of a native hydrogel. Despite unit-cell collapse and limited force translation using hydrogels, some bizarre observations were obtained from cells grown on "reentrant" auxetic structures with two-photon polymerization that appeared unable to complete the final phase of mitotic separation[66]. The impressive ~16 μm resolution of the unit-cell was matched to the biological cell size ~45 μm, and despite displacements that were not entirely translated to

adjacent structural unit-cells, the cell experienced a localized single unit-cell auxetic effect. The scaffold was too fragile to support its own weight in air, but provides the most intriguing observation of cell behavior on synthetic auxetics seen to date. The Lewis group transitioned these material, scalability, and range concepts in their own way with a more robust PDMS material applied at macroscale ~4 x 10^3 μm unit cells[67].

The previous work shows progressive improvement with some unexpected observations through reiterations of design and materials. The goal of this work is to create synthetic auxetic scaffolds for actuation and mechanical energy storage to mimic aspects of tendon behavior. This directs the scaling of unit-cell miniaturization to be compatible with cell aggregation to encourage some tissue formation. Additionally, the unit-cell mesh needs to incorporate a greater tunable dynamic auxetic range to be capable to match prospective tissue requirements while still being functional in larger area mesh structures to meet replacement tissue sizes. These objectives require material strength, high resolution, design flexibility and high scalability that were achieved using a photopolymerizable polyurethane material mixture with a projection stereo-lithography printing technology.

In our efforts to build on other groups' successes, we chose a more robust elastomeric material like PDMS to be printed with dynamic optical projection stereo-lithography (DOPsL). This system has previously been shown to print hydrogel structures in complex patterns, at high resolution, and in a readily scalable format[68].

The BR-7432IG30 material used from Biomar® was a consistent and easy to obtain off-the-shelf (OTS) polyurethane capable of photopolymerization with existing characteristics suitable for computer simulation[69]. This polymerized poly-aliphatic urethane-acrylate blend with isobornyl acrylate as the incorporated plasticizer (PAUA/IBOA) was more cytocompatible than originally anticipated and was sufficient for our demonstration purposes and testing. The more robust polymerized OTS PAUA/IBOA material was easier to handle and tolerated increased strain per cross-sectional area than conventionally printed hydrogels. These factors permitted more functional smaller unit-cell structures to be created within even larger meshes.

The DOPsL platform was chosen for parallel projection polymerization, which is capable of fast tile printing of the larger structures anticipated for tendons. The mask-less digital design provides nearly infinite tunability in unit-cell shape to effect stiffness and range of motion. The digital-masks can be altered at pixel resolutions that correspond to ~ 3 μm increments given the setup used. This digital flexibility translates to fabrication tunability that allows mesh stiffness alteration via strut thickness and design changes. The 25 μm strut resolutions provide a scale consistent for interaction with aggregate cells in a tissue, however are unlikely to auxeticly influence individual cells.

In comparison with two-photon lithography[13,35,41,66], DOPsL reflects the classic trade-off between faster times to create application relevant and robust

mesh sizes with sufficient resolution, versus smaller unit-cell auxetic structures generated with slower serial fabrication.

3.3 Materials and Methods

3.3.1 Photopolymer mixtures

BR-7432IG30 polyaliphatic urethane acrylate blend (30%/70%) with isobornyl acrylate (PAUA-IBOA) was donated by Biomar® as an off-the-shelf photopolymerizable polyurethane. 2,2,6,6-tetramethylpiperidine 1-oxyl (TEMPO) acquired from Sigma-Aldrich was added to PAUA-IBOA [0.1% w/w]. Irgacure 819 acquired from Chiba was added to PAUA-IBOA/TEMPO mixture [2.0% w/w]. UV absorber was eliminated to maintain a better aspect ratio in order to improve in-plane hinge bending and reduce cell toxicity. The concentration of free-radical terminator (TEMPO) was increased to reduce the mean free path of free-radical chain propagation ultimately reducing print "bleed". Photocurable PAUA/IBOA prepolymer is moderately viscous and was weighed in a tarred glass scintillation vial. Pre-weighed TEMPO was added, mixed slowly with a magnetic stir bar for 1 hour while loosely capped, protected from light, fixed in place, and partially submerged in a 50˚C water bath. Irgacure 819 was added afterward and allowed to mix for another 6-12 hours at room temperature. NOTE: This material also binds strongly to glass even without coating (methacrylation).

3.3.2 DOPsL (Dynamic Optical Projection Stereolithography) setup

Figure 3.1 shows our in-house Dynamic Optical Projection Stereolithography (DOPsL) printer, which features a digital micromirror device (DMD), an ultraviolet light source (Omnicure S2000), and a computer-controlled stage (Newport). The DLP 4000 UV coated (digital light projection) chip from Texas Instruments reflects the UV light in a pattern of our design through the condensation lens to be focused and miniaturized onto the fabrication stage. The pattern is any HD (1920 x 1080) pixel image. The flexible nature of the platform permits rapid prototyping of dynamic mechanical structures via changing strut thickness or hinge design with pixel by pixel control. This platform also enables construction of larger structures through printing a preloaded cache of different images into a larger unified tiled array while maintaining ~4 micron resolution. This expanded construction mode is only limited by stage movement and the material holder. The mesh constructs referred to in this paper are not larger than 2 cm, yet retain structural components that are 25 μm and tolerate tissue associated load. The UV light source for this experiment used an Omincure S2000 halogen bulb with a 320 nm filter before the light guide, but outside of the normal housing.

The photocurable prepolymer solution is sandwiched between a glass slide and a coverslip with spacers to confine the z-height of the solution consistent with the layer. In doing so, the system can be fed new prepolymer layers quickly. Normal operation can produce a PAUA/ IBOA multilayer mesh samples in ~3 minutes. NOTE: PAUA requires a thin oil coat (Krytox) or PDMS thin slab. The photocurable resins are polymerized via spatial and

temporal light patterning on a glass slide. The PAUA/IBOA is carefully removed with tweezers and soaked in chloroform for 5 – 10 minutes. The material will then swell. This process removes the excess viscous prepolymer and decreases the possibility of trapped viable bacteria causing contamination. The material is immediately transferred to ~100% ethanol to slow and stabilize the material shrinking from chloroform evaporation to reduce potential for scaffold fracture, until returning to expected size and then rinsed with millQ and placed in a sterile container.

3.3.3 Cell culture and fluorescent staining

C3H/10T1/2 clone 8, Mus Musculus fibroblast line was thawed from cryopreservation and used at passage 18. C3H/C2C12 Mus Musculus myoblast line was thawed from cryopreservation and used at passage 3 when observed as healthy. Both cell lines were acquired from ATCC and cultured in growth medium (Gibco) Dulbecco's Modified Eagle's Medium (DMEM) and supplemented with 10% fetal bovine serum (Gibco). Cells were passaged upon reaching 80-90% confluence: rinsed with 10 mL of sPBS buffer (Gibco), using 1 mL of Trypsin-EDTA [0.25%] and incubated at 37˚C for 5-10 min with 1/10 media resuspension. 1 mL of resuspension was used in passaging (1 to 4-6 split). Resuspensions were centrifuged at 100 x g for 2 minutes, supernatant removed and resuspended in cell media to 1 x 10^3 cells/µL prior to scaffold seeding. Cell seeded scaffolds were rinse with 3 mL of PBS for 1 minute 3 times prior to staining. Live-Dead staining was performed with

LIVE/DEAD® Viability Kit L3224 (Life Technologies) using calcein AM and ethidium homodimer per insert instructions. 10T1/2 samples were fixed after staining. Cell scaffolds were fixed at timepoints [day 22] with 4% paraformaldehyde in PBS for 20 minutes and permeabilized in 3% BSA, 0.1% Triton-X in PBS. All C2C12 samples were stained and imaged immediately without fixing. Cells were stained with Hoechst 33342 (Life Technologies) / Rhodamine phallodin (Biotium) per package instructions.

3.3.4 Scaffold preparation:

During initial studies to determine the extent of fibroblast (C3H/10T1/2) cell adhesion to the uncoated PAUA/IBOA polymer and in order to gauge unpolymerized PAUA or IBOA cell toxicity, it was observed that non-chloroform soaked PAUA/IBOA treated with 2% penicillin and streptomycin for 24 hrs, and then left in media with 1% penicillin and streptomycin appeared to have bacterial growth between the culture plate and polymerized material while controls came up negative. This test was inconclusive because PAUA/IBOA has difficulty passing through a 0.22 um filter, however the cells exposed to unpolymerized PAUA/IBOA and non-chloroform treated PAUA/IBOA both appeared to bacterially contaminated and appeared to slow cell growth.

It is our practice that PAUA/IBOA scaffolds must at sometime be soaked in chloroform per the above procedure. PAUA/IBOA was then transferred to a sterile biological safety cabinet (BSC) where 30 µL of

fibronectin (2μg/mL) was added to the scaffold surface and placed in at vacuum for 30 minutes at room temperature and then treated on the other side (if a vacuum chamber is not available this process takes 2 days at 4C). The material was then stored at room temperature for 30 minutes in sterile PBS with 2% penicillin and streptomycin followed by 24 hours at 4C. Prior to seeding the antibiotic decontamination solution (PBS with 2% P/S) was removed.

Cells were seeded directly atop the scaffold at ~2 x 10^4 in a 20 μL volume of cell media (per ATCC) and allowed to sit on the scaffold for 30 minutes at 37˚C at 5% CO2. After the allotted time warmed culture media (cell media with 1% penicillin and streptomycin) was carefully flooded around the scaffold. The scaffold was gently depressed if floating. The samples were cultured in 12 and 24 well plates, and were gently transferred to new plates when the cell growth on the bottom of the well approached confluence (~3-4 days). 10T1/2 lines were terminated after 12 days after confirming PAUA/IBOA + fibronectin scaffolds could facilitate cell adhesion, cell survival, and cell gap spanning potential. C2C12 were run for 26 days. All cells died as a result of biofouled media after a faulty electrical stimulus connection to the platinum leads.

3.3.5 Scanning electron microscopy

10 KV was used for scattering mode images and 20-30 KV was used for backscattered images via a field emission environmental microscope (FEI

XL30 ESEM FEG). PAUA/IBOA is not a hydrogel and does not require ethanol-dehydration prior to exposure to ultra high vacuum. SEM images of hydrogels often shrink from the state in which they are used possibility changing observed aspect ratio, whereas PAUA/IBOA does not appear to have this issue. As such the information from SEM provides a more relevant approximation of the environment that the cells interact with. Though the PAUA/IBOA experience mild charging, no sputter coat was required for scattered or backscattered images. UHV for 24hr was still used as a precaution for degassing of residual organics to prolong filament use.

3.4 Results and Discussion

Figure 3.1A provides a simple representation of the dynamic optical projection stereolithography (DOPsL) system used for these experiments. Spatial patterns of UV light are miniaturized and projected onto the prepolymer, where photon-initiated free-radicals propagate a chemical polymerization reaction to solidify said pattern into a structure. The pattern is determined by a computer controlled dynamic digital mirror array capable of rapid full “screen” changes (24 fps) depending digital image input for each area or “tile” printed. In this tiling manner, this specific DOPsL system provides scalability (3 x 5 cm) with high resolution (3.8 μm/px) in minimal time (seconds for print-move) without the conventional constraints of a static mould or quartz light-mask.

Figure 3.1BC shows a PAUA/IBOA 3-tile conventionally designed re-entrant auxetic structure in the maximum tolerated compressed (B) and stretched (C) states. This structure is being actuated along the vertical z-lines while the horizontal coupling elements (CEs) displace the structure transversely and increase the “effective area” of the unit cells. The accordion-like z-line (green), stores energy like a spring, which stretches and compresses axially. The associated non-axial displacement is coupled to neighboring z-line with CE’s (purple) to exert force laterally. Based on the hinge design and material properties, this structure is surprisingly at its range limits. Despite the appearance of sufficient space to enable further movement of the unit-cell structure shown in Figure 3.1B and Figure 3.1C, the structure buckles or fractures when further compressed or stretched, which demonstrates potential for functional improvement. Additionally, less compressible materials tend to make the design limitations more noticeable as the scale is reduced. In this particular case the range of motion is limited to axial change of 17.5% with a transverse change of 21.1%. The structures coupling elements are effectively large at 2.2 mm.

At this same approximate scale Figure 3.1D shows a thin-walled 2 cm square-grid with sub-millimeter architecture printed without removing the prepolymer. After an ethanol rinse to remove prepolymer material followed by the addition of water, Figure 3.1E shows the resulting transition into a classic counter-rotational auxetic used by Clausen. In this case the z-lines and coupling elements are the same and show how some systems achieve an

auxetic state without an imbued synthetic design. This suggests that auxetics might be more integral as a physical state of a unit-cell structure mechanical energy storage. The physical contraction induced by the solvent change again demonstrates that auxetic structures can be a formed in association with natural means of mechanical energy storage. The cohesive tension of water is a potential justification for the 14.5% contraction of the grid into the simple naturally arranged auxetic.

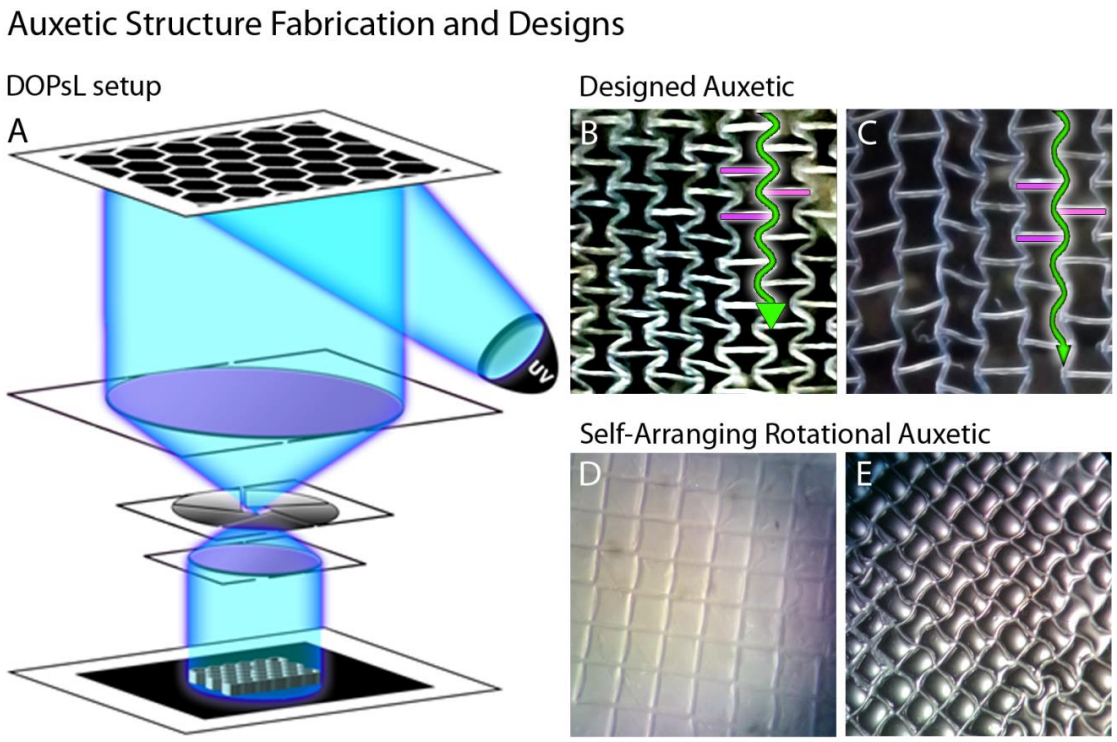

Figure 3.1: Auxetic structure fabrication and designs. Introduction to auxetic structures: (A) Method to photo-polymerize unit-cell mesh macrostructures with a Digital Micromirror Device reflective array, projected ultraviolet light and condensation lenses. (B) Printed “reentrant” auxetic or negative Poisson’s ratio design at large resolution imaged at compression before buckling. (C) Same structure imaged at full extension before shear. Both cases appear to have extra unit cell space, yet fail. (Green = z-line, purple = coupling elements at 2.2 mm). (D) Printed grid with 2 mm struts imaged in prepolymer. (E) Structure in image (D) washed with alcohol and filled with water show contraction and natural formation of a rotational auxetic. Structure composition PAUA/IBOA.

A problem with the existing auxetic structure in Figure 3.1B is limitation in movement range. Despite using a stronger yet less compressible material than a hydrogel, functionality is limited at this scale in addition to the robustness of the unit-cell. However, Figure 3.1E shows structure distortion around the periphery that in not translated through the rest of the structure. As expected, auxetic structures are more effective at mechanical energy storage when not showing regional collapse, such that struts are able to effectively exert lateral force on adjacent z-lines. The region on interest that is functional lies between being too rigid Figure 3.1B and too flexible in Figure 3.1E.

With miniaturization, often solid, non-monocoque structural elements such as struts and hinge regions intuitively become more flexible and fragile. This common phenomenon is more pronounced in structures composed of hydrogels, which are already notoriously soft. Additionally with miniaturization, instrument “noise” begins to compete with intended “signal” and artifact structure bleed becomes more challenging.

When moving to a stronger material with less compressibility, we observe buckling followed by fracture of the unit-cell with compression where noticeable structure bleed is present such as Figure 3.2A and 2E. Failure tends to occur at internal angles of ~30 degrees of this structure. Finite element analysis (FEA) using material properties of PAUA/IBOA confirm observations of fracture at the strut just before the hinge joint. Figure 3.2B and Figure 3.2F show rounded hinges that permit better mobility of the unit-cell during compression and axial elongation thus increasing the overall unit-cell

ranges. However, when reduced ¼ in scale (Figure 3.2C), the hinges pivot at many angles other than those normal to the plane, causing struts to rotate out-of-plane and become “wobbly” and unstable. This out-of-plane flexion was stabilized by laterally increasing the cross-sectional area of regions bracketing the intended hinge area, thus stiffening regions neighboring intended in-plane flexion. This reconfiguration was achieved in Figure 3.2D while staying within material tolerances and localizing flex to the hinges instead of the struts as modeled in Figure 3.2G.

Finite element analysis (FEA) was used to corroborate our observations. Figure 3.2E shows localized strain to the struts. Despite this type of strain being less debilitating for structures of softer materials, excessive compression or extension still yields failure in the strut. When using stronger materials to achieve finer resolution structures, this “acute-angle” design limits the unit-cell range, not by internal collision, but by restriction from structure strain. This force was sufficient to cause out-of-plane compressive buckling and also out-of-plane tensile deflection, both eventually resulting in mechanical failure. Miniaturization of the “acute-angle” unit-cell structure flexed struts instead of the anticipated hinge regions due to fabrication bleed absent from earlier FEA models. Figure 3.2F demonstrated that distributing the flexion force along too much of the bending region enables a wobbly hinge, which allowed out-of-plane movement and a predictably very soft mesh. The stabilized hinge localizes the flexure to a narrower region creating a more ideal “point” hinge that does not exceed the material properties (Figure 3.2G)

while incorporating design consideration for material bleed characteristics at this scale. Using this information we can tune meshes of smaller features to perform more towards what is expected. The hinge design doesn't make the structure stronger, it actually focuses stress into a smaller area requiring stronger materials, in order to maintain or improve the range of motion of the unit-cell mesh as we scale down the unit size to a more "cell interactive level." Additionally, the use of hydrogels created sloppiness in the design and accommodated a larger range of motion with strut compressibility. Simple ACUTE designs show strut flexion. ROUNDED hinge designs show too much distribution of force and too many flexion angles that are less normal to XY plane. STABILIZED ROUNDED is more optimized for material at this scale. As expected, summation of hinge designs affect unit-cell, and influence overall mesh softness and stretchability for added tunability in differentiating stem cells.

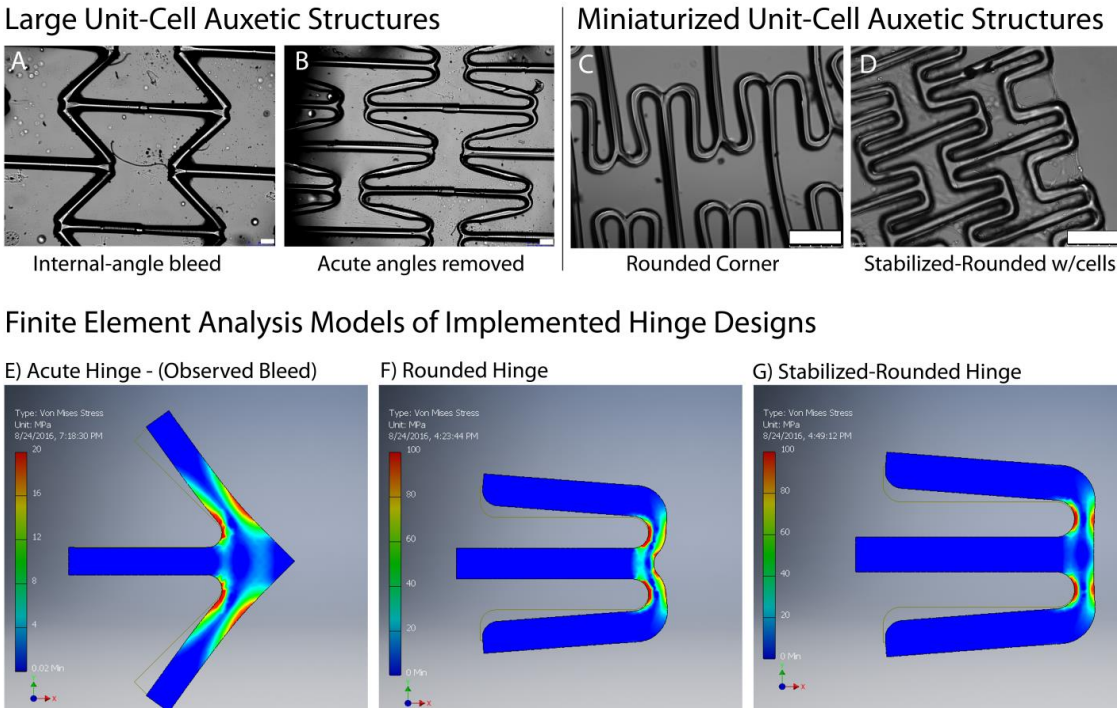

Figure 3.2: PAUA/IBOA 30/70 auxetic hinge fabrication and modeling. Hinge design analysis: (A,B) PAUA/IBOA unit-cell structures of a tiled mesh with different hinge configurations found in (E,F) at large scale. (C,D) PAUA/IBOA unit-cell structures of a tiled mesh with different hinge configurations found in (F,G) at quarter scale. (E,F,G): FEA of unit-cell hinge design to show where force persists and in order to choose materials to tolerate expected strain while also moving correctly. FEA was performed in Autodesk Inventor simulation with material properties for BR-7432GI30. Bottom face is fixed. Static analysis type "spring" k. 0.010 N force applied. Modeling W45 um x L160 um x D80 um structure. Scale bar = 250 μm. Scale bar of E is 0 to 20MPa.

Two redesigned hinge concepts were implemented into individual single layer PAUA/IBOA meshes shown in Figure 3.3A and Figure 3.3B. Each structure had auxetic regions flanked by non-auxetic honey-comb regions to enable more uniform actuation and demonstrate that multiple stretching behaviors can be achieved on a single scaffold. The associated displacement maps were compared to show that the overall stiffness of the meshes were tunable. The structures were examined during actuation to infer functionality was achieved and that the structures were sufficiently robust to handle.

Displacement maps were created through observed displacement in correlation with a force transducer as seen in setup Figure 3.3C of an axially-offset multilayered scaffold. Figure 3.3A rounded-hinge auxetic region shows a large displacement (y-axis) with less force (x-axis) providing a steeper slope than the non-auxetic honey-comb regions that elongate minimally along the structure axis. Figure 3.3B shows the stabilized-rounded hinge mesh as a less soft auxetic region evident from a shallower displacement curve slope. As expected from the stabilized-rounded hinge structure FEA modeling in Figure 3.2G, a single layer mesh structure with this sub-unit was observed to function as intended. Flexion was more localized to hinge regions and the unit-cells transmitted more movement throughout the structure more effectively than Figure 3.3A, which showed more unit-cell collapse and out-of-plane deflection. Both structures showed better unit cell range of motion than acute-hinges found in the original structure found in Figure 3.1B. Figure 3.3B shows improved handling with more uniform actuation of the unit-cells that transmit force more effectively to neighboring unit-cell subunits. The changes made to the hinge structures achieved tuned stiffening as demonstrated by the displacement mapping to be more in line with expectations for mouse muscle cell stretching. Additionally, the non-auxetic honey-comb regions in Figure 3.3B were thinned to match cross-sectional area and architecture feature size of the auxetic region. The non-auxetic regions in Figure 3.3A show almost no slope then fracture at 0.2, while Figure 3.3B shows stretching to 0.2 and then fracture. To accommodate a functional structure more suitable for tissue

growth, axially-offset multilayer structures were constructed in Figure 3.3C to demonstrate more robust displacement maps with more 3D construct meshes, where mesh softness is retained in the auxetic region and honey-comb elongation shows more common exponential curves. Scanning electron microscope images more effectively show the detail of the negative Poisson's ratio in Figure 3.3D, and the same stabilized-rounded hinge concept applied to a zero Poisson's ratio in Figure 3.3E structure despite being normally semi-transparent to light when using PAUA/IBOA.

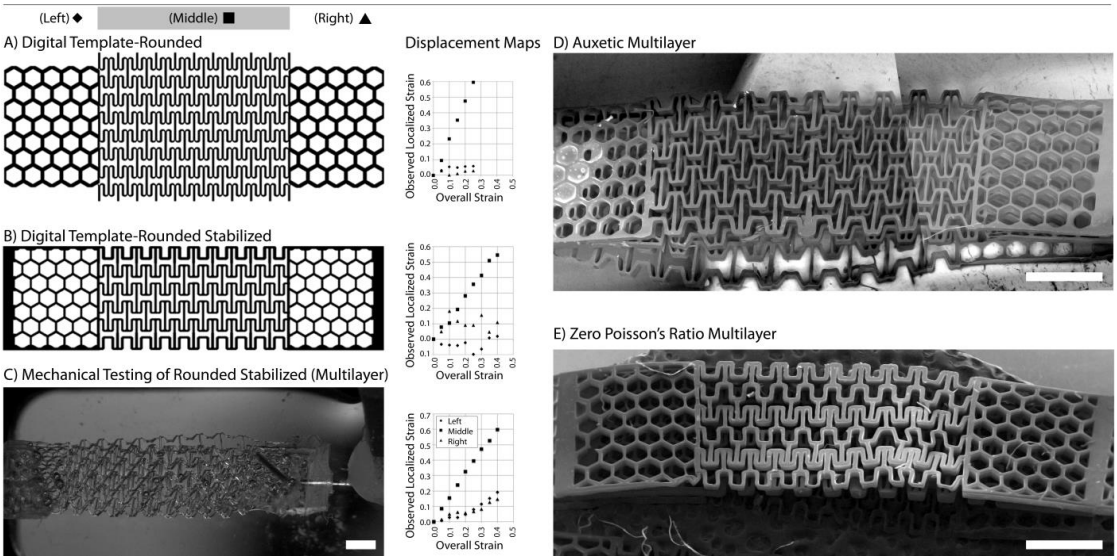

Figure 3.3: Altering tiled scaffolds and changes in displacement maps. Tiling and tunability of sheet structures to change displacement maps: Force to stretch the scaffolds changes with hinge-designs (A-ROUNDED, B-STABILIZED ROUNDED) as seen in displacement maps (Overall Strain = Force / Observed equals stretch) wording comes from how the measurements are taken. C shows multilayer and device, D and E show unit structure flexibility and application to produce layer offset unit cells for tissue in NPR and zero PR configurations. Scale bar = 1 mm

To justify implementation of scaffolds as supporting structures for living tendon and muscle tissue the following in vitro studies were conducted with tissue-appropriate fibroblast and myoblast cells. Physisorbed fibronectin was

used as a cell adhesive coating on dry polymerized PAUA/IBOA (BR7432IG30) structures. Though this commercial material likely suffers from conventional polyurethane synthesis drawbacks, the polymerized structure was soaked in chloroform for 10 minutes to induce structure swelling of 100-200% in order to flush out potential isocyanates and other latent monomers (e.g. IBOA), which may leach from the structure during cell culture. The scaffold was thoroughly dried to remove chloroform solvent. The coated scaffolds were used to culture cells.

Cell culture results on these structures demonstrate with cell viability that growth is supported, and with motile capability evident from cells spanning gaps at this scale, that the architecture is acceptable for tissue formation. Additionally fibroblasts and myoblasts constitute the majority of cell types found in muscle-tendon transition areas. Figure 3.4A shows murine fibroblasts adhering to a polymerized PAUA/IBOA fibronectin coated scaffold at the planar face. Figure 3.4B shows mid-structure cell profiles elongating in the scope perspective that adhere laterally to structure walls. This observation suggests that fibronectin is coating side walls in addition to “normal’ surfaces. Figure 3.4C shows that murine myoblasts are even capable of spanning architecture gaps at 3 weeks time. Figure 3.4D shows acceptable cell death that could be improved with another “green” polyurethane material in the future. These structures were all seeded at a density of 2×10^4 cells/structure. Surface imaging of the myoblast seeded multilayer scaffold for F-actin and nuclei shows lateral wrapping transverse to elongation. However, deeper

imaging of the multilayer scaffold shows cells flowing along unit-cell wells and normal to the planar surface despite the layered pattern offset. Additionally, multilayer scaffolds are less than the 500 μm recommended diffusion limits for normal static cells. Figure 3.4C shows even muscle cells can span the gaps.

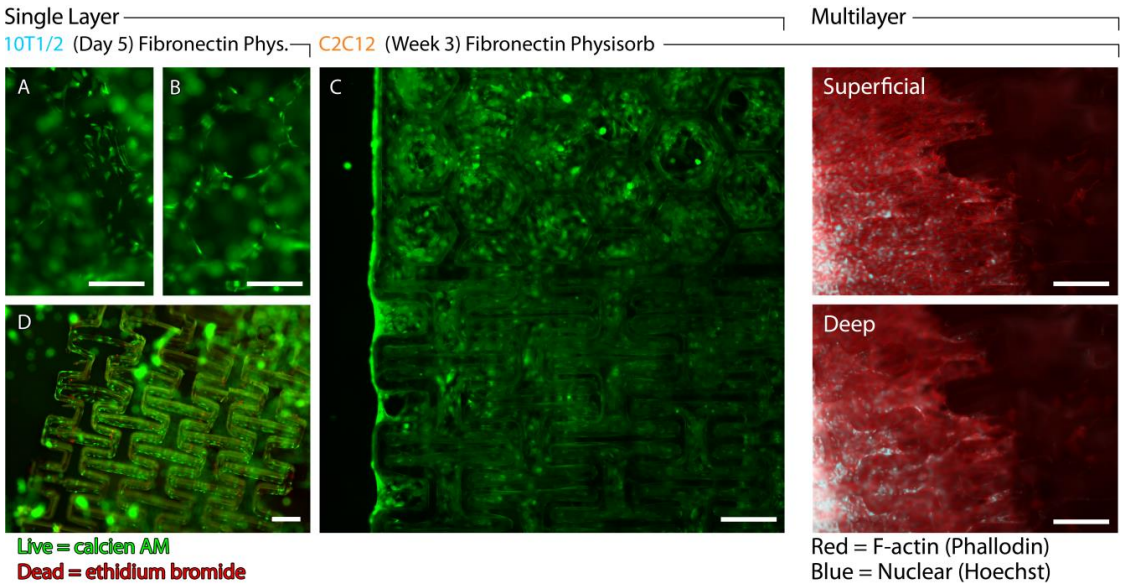

Figure 3.4: Cell adhesion and cells filling gaps on fibronectin coated PAUA/IBOA 30/70 scaffolds. Cell viability and assessment on PAUA/IBOA scaffolds (scale bars = 250 μm)

Multilayer structures facilitate gap transitions. When comparing fibroblast cultured single layer images (Figure 3.4C), which still have a few gaps, to myoblast cultured multilayers (Figure 3.4 “Superficial/Deep”), it appears and intuitively may make sense that the staggered layer provides a bridging element for the cells. Noting that the cell types are different and the z gap is 160 um. This may be better than the single layer approach, as there appears to be no unfilled unit gaps on the visible exterior regions. Fibronectin may be spanning the gap, however no floating extensions or cell bodies were observed, which may indicate the cells span these gaps. From the Figure

3.4Deep, nuclear stained cells appear to pouring out of the unit regions (normal to a frontal plane) and aligning along the well edges. The superficial cells seem to be forming a surface sheet on the transverse to the elongation axis. This behavior has been observed previously with cells while being stretched.

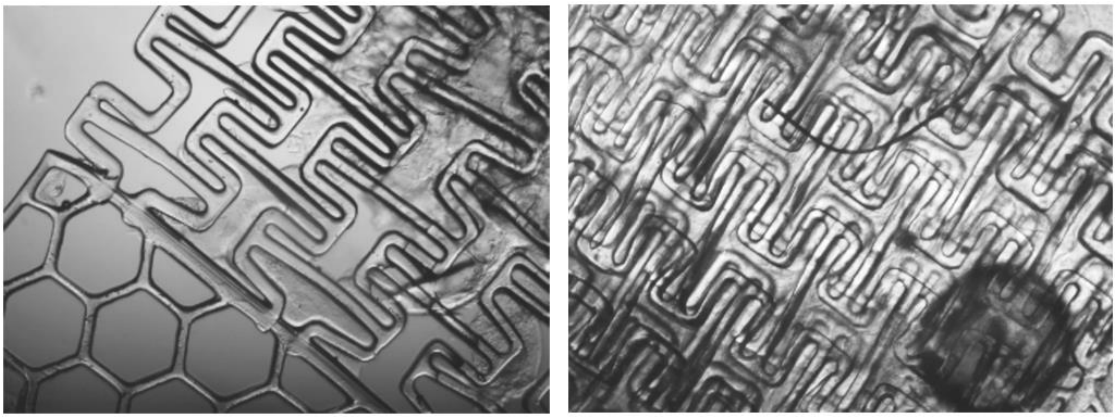

Figure 3.5 A coupled dynamic auxetic skeleton scaffold (CoDASS) embedded in a hydrogel. PAUA/IBOA 30/70 skeleton embedded in alginate. LEFT: positive to negative Poisson's ratio transition of embedded single layer after stretched and clamped at honeycomb region. RIGHT: negative Poisson's ratio (auxetic) region of multilayer embedded in alginate after stretching.

In efforts to combine the region localized dynamic motion of the unit-cell meshes, reduce the void space within the unit-cell, and apply these characteristics to hydrogel structure without need for vascularization, a "skeleton-reinforced hydrogel" concept inspired by Cha and Soman was created at less than a 500 um thickness[70]. The PAUA/IBOA multilayer structure shown in Figure 3.4D was used as a skeleton scaffold that was pre-tensioned in a mould filled with photon induced alginate-acrylate prepolymer. After alginate polymerization, the skeleton was found to induce a lesser overall auxetic movement in the normally non-auxetic alginate bulk, while the bulk

alginate limited the range of movement of the auxetic skeleton (Figure 3.5). Depending on the extent of skeleton pre-tensioning prior to alginate polymerization, the axial-transverse expansion ratio was constrained around the ratio of the skeleton at that pre-position. The elasticity of the alginate appeared to be the prime attribute to control the maximum extent of stretch, as comparison to notably less elastic 3% gelatin-methacrylate showed internal skeleton tearing at 50% stretch. Both gelatin methacrylate and alginate did not show strong adhesion to the polymerized PAUA/IBOA skeleton suggest that sliding may occur at the material interfaces. The alginate casing was cycled 5 times prior to imaging. As cell structure dimensions are important for diffusion, a sub-500 μm thickness was met with a multilayer to achieve better cell viability. The multilayer alginate encapsulated sample was more robust in response to stretching than embedded single layer skeletons. All (CoDASS) coupled dynamic auxetic skeletal structures suffered moderate to mild damage to the alginate at the clamping regions. The clamping mechanism crushed the alginate normal to the surface at the honey-comb contacts for single layer yet remained intact over the auxetic (non-clamped) region. Damaged alginate did not remain attached to the PAUA/IBOA skeleton, indicating that the material is not adhesive.

3.5 CONCLUSION

Dynamic optical projection stereolithography (DOPsL) was used to fabricate functional multilayered, non-positive Poisson's ratio tissue bio-

scaffolds. The reiterative design capability of DOPsL facilitated improvement of the classic “reentrant” unit-cell structure to accommodate the force and dynamic ranges experienced at smaller scales, while also being capable of using different off-the-shelf materials (PAUA-IBOA). Observation of unit-cell mesh actuation was consistent with FEA modeling leading to hinge and strut modification used to tune force-displacement curves at architecture scales capable of interaction with cell sheets, as shown in the fibroblast and myoblast cell studies. In addition, reduced auxetic behavior was induced in bulk alginate through embedding a 3D printed, dynamic multilayer auxetic skeleton. Though more effective with elastic materials, dampened coupled dynamic auxetic motion was achieved in a hydrogel-encapsulated-skeleton hybrid bio-scaffold. Despite reduced auxetic motion, such a hybrid structure demonstrates another means to locally modulate movement through skeleton confinement, which is potentially useful in tuning the axial-transverse auxetic ratio of a scaffold for multiple regions of stretch-induced cell differentiation.

3.6 ACKNOWLEDGEMENTS

The project described was supported in part by the Department of Defense (W81XWH-14-1-0522), California Institute for Regenerative Medicine (RT3-07899) and National Science Foundation (CMMI-1332681 and CMMI-1547005). UCSD Neuroscience Microscopy Shared Facility Grant P30 NS047101. We thank Dr. Richard Lieber for kindly providing the mechanical transducer with the expertise of Shannon Bremmer. We thank the UCSD

Nanoengineering Materials Research Center for SEM imaging. We also thank Helen Bae, Pengrui Wang, Hong Zhang, Sabine Faulhaber, and Wayne Neilson for their assistance.

Chapter 3, in full, has been submitted for publication of the material as it may appear in Warner, John; Wang, Pengrui; Mellor, William M.; Hwang, Henry H.; Pyo, Sang-Hyun, Chen, Shaochen, “A Photopolymerizable and Composition Tunable Polyurethane with Green ‘Click’ Chemistry.” The dissertation author was the primary investigator and author of this paper.

Chapter 4: Composition Tunable, Green "Click" Chemistry Polyurethane for Optical 3D Printing

4.1 ABSTRACT

Molecular variations of an easily tunable, "green" chemistry-based polyurethane (GCPU) were prepared and photo-printed via dynamic optical projection stereo-lithography (DOPsL) into 3D structures with spatially-localized material properties. Trimethylolpropane allyl ether–cyclic carbonate (TMPME-CC) was used to couple the unique properties of two types of reaction chemistries: (1) primary diamine-cyclic carbonate ring opening conjugation for supplanting conventional isocyante-polyol reactions in creating urethane groups, with the additional advantage of modular segment interchangeability within the diurethane prepolymers; and (2) thiol-ene (click) conjugation for non-telechelic, low monodispersity, quasi-crystalline-capable, and step-growth co-photopolymerization. Infrared spectroscopy (FTIR) was used to confirm these processes' associated molecular products. The extent of how these processes' molecular tunability affects material properties was investigated through measurement-based comparison of the various copolymer compositions: frequency-related dynamic mechanical analysis (DMA), tension-related elastic-deformation mechanical analysis (TMA), and material swelling analysis were implemented. Stained murine myoblasts cultured on GCPU slabs were evaluated via fluorescent microscopy for how "green-chemistry" affects cytocompatibility and cell adhesion. Functional 3D devices were optically printed with high resolution via DOPsL, thus

demonstrating the capability to spatially pattern different materials in a controlled manner. This novel, tunable synthetic process for isocyanate-free PU is readily-applicable to light-based 3D printing technologies via click chemistry, and may be useful for implementation in future biomedical applications.

Keywords: 3D printing, polyurethane, green chemistry, isocynate-free, click chemistry

4.2 INTRODUCTION

The rising popularity of 3D printing usage in biomedical applications has renewed interest in photo-printable polymers with tunable and biocompatible properties[40,42,71–74]. Indeed, many naturally biocompatible and covalent polymer systems, such as proteins and polysaccharides (excluding DNA), have been successfully modified into photo-printable hybrid polymers via terminal acrylate conjugation or other similar methods[75–85]. These telechelic polymers use photo-initiated acrylate polymerization to tether fragmented natural polymer chains together. However, these materials are relatively fragile before and during cell integration until tissue formation[3], making these materials difficult to handle, suture, or implant[2,56,86], while also prone to deformation via swelling[87,88]. Though hydrogels are a necessity in many bioprinting applications[5], the physical properties of non-hydrogel polymers can broaden existing 3D photo-printing capabilities available to bioengineering[89].

Through increased accessibility to modular click chemistries, as well as safer, “greener” processes to generate polymer precursors, synthetic biomaterials are now better able to meet the varying needs found in medical research applications[90]. PU’s elastomeric properties[91], physical robustness[92], and low chemical reactivity have been favorably noted in bioengineering for many years[93]. However, despite being integrated into several biomedical devices[1,93–96], traditional PU has experienced implementation challenges due to toxic precursors and leeching[97,98] of chemicals such as phosgene[97,99], isocyanates [100,101], and associated degradation products[98,101]. Additional difficulties exist in acquiring commercially-available photo-polymerizable PU[74], which hamper its use in light-based 3D printing applications. While there are some commercially-available aliphatic polyurethane-diacrylate materials with desirable properties, such as the industrially-produced Dymax® BR7432IG30, they often have shortcomings. For example, the Dymax® material mixture can be used off-label as a 3D-printable material, but the incorporated acrylate plasticizer used to maintain flexibility is also acutely toxic[102].

In contrast, the ring opening conjugation reactions of six-membered cyclic carbonates with polyamines can create urethane bonds without the use of phosgene and isocynates[101,103–105]. By functionalizing the cyclic carbonate with an allyl group, UV light exposure can induce the terminal alkene to participate in a radical-mediated thiol-ene reaction with a thiol group - this functionalized cyclic carbonate can then be used to impart different mechanisms and properties to the polymer. This thiol-ene chemistry has all

the desirable features of a click reaction: high efficiency, simple execution with no side products, and quickly-produced high yields[106]. As such, in recent years, thiol-ene chemistry has been extended from use in bulk materials to hydrogels, thin films, and lithographic applications[106,107]. A process for stamp fabrication was developed for soft lithography by (A) casting liquid thiol-ene mixture onto a patterned master mold, (B) curing the material with UV and (C) peeling off the patterned polymeric stamp[108109]. Thiol–ene systems of various compositions were printed *via* inkjet and cured with a xenon flash lamp system to produce mechanically- and chemically-stable dielectric films[110]. However, thiol-ene chemistries have yet to be applied to light-based 3D printing[13,51]. Thiol-ene chemistries are suitable for photopolymerization applications – this facilitates spatial and temporal control of the click reaction[106], allowing assembly of highly-uniform crosslinked networks and polymer functionalization[111,112] for a variety of tissue engineering applications[113]. Maskless optical 3D printing has shown advantages as a mould-free, scalable additive manufacturing method with high resolution and low alteration costs[35,47], which are important factors for biomedical applications.

Here, we present a novel 3D-printable and tunable polymerization mechanism of polyurethanes networked with thiol crosslinkers via “green” click chemistry (GCPU). The chemical tunability and physical properties of this GCPU are investigated in controlling rigidity, flexibility, and elasticity while also demonstrating non-toxicity, cytocompatibility, and potential uses with photo-printable bioengineering applications via DOPsL.

4.3 EXPERIMENTAL SECTION:

4.3.1 Preparation of Diallylated Diurethane Prepolymer

5-Allyloxyethyl-5-ethyl-1,3-dioxane-2-one (trimethylolpropane allyl ether–cyclocarbonate, TMPME-CC) was prepared according to a previous report[114]. Bio-based cadaverine (1,5-diaminopentane, >99%) was generously provided by CJ Biotech (South Korea). TMPME-CC and cadaverine were mixed at a molar ratio of 2:1 in order to accommodate ring-opening conjugation with cadaverine's two available primary amines. This mixture of TMPME-CC and cadaverine was vortexed vigorously for 1 minute and then heated at 68˚C for 15 min, during which it was periodically vortexed. The resulting product, diallylated diurethane, was used with thiol compounds for photo-polymerization.

4.3.2 Preparation of Photopolymerizable Mixture

The branched thiol crosslinkers such as pentaerythritol tetrakis(3-mercaptopropionate) (>95%), trimethylolpropane tris(3-mercaptopropionate) (≥95.0%), and linear thiol 1,6-hexanedithiol (96%) were purchased from Sigma Aldrich. Darocur 1173® (2-hydroxy-2-methyl-1-phenyl-propan-1-one) purchased from Ciba Specialty Chemicals Inc. (Switzerland) was added as a liquid photoinitiator to the viscous prepolymer mixture. Various molar ratios of the multi-thiols were added to match the alkene bonds flanking the prepolymer as detailed in Table 1. Each mixture was heated to 78˚C for 5 minutes. After

heating, Darocur 1173® was added to each mixture at 2% v/v and periodically vortexed for an additional 5 minutes at 78˚C.

4.3.3 FTIR Analysis

FTIR spectra were acquired from a Perkin Elmer® Spectrum Two infrared spectrometer equipped with a UATR (universal attenuated total reflectance *crystal*) 2 module. Liquids were placed directly onto and completely covering the crystal sample window. Solid materials of various compositions found in Table 1 were polymerized into 1 mm slabs and then cut into disks with a 6 mm biopsy punch. Spectra from the face of material distal to the UV light source are reported. Spectra from material-faces were shown to be consistent at the 927 cm^{-1} peak indicating the alkene-associated carbon-hydrogen bond. This alkene-associated carbon-hydrogen bond is affected by alkene-thiol conjugation and indicative of polymerization of the material.

4.3.4 Dynamic Compression Storage Modulus

A Perkin Elmer® Dynamic Mechanical Analyzer (DMA 8000) was used to obtain storage modulus and “lossiness ratio” (tan δ) compression data. Frequency scans were run from 0.1 to 3 Hz at 5% displacement on 1 mm thick, 6 mm wide disks of the various materials found in Table 1 that had been polymerized via 365 nm UV light for 5 minutes. The frequency curve was checked for continuity and the 1 Hz point was reported in order to compare the various mixtures.

4.3.5 Tensile: Young's Modulus

GCPU films were polymerized via 2 minutes of 365 nm UV light into 0.32 mm thick and 2.2 – 2.6 mm wide films of various lengths, and then examined. A Perkin Elmer® TMA 7 running Pyris© was used to acquire tension data. Force-displacement curves were translated into stress-strain curves with the caliper measurements of the material setup conformation. The moduli of various materials were acquired as the initial slope of the "linear" elastic-deformation region of the stress-strain curve (SI Figure 4.9).

4.3.6 Swelling Analysis

The mixtures found in Table 1 were photopolymerized via 5 minutes of 365 nm UV light into slabs 1 mm thick, and then cut into 6 mm wide disks with biopsy punches. The disks were submerged in chloroform for 5 minutes, removed, and quickly measured to determine swelling characteristics.

4.3.7 Optical 3D Printing by DOPsL system setup

We carried out 3D printing of GCPU using the DOPsL setup as previously developed in our lab[12,51]: 2D bitmap computer model slices are serially-uploaded to a digital micro-mirror device (DMD) chipset (1920x1080, Discover 4000 digital light processing (DLP) chip, Texas Instruments) that display dynamically based on z-dimension height. The 2D bitmap slice information encodes a spatial pattern via tilting of individually-addressable micromirrors on the DMD chip. The tilted micromirrors reflect the UV source's light (Omnicure® S2000) through condensation optics to a focal point on a controllable sample

stage. Stage movement was managed with a stage controller (Newport, CA) to change the optical focal plane height within the sample. A 320nm~500nm filtered light spectrum is produced by Omnicure® halogen bulbs. Synchronization of spatial patterns, light exposure, and z-focus with the sample chamber was controlled by a desktop computer. GCPU liquid pre-polymer was diluted 20% v/v with 99.9% ethanol to minimize perturbing forces during rinsing of unpolymerized pre-polymer. The GCPU (80%)/ethanol (20%) mixture was physically confined with a transparent glass coverslip coated with Krytox® oil to prevent non-specific adhesion, and PDMS sheets to eliminate potential oil contamination during cellular structure printing. The material was polymerized with 365 nm UV light for 45 to 90 seconds. Various GCPU structures were constructed by sequential photopolymerization of different GCPU/ethanol pre-polymer mixtures, thus creating structures with multiple material properties.

The printed 3D structures using GCPU were rinsed with ethanol (99%), heated at 68˚C for 15 min, and then transferred to a room temperature vacuum chamber for 24 hours. The GCPU structures were sputter coated with carbon and imaged via a field emission environmental microscope (FEI XL30 ESEM FEG). Images were acquired in electron scattering mode at 10kV.

4.3.8 Biocompatibility of GCPU Material Slab Construction

GCPU square slabs were photopolymerized via the DOPsL system for 60 seconds at 6W/cm^2. They were then rinsed with ethanol, heated at 68˚C for 10 minutes, and placed in a room temperature vacuum chamber for 24 hours. Half of these materials were removed for fibronectin physisorbtion coating at a concentration of 1mg/mL dispensed directly onto the sample surface, and then allowed to incubate for 24 hours at 4˚C protected from light. Afterwards, they were transferred to a vacuum chamber at room temperature for an additional 48 hours. The dry samples were exposed to 365 nm UV light for ~30 minutes prior to use.

Murine myoblast (C3H/10T1/2, Clone 8, CCL-226™) cells from ATCC® were cultured based on ATCC guidelines. The growth medium consisted of high glucose DMEM (Gibco), (inactivated) fetal bovine serum (10% v/v) (Hyclone), and L-glutamine (1%) (Gibco). Penicillin/streptomycin (50 units/mL) (Gibco) was added to the culture medium used during material-cell incubation. Cells were incubated at 37˚C with a gas mixture of 5% CO_2 and were sub-cultured prior to confluence. Cells were used at passage 6 and seeded on both fibronectin-coated (physisorbed) and naked 050-050-000 GCPU slabs. The GCPU 050-050-000 slabs were seeded with a 10 uL drop containing 2 x 10^4 cells and then incubated for 20 minutes at 37˚C, after which the sample wells were carefully flooded to fully submerge the slab in complete growth medium.

C2C12's were seeded on polymerized GCPU 050-050-000 with and without fibronectin coating. A LIVE/DEAD® Viability/Cytotoxicity kit for mammalian cells from Thermo Fisher Scientific was used to assess cytotoxicity on culture days 3 and 5. The culture media of each sample was removed and rinsed 3 times with an equivalent volume of DPBS (pH 7.4) before adding 150 µL of a cell-staining solution containing 2 µM calcein AM and 4 µM ethidium bromide in DPBS (Gibco) as per Thermo Fisher guidelines. The cells were covered from light and then incubated with the staining solution at room temperature for 30 minutes. After incubation, the cell staining solution was removed, rinsed with 3 equivalent volumes of DPBS (pH 7.4), and then imaged using a Leica DMI 6000B microscope at the 10x objective, with tiling functionality. Bright field and fluorescent images were taken, and a longer exposure time for the ethidium dye was used to enhance imaging of any dead cells against the fluorescent background.

4.4 Results and Discussion:

4.4.1 Functional Diurethane Prepolymer and Polyurethane Copolymers

The ring opening conjugation -of six-membered cyclic carbonate with amines has attracted attention over the use of five-membered chemistries in producing PUs without phosgene and isocyanate[103,105,115,116], due to the more reactive and thermodynamically-favorable reaction involved[115]. Figure 1 shows an easily-tunable, "green" thiol-ene click-chemistry synthesis of PU using TMPME-CC. There are two sequential reaction steps, consisting of an initial

reaction of amines to produce diurethane, after which UV light is used to facilitate crosslinking and thiol-ene polymerization. Urethane groups can be generated from a catalyst-free thermal reaction of TMPME-CC with an amine group, and the allyl functional group can be used to attach various thiols capable of imparting different properties to the polymer.

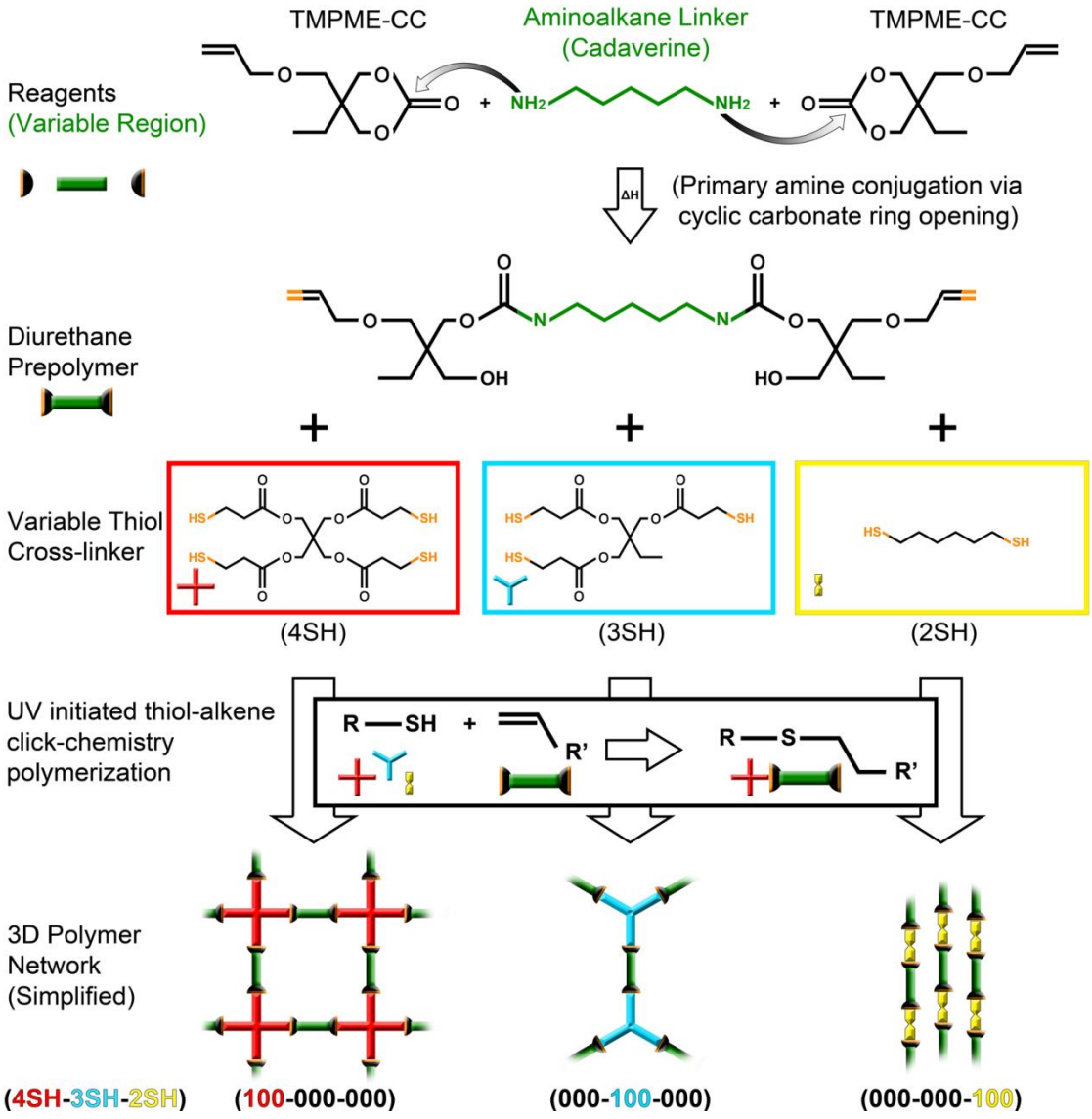

Figure 4.1: Schematic of the GCPU copolymer polymerization system chemistry. Synthesis of diallyl urethane prepolymer from diamine and TMPME-CC by heating, followed by UV-photo-initiated free radical thiol-ene polymerization with branched variable thiol crosslinkers, to create a 3D polymer network.

Various polyamine linkers, including biogenic materials such as putrescine, cadaverine, spermidine, and spermine, which are non-toxic biogenic metabolites in essential biosynthesis pathways, can be used to affect the degree of crosslinking[117,118], site-specific degradation, as well as the physical properties of the resulting polymers. In this study, cadaverine was used in this material comparison due to its structural simplicity and ubiquity as lysine's decarboxylation product in protein putrefaction. The cyclic carbonate ring opening of TMPME-CC does not require phosgene, nor does the reaction to obtain the "green" alkene monomer linker (allylated direthane prepolymer) in Figure 4. 1 require any isocyanate or additional catalysts, although the reaction was accelerated with heating (70˚C). This reaction uses a 2:1 molar ratio of TMPMECC to cadaverine. The resulting alkene-functionalized diurethane was incorporated with various ratios of branched multi-thiols, and then photopolymerized via UV light into thiol-ene crosslinked PUs.

FTIR spectra of the products and reactants were used to confirm transformation of functional groups (Fig.2). The formation of diurethane from ring opening of TMPME-CC with polyamine was monitored with a peak at 1752 cm^{-1}. As this cyclic carbonate-associated carbonyl peak (Fig. 2b) diminishes, a new carbonyl peak from urethane formation appears at 1695 cm^{-1}, which coincides with the appearance of a broad hydroxyl peak (3200-3600 cm^{-1}) and is characteristic of ring opening at the carbonate linkage (Fig. 2c) with an amine to form the diurethane monomer.

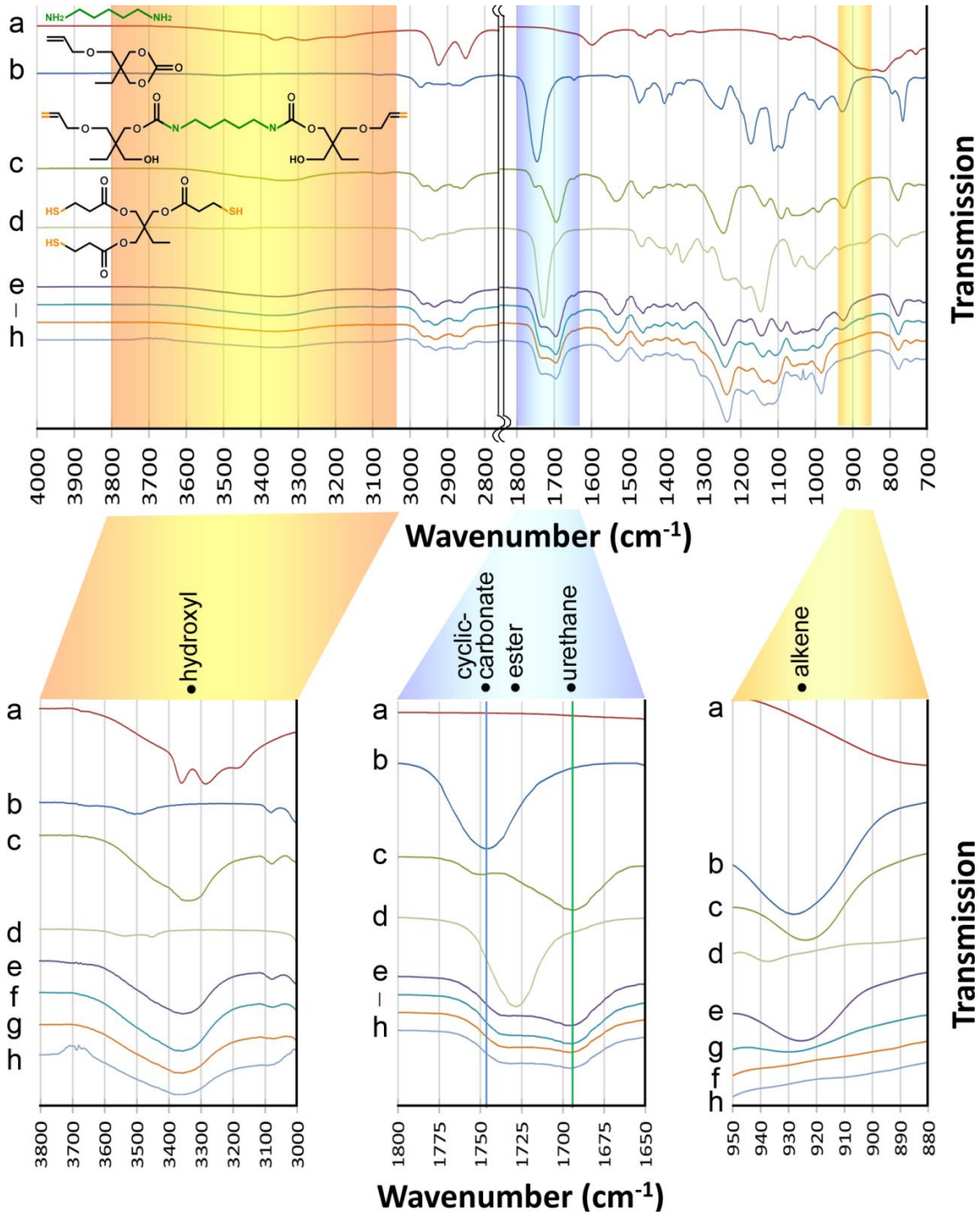

Figure 4.2: FTIR spectra of molecular precursors and products**.** (a) cadaverine heated with (b) TMPME-CC [5-allyloxyethyl-5-ethyl-1,3-dioxane-2-one (trimethylolpropane allyl ether–cyclocarbonate)] to create (c) diallyl urethane confirmed with replacement of cyclic-carbonate peaks with urethane (O=C-N) and hydroxyl (-OH) peaks. (d) (3SH) = trimethylolpropane tris(3-mercaptopropionate) mixed with (c) yields (e) and is exposed to 365 nm light for (f) 2.5 min. (g) 5 min. (h) 10.0 min. The peak at 927cm-1 indicative of the alkene diminishes with time and shows no difference between (g) and (h).

UV-induced free-radical polymerization of functional diurethane monomers was inferred via the peak at 927 cm^{-1} (Fig. 2) diminishing with UV exposure; this peak correlates to the C-H bond of the mono-substituted alkene in the allyl group being transformed into a thiol-ene sufide bond. Fig. 2e's spectra (0.0 minute at 365 nm), demonstrates a maximum FTIR peak of available alkene for thiol-ene polymerization, which diminishes with exposure to UV light. 2.5 minutes of UV exposure shows a partial decrease of the "alkene" peak, while 5 minutes shows a complete decrease, which was confirmed via no additional significant change in spectra after 10 minutes of exposure (Fig. 2h). FTIR spectra confirmed GCPU functionality as a photopolymerizable PU utilizing "green" click chemistries.

4.4.2 Tunable Synthetic Process and Characteristics of Isocyanate-free GCPU

Three multi-thiols were chosen to examine crosslinking, charge differences, and entropy effects on the GCPU: 1) branched tetra-thiol (4SH, pentaerythritol tetrakis(3-mercaptopropionate)), 2) branched tri-thiol (3SH, (trimethylolpropane tris(3-mercaptopropionate)), and 3) linear di-thiol (2SH, 1,6-hexanedithiol).

To evaluate the created compositions, we examined these materials in a tetra-thiol (4SH), tri-thiol (3SH) and di-thiol (2SH) format as shown in Table 1 (Material 4SH-3SH-2SH), with a naming convention to aid in understanding the data. The allyl diurethane was kept constant as a uniform-length linear molecular segment using the cadaverine-only chemical configuration.

Additionally, the thiol-ene chemistry creates an alternating alkene-thiol copolymer chain[119]. In eliminating allyl diurethane as a variable and relying on the documented alternating thiol-ene mechanism, the naming convention of GCPU materials was simplified – we normalized the number of alkene-thiol bonds based on the contributing thiol, thus weighing the crosslinking based on source instead of merely the number of molecules. As an example: an equal molar mixture of tetra-thiol and tri-thiol molecules will have the tetra- bonds responsible for 33% more of the total interactions, and thus is labeled as GCPU Material 057-043-000, which may not be immediately clear. Such naming conventions are meaningful in classifying low monodispersity thiol-ene reactions capable of quasi-crystalline[89,120] arrangement. Table 4.1 explains a common way to interpret the GCPU compositions, and facilitates normalized analysis based on such factors as expected bonds, molar concentration, and expected crosslinking. Establishing this nomenclature is critical to understanding the GCPU's mechanical data and its mechanisms of tunability for optical 3D printing.

Table 4.1: GCPU Material Compositions

Visual Representation	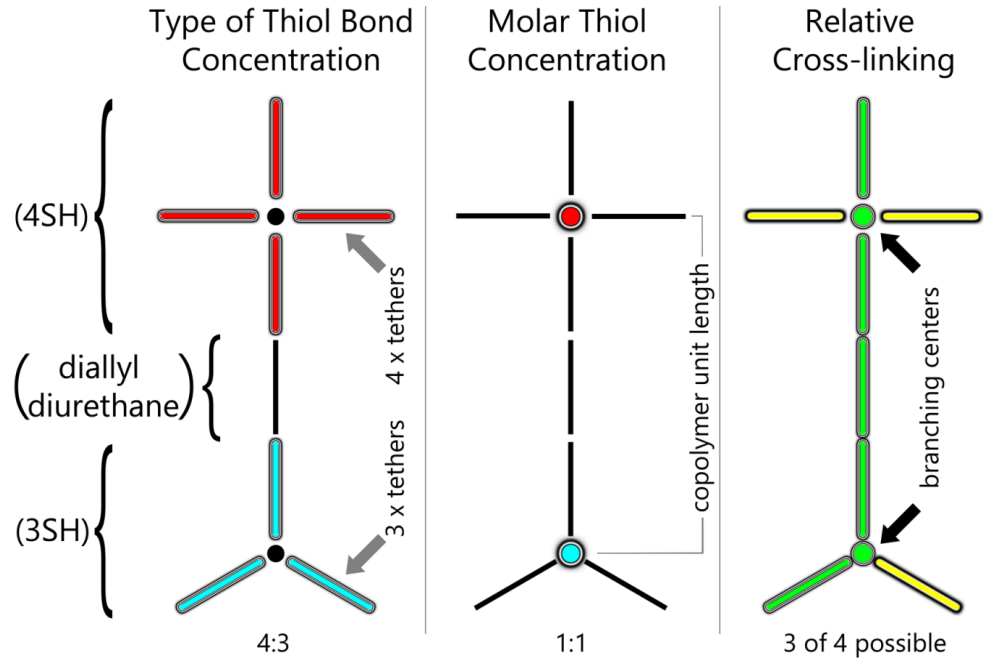		
Description		[Default Reference] Estimated percentage of thiol-ene bonds categorized by multi-thiol	(RTC) Relative Thiol Content Conventional molar ratio of ONLY multi-thiol variants	Relative Strand cross-linking (RXL): Available crosslinking to a single continuous molecular chain per unit, given chemistry used. (yellow = crosslinking)
GCPU Material Mixtures				
		4SH-3SH-2SH	RTC-4SH-3SH-2SH	Relative strand crosslinking %
		100-000-000	RTC-100-000-000	100
		070-030-000	RTC-064-036-000	82
		050-050-000	RTC-043-057-000	71
		030-070-000	RTC-024-076-000	62
		000-100-000	RTC-000-100-000	50
		040-040-020	RTC-030-040-030	50
		033-033-033	RTC-023-031-046	38
		050-000-050	RTC-033-000-066	33
		000-050-050*	RTC-000-040-060	20
		000-000-100**	RTC-000-000-100	0
	*Formed solid initially. Capable of being cut and handled. Reverted to a viscous drop within 24hours at RT. Mixture not tested. ** Did not form a solid material. Mixture not tested.			

Dynamic mechanical analysis was used to compare compression properties observed in GCPUs prepared using different ratio of thiols. As expected, the most crosslinked GCPU (Material 100-000-000), which is comprised of tetra-branched functional thiol molecules, was the most rigid and least compressible polymerized compound. A 1 mm thick GCPU slab structure of 100-000-000 (4SH only), when folded onto itself (180°) and pressed, was observed to tear along the fold line due to the stress.

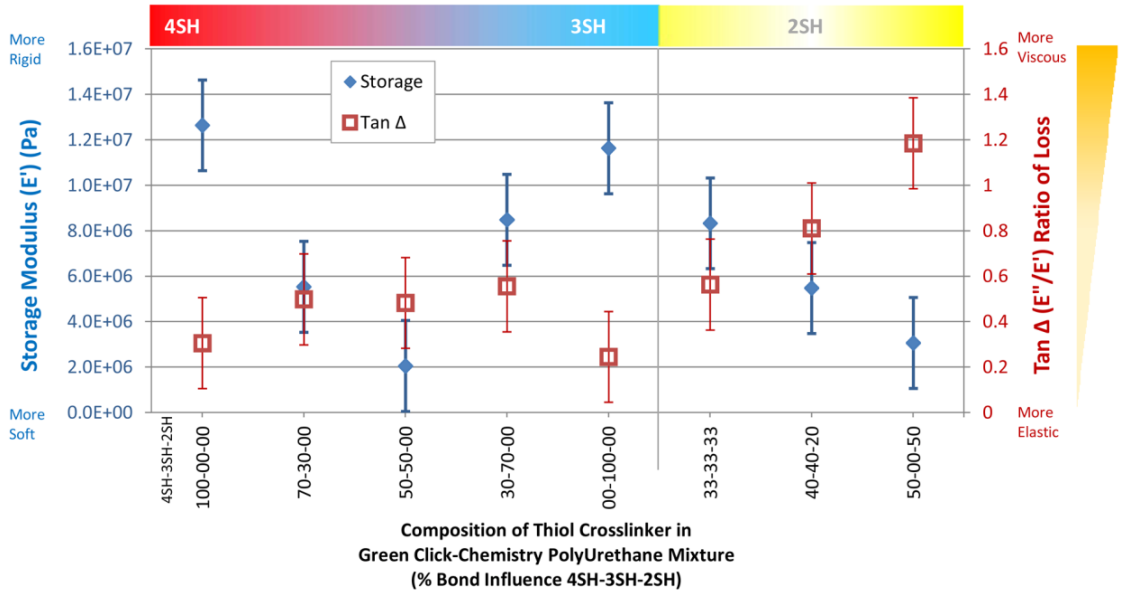

Figure 4.3: Compression testing by dynamic mechanical analysis. Compositions of thiol crosslinker of GCPU evaluated based on mixtures found in Table 1 measured for storage modulus and ratio of loss Tan δ. (4SH) = pentaerythritol tetrakis(3-mercaptopropionate, (3SH) = trimethylolpropane tris(3-mercaptopropionate), and (2SH) = 1,6-hexanedithiol.

Meanwhile, the GCPU slab structure of 000-100-000 (3SH only), which was instead comprised of tri-branched thiol, was nearly as compressible as 100-000-000 yet was sufficiently flexible to tolerate self-folding without the tearing seen in 100-000-000. Both variants likely represent a quasi-periodic crystalline structure previously observed by the Hoyle/Hawker groups as

“pure” thiol-ene mixtures[92,121], suggesting that the tri-thiol packing structure tolerates more molecular-layer slipping. Material compressibility is related to storage modulus E’ data, which evaluates elastic response. The damped viscous-related loss modulus E’ response is statistically proportional to the storage modulus across both tri-thiol and tetra-thiol GCPU materials, therefore providing a moderately consistent tan δ, “ratio of loss,” for these materials at room temperature (Table1 and Fig. 3). Mixtures of 4SH-3SH show slightly higher room temperature tan δ values, illustrating a peak shift towards higher temperature with molecular species entropy. This data is consistent with Senyurt et. al., whom showed a similar relation to network “disorder” using the same tri-thiol, but instead varied the copolymer with ratios of two different length alkene molecules[120]. The “pure” longer alkene molecule permitted greater entropy, and revealed a low, broad tan δ curve with a peak shifted into higher temperatures. Since the tetra- and tri- thiols used for GCPU have the same arm structure, and pure tri-thiol tan δ values return to pure tetra-thiol tan δ values, greater disorder in the periodic structure likely occurs due to molecular packing differences in tetra/tri-thiol mixtures. GCPU material 050-050-000, where half the supporting bonds are tetra- crosslinked and half are tri- crosslinked, revealed interesting information about its internal organization: 050-050-000 was observed to be the softest and most flexible material with the lowest storage modulus (Fig. 3) and comparatively resistant to stretching (Fig. 3). Materials 070-030-000 and 030-070-000 were formulated in an attempt to confirm this trend and reveal similar “softening”, yet the storage

modulus data of 050-050-000 is more similar to 070-030-000 than 030-070-000. This data suggests that entropy arising from molecular species concentrations has a stronger correlation to storage modulus rather than from the bond sterics of branching thiol copolymers. This also suggests that GCPU material 057-043-000, or an equi-molar concentration of tetra- and tri- thiol species, would likely have the most disorder, the softest modulus, and strongest tan δ shift of the tetra/tri thiol blends.

The GCPU prepared from linear-thiol mixture 000-000-100 (2SH only) with no theoretical crosslinking between chains (Table 1) was polymerized into a notably viscous, sap-like liquid, indicating an inability to form a solid at room temperature. GCPU material 000-050-050 yielded a temporarily deformable solid, that after 24 hours, reverted to a drop-like shape consistent with the behavior of extremely viscous liquids (SI Figure 4.8). Given these limitations, the effects of linear thiol linking were examined through mixtures coupled with tetra-thiols and tri-thiols. By comparing Material 050-050-000 with 033-033-033, we observe the addition of linear thiol to a “disordered” system (050-050-000) increases the storage modulus while having little initial effect on tan δ – this is likely because the addition of linear thiol may contribute to alleviating steric strain from irregular molecular packing. When linear thiol concentrations are reduced from the 033-033-033 equivalent di/tri/tetra thiol mixture, and tetra/tri thiol ratios are maintained, as seen with 040-040-020, the storage modulus is partially restored toward 050-050-000’s values and the “ratio of loss” increases. A higher temperature peak shift of tan δ caused by structural

relaxation from adding linear thiol is consistent with Senyurt's observations. However, when the quasi-crystalline structure[107,120] of tetra-branched bonds is supplemented with an equal number of linear bonds, such as in GCPU 050-000-050, the polymer behaves similarly to traditional acrylate polymers in that increasing the telecheic monomer length increases overall softness. Thus, the storage modulus is very low while the tan δ is comparatively high.

GCPU copolymer unit length and crosslinking frequency are coupled as seen in the polymerizing mechanism of Figure 4.1. Thiol-ene polymerization produces an alternating multi-thiol and diallyl diurethane chain structure. Under the reaction conditions used, tetra-thiols and tri-thiols provide crosslinking centers of uniform molecular separation[92]. Assuming ideal mixing, when an equal number of dithiol bonds are introduced to a tetra-thiol-only GCPU material, the length between crosslinking points doubles based on the approximate interval chain length of [100-000-000] = 40 vs. [050-000-050] =74. Comparison of the storage modulus data of GCPU materials 100-000-000 and 050-000-050 shows ¼ reduction, while the "ratio of loss" increases by about 4. This phenomenon is different from many telechelic acrylate polymers where increasing the monomer weight does not influence crosslinking frequency of the polyacrylate chain.

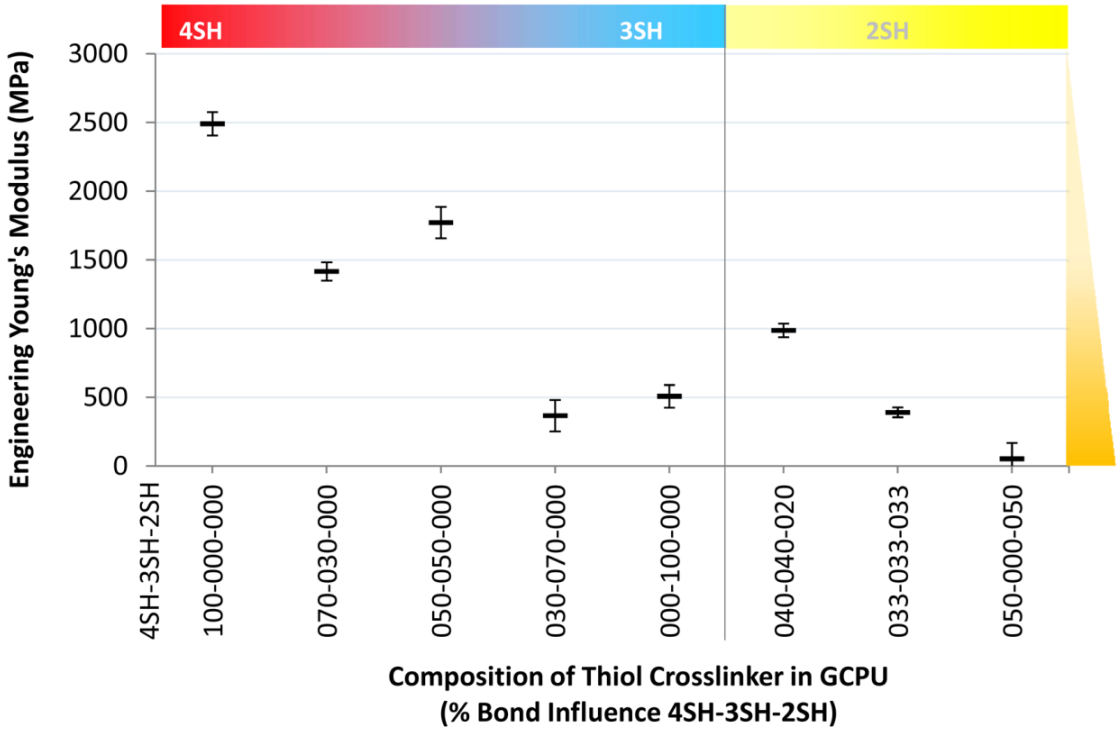

Figure 4.4: Tension testing for engineering Young's modulus. Compositions of thiol crosslinker of GCPU evaluated based on mixtures found in Table 1 measured for elastic deformation. (4SH) = pentaerythritol tetrakis(3-mercaptopropionate, (3SH) = trimethylol-propane tris(3-mercaptopropionate), and (2SH) = 1,6-hexanedithiol.

The stress-strain data details the forces required to deform or stretch a given material (SI Figure 4.9). Figure 4.4 shows a general trend where increasing the concentration of tri-thiol crosslinker reduces the force required to elongate the polymer film. When increasing the concentration of linear di-thiol, there is a stronger reduction in required elongation force. Materials with smaller Young's moduli tend to stretch farther than stiffer materials with the same force, however the majority of the materials encountered mechanical failure at the grip-material interface, thus their material failure data is inconclusive. As seen in Figure 4.4 data, the more rigid tetra-only thiol Material 100-000-000 had the highest storage modulus and was resistant to stretching.

However, we found that the mixed tetra-/tri-thiol Material 050-050-000 had a very low storage modulus, yet was resistant to stretching; and the tri-only thiol material 000-1000-000 had a high storage modulus, yet had high stretchability. These seemingly mismatched set of characteristics demonstrate the potential tunability of thiol-ene network to create materials with varying rigidity, flexibility, and stretchability. The elastic-deformation modulus shows higher correlation to the type of bond branching rather than expected crosslinking or storage modulus as seen in Table 1.

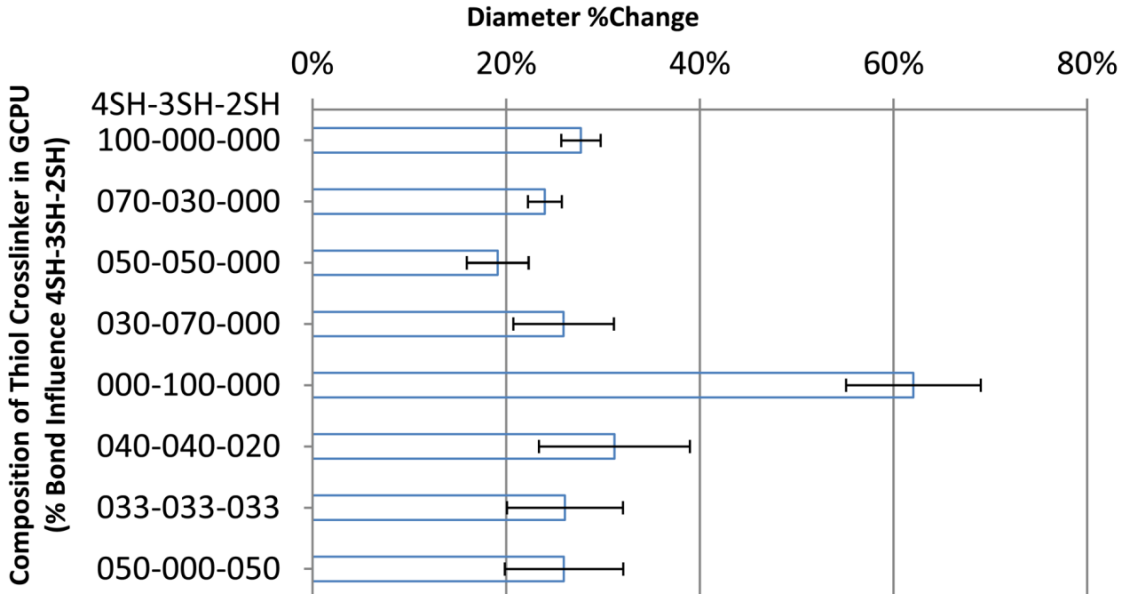

Figure 4.5: Swelling analysis of GCPU material mixtures. Compositions of thiol crosslinker of GCPU evaluated based on mixtures found in Table 1 swelling in cholorform based on disk diameter changes. (4SH) = pentaerythritol tetrakis(3-mercaptopropionate, (3SH) = trimethylol-propane tris(3-mercaptopropionate), and (2SH) = 1,6-hexanedithiol.

The interpenetrating networks of polymers are difficult to examine once polymerized because the repeating units are large and flexible compared to crystals while still persisting as one large covalent macromolecule. Conventional methods for understanding bulk crystalline periodicity often rely

on deconvolution of scattering spectra from highly-organized, immobile, periodic structures. To circumvent these challenges, we use the amount of swelling to infer polymer network spacing and packing, assuming that the molecular bonds between branched cores are approximately the same, and that the intermolecular solvation force between segments of the copolymer system is approximately uniform at equilibrium[107,120]. Because the GCPU swelling data found in Figure 4.5 is dependent on the polymer network, there is less surprise that the swelling data agrees well with the storage modulus data, showing the highest values for tetra-thiol 100-000-000 and tri-thiol 000-100-000 and the lowest values for 050-050-000 and other tetra/tri thiol blends. This swelling data reinforces the concept that a space-filling phenomenon with tetra/tri thiol blends is creating more dense and restrictive networks. The linear thiol materials' storage modulus data show slightly amplified ratios and larger error likely because the longer molecular chain lengths between branched cores permit more flexion. The tri-thiol material swells to the highest degree, deviating from the tetra-thiol dominance in the storage modulus data. This abnormal swelling behavior indicates that the interval between network-anchored crosslinked bond lengths may be longer than expected for tri-thiol GCPU. Additionally, the storage moduli are high, suggesting an ordered packing regime such as laminar or sheet-like organization. While this was the only material where swelling tests were partially destructive due to rapid influx of the solvent, chloroform did not dissolve this material even after 1+ week of submersion.

4.4.3 Biocompatibility of GCPUs

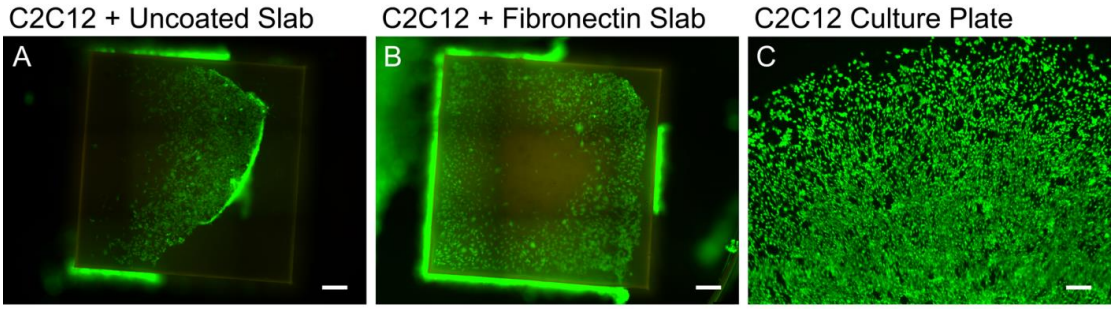

Figure 4.6: Cell live/dead assay: Murine 3T3 C2C12 mybloasts grown on GCPU for 5 days. Green = Calcein AM, Red = Ethidium Bromide. (A,B) GCPU materials 050-050-000 were tested. Uncoated (A) and physisorbed fibronectin (B) were examined to determine cell death. (C) Culture plate control. Structures were inverted for imaging. (Scale bar = 250 μm)

Conventional PU production often involves toxic components such as isocyanates and phosgene. The process for GCPU production eliminates these contaminants, making it more suitable for biomedical usage[97,98]. The ring-opening conjugation of cyclic carbonate with amines is an isocyanate-free process, and creates aliphatic PUs consisting of aliphatic carbamates, biogenic diamines, and thiols. Additionally, based on our understanding of GCPU synthesis and structure, GCPU without physicochemical or charge modification provides few motifs for cell adhesion. Since non-adhered cells tend to die, we grew high-density cell sheets on GCPU slabs to test for any potential cytocompatibility issues, relying on the aggregate cell-cell contact to improve survivability. Figure 4.6A shows a GCPU slab tilted upside-down, the cell sheet has separated from the GCPU slab and is falling ‘forward’ from the viewer’s perspective toward the base of the plate. The living cell sheets were in direct contact with the GCPU slabs, but adhesion was sufficiently weak such that an air bubble was capable of displacing the cell sheet (SI Figure 4.10).

The fluorescent images in Figure 4.6 A-B suggest minimal cell death (~3%) in response to prolonged GCPU contact as compared to the control (Figure 4.6C) ~4%. In Figure 4.6A-B, the murine C2C12 cells on a slab of GCPU 050-050-000 proliferate under aggregated cell conditions despite lack of strong cellular adhesion and show little-to-no toxicity effects after 5 days of culture. Physisorbed fibronectin (Figure 4.6B) did not substantially improve cell sheet adhesion to GCPU, however the cell sheets appear to show less clumping at the periphery. Cells from the surrounding polystyrene plate grew up to and around the GCPU slabs, as many cell sheets were found adhered to the culture plate. Based on the cell viability data, no acutely toxic effects were observed with the GCPU.

4.4.4 3D-printed Multi-Mixture GCPU Structures

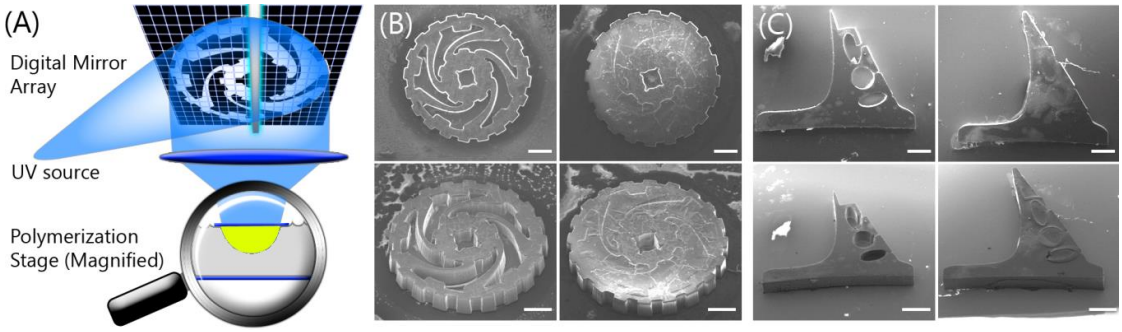

Figure 4.7: Optical 3D Printing of GCPU materials: schematic of the DOPsL setup (A) with SEM images of printed GCPU structures. (B) A simple torque gear for dampening accelerations. (C) A pulsatile-flow cantilever valve. (B,C) Left images: More rigid material printed first. Right images: Compressible, damped, flexible, and elastic materials printed second. (Scale bar = 500 μm)

DOPsL was used to photo-print different GCPU mixtures into 3D devices designed to possess spatially-dependent storage moduli, Young's moduli, flexibility, and stretchability. Figure 4.7A shows the DOPsL system

schematic: UV-light illuminates a patterned digital mirror array, reflecting an optical pattern through focusing optics onto a moving stage containing GCPU prepolymer, thus photopolymerizing a 3D object. Figure 4.7 shows various SEM images of 3D-printed GCPU structures. Figure 4.7B shows a directionally-biased semi-rigid gear with rotational dampening of acceleration. The design comes from wheels of NASA's Mars Pathfinder Rover that absorb tangential shock, however the same concept can be used to absorb or dampen rotational shock. The rationale is that miniaturized mechanical systems experience increased force-to-weight ratios - as artificial implants become more complex, they will require protection against damage to their internal assemblies, such as a step-down gear for mitigating high rotational forces. In the first stage of printing, the 30 µm wide radial support dynamic struts, the axle contact, and gear teeth were printed with the more rigid tetra-thiol GCPU (Material 100-000-000) (Fig. 7B). The unpolymerized 100-000-000 prepolymer was rinsed away, and followed by printing of the second prepolymer, 050-000-050. The inner portions responsible for rotational dampening were printed with the more compressible and elastic mixture of tetra/di-thiol GCPU (Material 50-00-50) (Fig.6C). Material 50-00-50 provides elastomeric dampening, better distribution of force along the struts, and can prevent out-of-plane buckling. Thus, we demonstrate that modular formulations of GCPU can be combined synergistically for flexible applications.

Figure 4.7C shows a cantilever of gradient thickness with flexion points that allow preferential bending after the application of varying forces. This

design was envisioned as a valve for lab-on-a-chip (LOC) platforms examining variable pulsatile-flow in vascular indication models, and is designed to variably reduce the lag phase of fluid backflow during pulsatile flow. The two-step printing process used GCPU 100-000-000 and 050-000-050 for the rigid low compression backbone and stabilizing elastomeric regions, respectively. The varied regions of flexure reduce the valve closing time in situations where the flow rate may change, such as when experiencing system dilation, or the difference in cardiac output between infants and adults. GCPU's low cell adhesion properties may also provide an additional advantage in reducing biofouling.

Here, we used DOPsL to spatially localize GCPU material-dependent viscoelastic properties in a controlled platform. Combining DOPsL and the tunable properties of GCPU provides mechanical solutions to circumvent some existing issues in printing or attaching different materials.

4.5 CONCLUSION

We demonstrated a novel process to produce isocyanate-free PUs in a two-step synthesis consisting of a thermal ring opening reaction of functional cyclic carbonates with a diamine, and UV polymerization of the resulting diallyl diurethane prepolymer with thiol cross-linkers by click chemistry. Physical properties of GCPUs from different combinations of linear and branched thiols were characterized, and shown to be tunable, cytocompatible, and photo-printable via DOPsL, thus demonstrating the capability to spatially pattern different materials into novel, biocompatible structures.

The tunability and characteristics of printable GCPU materials can be enhanced by using other types of biogenic polyamines such as putrescine (C4-diamine), spermidine (tri-amine) and spermine (tetra-amine) instead of cadaverine (C5-diamine), to affect chain length and degree of cross-linking. Furthermore, the green chemistry involved in GCPU synthesis eliminates hazardous leechants such as phosgene, aromatic amines, and isocyanates, thus opening new pathways for PU cytocompatibility and its use in biomedical engineering.

4.6 ACKNOWLEDGEMENTS

The project described was supported in part by the Department of Defense (W81XWH-14-1-0522), California Institute for Regenerative Medicine (RT3-07899) and National Science Foundation (CMMI-1332681 and CMMI-1547005) to S.C. The work was also supported by VINNOVA (The Swedish Agency for Innovation System) and The Swedish Research Council Formas to S.-H.P. SEM, DMA, TMA, DSC, and FTIR equipment use and support was provided by UCSD Nanoengineering Materials Research Center.

Chapter 4, in full, is currently being prepared for submission for publication of the material. Warner, John; Gillies, Allison; Hwang, Henry H.; Zhang, Hong; Lieber, Richard L.; Chen, Shaochen, “Printed Biomaterials with Regional Auxetic Properties”. The dissertation author was the primary investigator and author of this material.

4.7 SUPPORTING INFORMATION

-(SI 4.8) GCPU Material 000-050-050 (3SH-2SH) Shape Reversion

-(SI 4.9) GCPU Stress-Strain Curves of Key Mixtures

-(SI 4.10) Cell Sheet on GCPU Slab Removed with Minimal Force

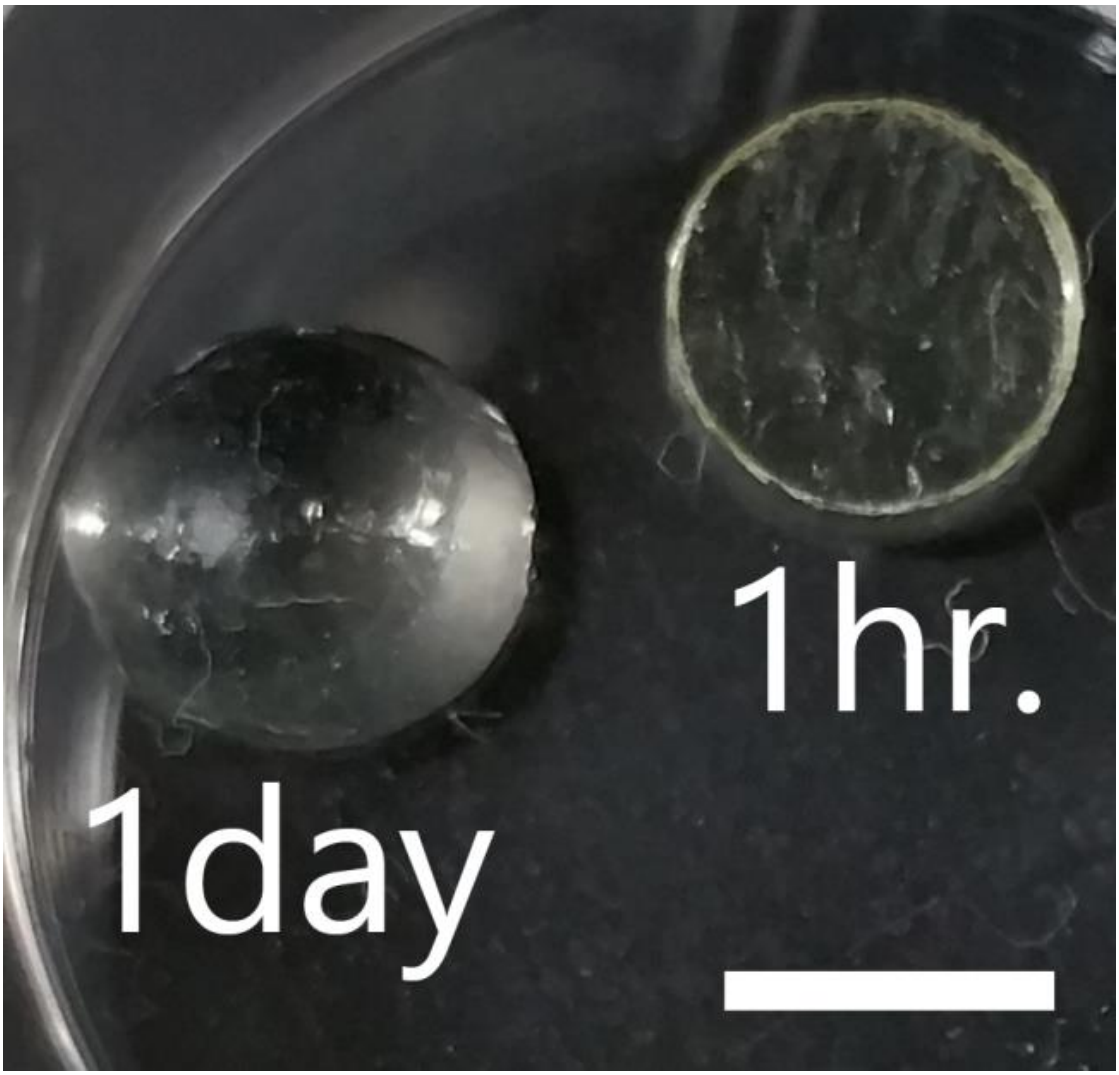

Figure 4.8: GCPU Material 000-050-050 (3SH-2SH) Shape Reversion: GCPU Material 000-050-050 (as per Table 1 in the manuscript) solidified after 5 minutes of UV exposure and was cut into 6 mm x 1 mm (D x H) disk, seen at one hour. After 1 day, the disk structure reverted to a drop-like dome appearance. This sample was not mechanically tested but illustrates a viscous liquid shape deformation over time. (Scale bar = 5mm)

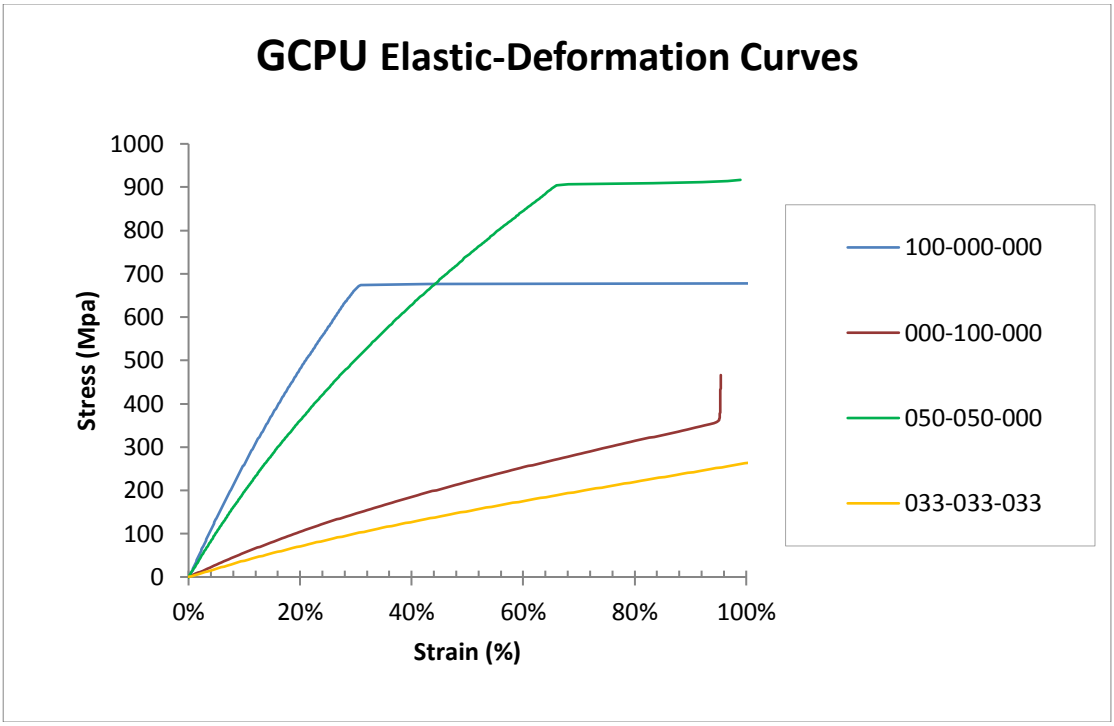

Figure 4.9: GCPU Stress-Strain Curves of Key Mixtures: Stress-strain curves of key GCPU mixtures based on Table 1. Data curves were used to determine Young's Modulus values for comparing GCPU material property variations (Figure 4.4). The curves are derived from probe force/displacement curves combined with measurements from the GCPU thin film samples.

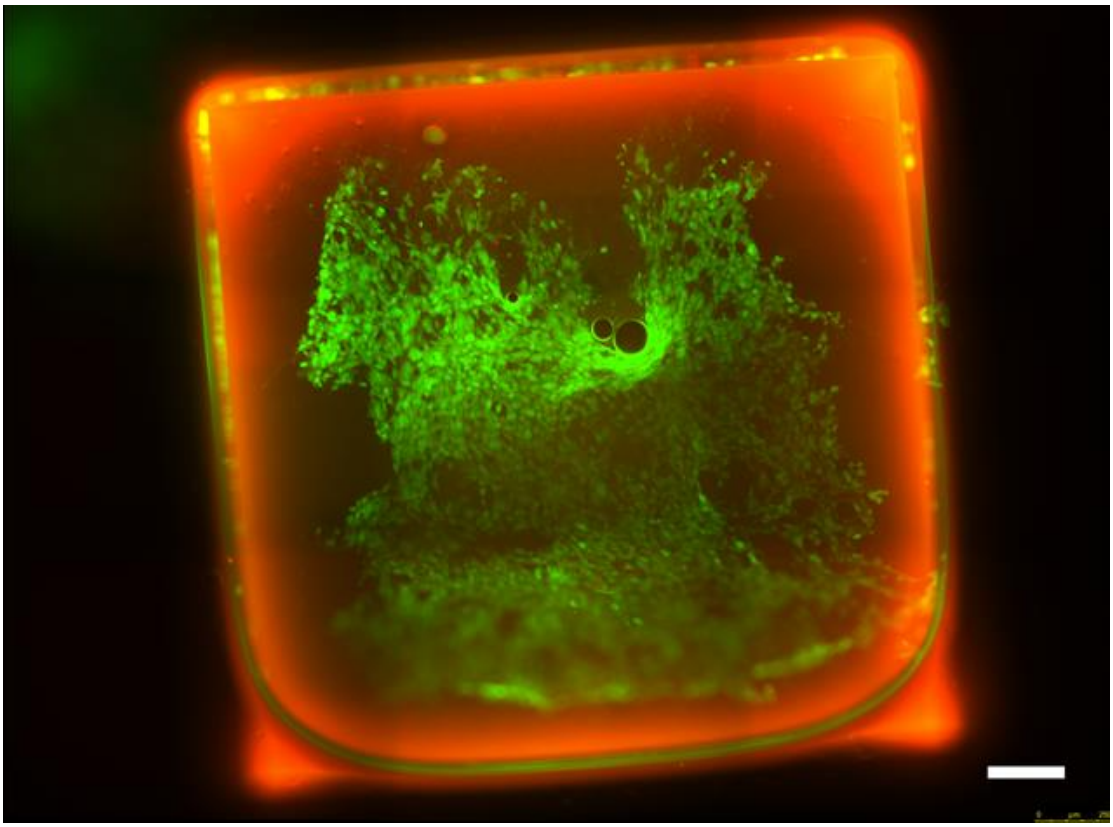

Figure 4.10: Uncoated GCPU Material 100-000-000 shows low cell adhesion via bubble displacement and cytocompatibility: Cell Live/Dead Assay: Murine 3T3 C2C12 mybloasts grown on GCPU for 5 days. Green = Calcein AM, Red = Ethidium Bromide. GCPU materials 100-000-000 were tested (uncoated). Structures were inverted for imaging. Image shows low cell adhesion and cytocompatibility. Bottom of image shows cell sheet falling toward viewer. Air bubbles displace the cell sheet. (Scale bar = 250 µm)

Chapter 5: Summary

Continuous projection stereolithography was shown to be capable of creating 3D printed biomaterial scaffolds for mammalian cells. Relying on the high resolution and flexibility of the DOPsL system, the transfer of complex designs into various photo-polymerizable materials was also achieved (Figure 2.3). This capability enabled the printing of scaffolds that mimic natural organizations of specific environments. As mentioned previously, some of these natural patterns are residual artifacts of optimized physical processes that have occurred in one medium and can then be transferred to various other media. These efforts of transferring force optimized patterns with the associated benefits of these material organizations may be useful to recapitulate nascent cell environments. This fabrication method was also implemented to create a dynamic multilayer auxetic mesh skeleton structure to convey similar counter-intuitive negative Poisson's ratio manipulations of force and movement to an outer hydrogel skin (Figure 3.5). Spatial patterning of biomaterials and localizing associated material properties were demonstrated over various polymers, including hydrogels and modular green-chemistry polyurethanes. The degree of pattern complexity in the above applications provides a useful tool for manipulating geometric cues in a manner consistent with the anticipated combination of both mechanical and biochemical stimuli for stem cell differentiation. It is our aim that this combination will enable future investigation of fundamental trends underlying cell organization, tissue models of tendon-muscle transition, and material choices for bio-scaffolds. If

these actions are successful, the ability to grow differentiated tissue on an artificial scaffold with information acquired from deconstructing natural tissue may provide a realistic and sustainable solution for future artificial organ generation. Synthetic methods other than xenogenic or allogenic harvesting of ECM may facilitate personalized medicine with an alternate resolution that is possibly less costly and raises fewer ethical concerns.

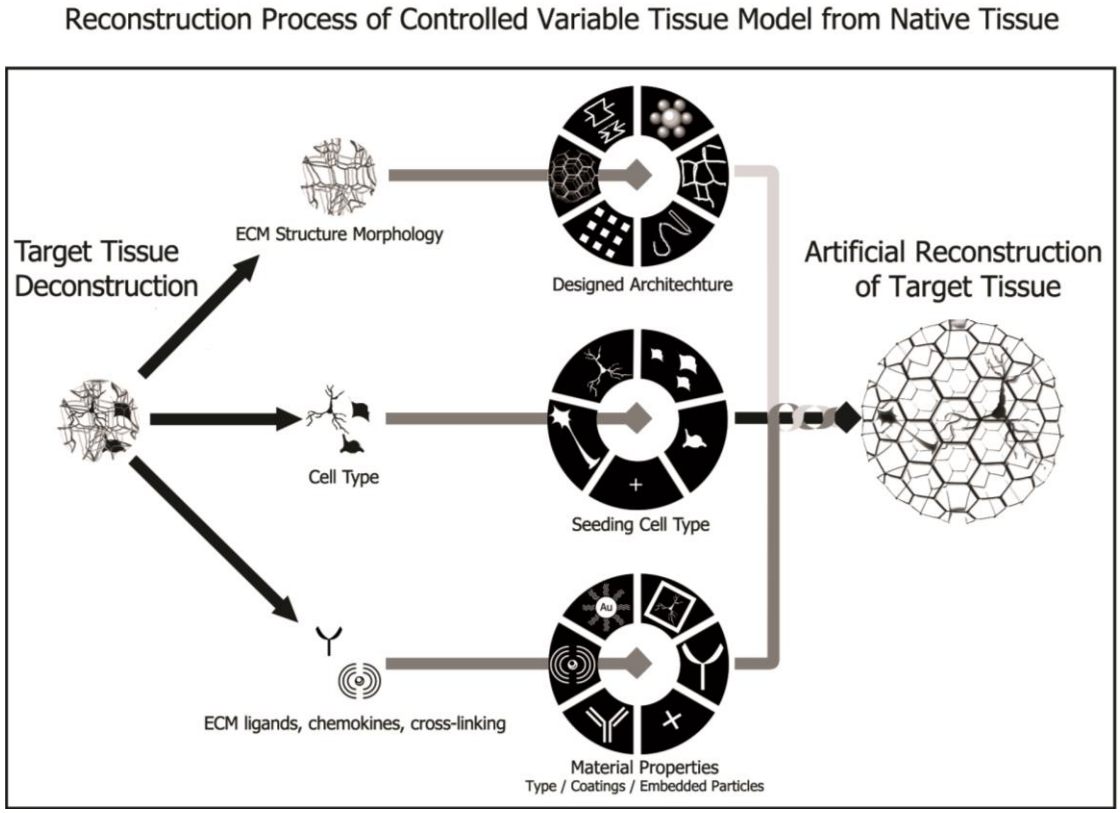

Figure 5.1: Reconstruction process of controlled viable tissue model from native tissue - concept. LEFT: Deconstruction of natural target tissue. MID: Advancement possibility of each individual technology. RIGHT: Reassembly of individual components into synthetic tissue construct.

Indirectly supporting this future path, printing methods are moving towards reversible polymers which enable write-erase functionality and post-polymerization modification to create much more complex, tunable and responsive structures. These added polymer-based functions will also permit various material life-cycle phases, each with the potential for unique applications that are based on scaffold construction. Additionally, in efforts to mimic the naturally occurring extra cellular matrix, these materials often use protein or polysaccharide components and have the flexibility for surface modification to express protein receptors, signaling molecules, or adhesive peptide motifs as illustrated in Figure 5.1. Deforest and Tirrell even demonstrated a complex chemically-engineered answer to “reversible” patterning by individually addressing each of these concepts with a different chemical reaction[122]. Their multi-step chemistry approach uses azide-alkyne cyclo-addition to form the initial polymer network, photo-deprotection to open sites for protein addition, and o-nitrobenzyl ester linker photo-cleavage for removal of the newly added surface protein. This technique was clever and well executed when approaching the problem as individual challenges in a step-wise fashion. Despite this technique providing a legitimately useful ability to remove a newly added protein, a residual chemistry persists and appears only capable of one reversal iteration. This method presents a reversble outcome, but not a truly reversible chemistry capable of unlimited “erasing.” The distinction lies in restoring the original state of the material, thus enabling unlimited reversibility. The application of “unlimited” reversibility is not new, as

liquid chromatography has utilized charge manipulation via pH and salt charge screening for decades to separate materials (*e.g.* ion exchange, hydrophobic interaction, affinity, and reverse-phase chromotographies) with truly reversible binding. The difference with Deforest's and Tirrell's work is using covalent bonds and photochemistry. One limitation plaguing covalent addition and cleaving chemical reactions, are that these reactions are fundamentally limited to one site for one type of reaction when trying to maintain specificity. The advantage is a very strong bond. In contrast, nature uses a strategy of common building blocks, such as amino acids and nucleic acids to generate virtually unlimited permutations of binding sites connecting with weaker bonds. Complementary DNA strands use simple hydrogen bonding controlled by steric hindrance (shape fit) from planar nucleic acids and generate specificity from sequential serial combinations (a similar theme to ligand-receptor specificity in proteins that inspired affinity chromatography). In this case, a natural polymer, *i.e.* DNA, is used to define or encode a proximity of individual site interactions and is capable of unlimited reversible thermal binding while additionally capable of limited reversible binding via localized incident light[123–128]. As an adjunct, this specific hydrogen bonding motif has already been implemented in synthetic polymers to demonstrate more immediate reversible bonding from mechanical cleavage in some self-healing polymers[129–131].

Another future technology concern involves scalability and resolution; which are normally at odds, and susceptible to varying degrees of compromise

depending on the application. Normally, as resolution improves, setup costs associated with operating a parallel system increase proportionally to size, with the additional complexity of the system communicating in concert (registration, alignment) to create a consistent final re-printable structure. The conventional engineering, equipment-based, top-down manufacturing perspective tends to focus on initial capital equipment and less on innovation of consumable polymers capable of self-assembly and light directed spatial localization. However, these two characteristics have the potential to achieve high resolution with increased scalability. Additionally, if selective reversible printing is applied effectively to a self-assembly system, then some of the existing known shortcomings of self-assembly, such as long-range defects, become less detrimental to implementation. Such controlled self-assembly has been seen with DNA origami in addition to prion (HET-s) fibrils and would benefit future fabrication methods[132,133].

Briefly addressing the general concern of polymer chemical coatings, the tunable specificity of DNA enables short nucleotide strand labeling that is often implemented in the probe design associated with mass produced and robust quantitative polymerase chain-reaction (QPCR) chemistries. As such, DNA chemistry has an extensive established history of covalent conjugation with synthetic chemistries to many material substrates as a surface coating (amino-silanized glass, dendrimer nuclei e.g.) and to other moieties (dyes, proteins, lipids) that function as labels, tethers, or transmission agents. As

such, the chemistry for DNA attachment already exists and is well documented. These characteristics point to DNA or perhaps a modified variant polymer incorporating these general DNA properties as future means to improve biomaterial printing.

With the perspective that DNA exhibits many characteristics desired in future high resolution, self-assembling, sequence editable, photo-responsive polymers capable of surface molecule addition while possessing an inherent photo-chemistry involving thymine dimers, we looked at using simple DNA as a reversible photopolymer. Heller's group in 2016 showed a double write system for DNA that was able to print layers using thymine dimerization to interfere with oligonucleotide annealing[134]. Using this concept, we used DOPsL to pattern thymine-dimerization on the Heller group's single stranded thymine 24-mer DNA [T(24)ssDNA] coated glass substrate. As expected, we show patterned dimerization with DOPsL in Figure 5.2 and thus demonstrate the feasibility of DNA layer printing on DOPsL with the Heller group's concept. Similar chemistries like cinnamate incorporation into the oligonucleotide have been utilized to lock a binding state, as being permanently bound or unbound. Despite, not being reversible, cinnamate-DNA photochemistry is covalent, demonstrating another method capable of use in DNA photolithography that further supports the flexibility of DNA as a photopolymer[135]. To make this polymer chemistry truly reversible, a multi-repeatable-reversible step is required. To clarify, this contrasts many chemistries that merely utilize

cleavage reactions, which provide an irreversible step that reverses a previous action, only once [122,136].

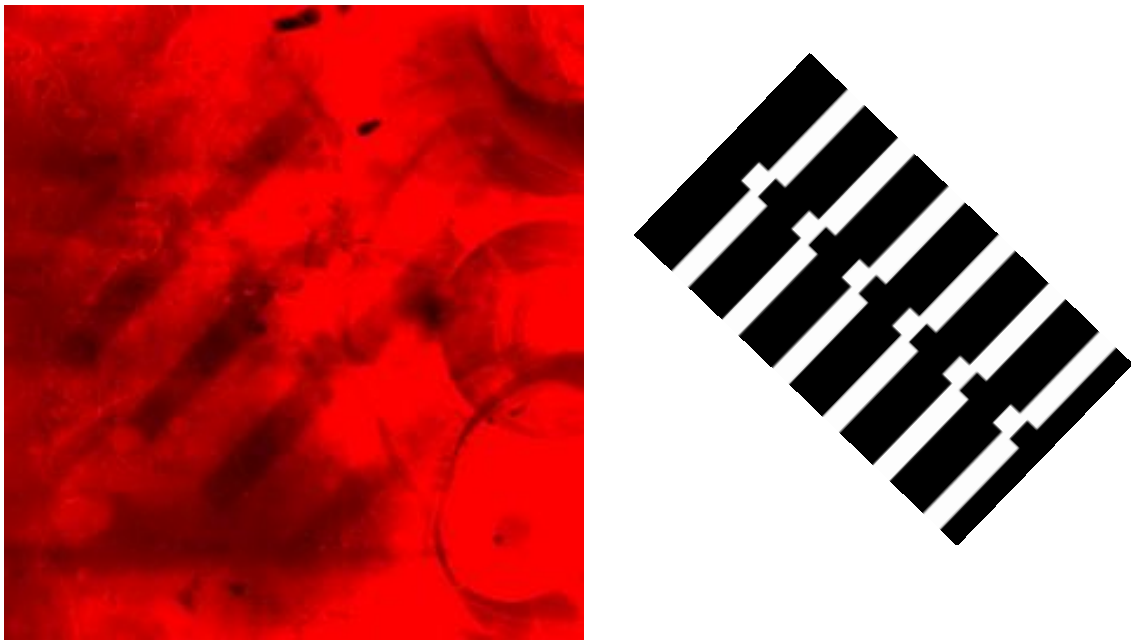

Figure 5.2: Fluorescent microscope image (LEFT) of amino-silanized glass reacted with bis (sulfosuccinimidyl) suberate (BSS) and 5"amino-linked thymine 24-mer ssDNA oligo-nucleotides, after exposure to an unfiltered high-energy light spectrum of ~250nm-500nm from a halogen bulb (Omincure S2000) for 15 minutes (of summed serial exposure) in a DOPsL projected pattern. Hybridization with Cy3 labeled adenosine 24-mer ssDNA oligonucleotides reveals binding interference in the area of the projected light pattern. Digital pattern loaded to DOPsL (RIGHT). White pixels represent micromirror activation to project light to sample stage.

Fortunately for this proposed DNA concept, thymine dimers can be reversed with specific enzymes. Despite mammalian error-checking system pathways where thymine dimers (T<>T) are excised and replaced using the complementary DNA strand as a template, bacteria can reverse T<>T with specific enzymes in combination with an energy storage molecule and lower energy light[137]. While trying to understand ways to combat the effects of photo-induced DNA damage from a worsening ozone-depleted solar light

spectrum, Sancar 2001 shows in multiple works the efficiency of particular isolated bacterial cryptochromes to reverse various T<>T products when exposed to 366nm blue light (as part of bacterial photo-reactivation). Some of these cryptochromes were photolyases from *Vibrio cholerae* that were specific to reversing cyclobutyl-pyrimidine (CPD) thymine dimer products[128]. While other proteins are responsible for other, and sometimes multiple, dimer products, the protein isolated from UNC-2001 plasmid appears to be the most efficient and specific to CPD products. The CPD product was selected as the most promising T<>T for this DNA polymer application for a few reasons. CPD's are less likely to confer retained biological gene mutations than 6-4 dimer products under some circumstances suggesting that CPD are more available for enzymatic binding or more deviant from normal DNA and thus biologically more "noticeable," for cleavage and removal than other dimer products. Intuitively this follows as the strained butyl ring of the CPD structure possesses a higher steric hindrance, and more greatly perturbs the DNA sugar-phosphate backbone, which impedes complementary strand binding.

As Sancar's isolated photolyase from *V. cholerae* was capable of dark reaction binding and a strong potential catalyst for nearly unlimited reversible binding of DNA T<>T CPD products, we chose to examine DOPsL for implementation in the capacity to spatially localize different spectrums of light for DNA photo-chemistry. Designed single-strand ssDNA fragments purchased from IDT (Integrated DNA Technologies) were exposed to the full spectrum

irradiation from the DOPsL light source in tris-EDTA buffer (1x). The samples were mixed with the respective complementary DNA strand and run as a high resolution melt curve (HRM) via a quantitative polymerase chain reaction instrument (QPCR- IlLumina Eco). This assay uses the change in light intensity from a double strand dsDNA inter-collating SYBR dye to infer the annealing temperature, and thus indicate a change in binding affinity between strands caused by T<>T's. The complement DNA fragment with one thymine pair annealed at 58°C as a negative control. Exposure of the DNA strands of this fragment to full spectrum (~250 nm – 600 nm) light prior to mixing, yielded multiple broad products peaks annealing at 55°C and 60°C. These results noticeably differ from the results of the positive control designed to emulate binding-inhibition of the thymine dimerization, which show a single narrow peak melting 49°C, as seen in supporting information Figure SI 5.5.

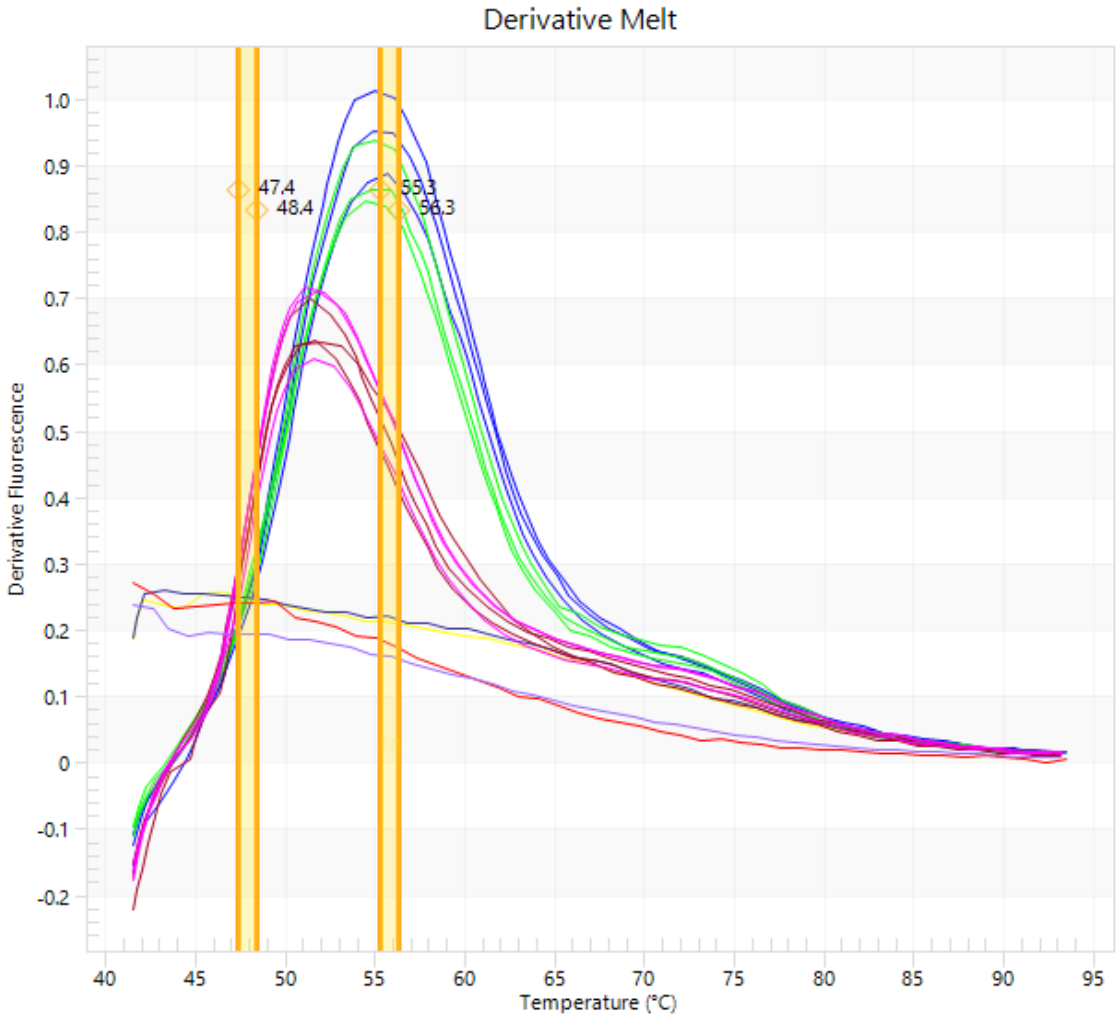

Figure 5.3: Derivative melt curve of ssDNA oligonucleotides individually exposed to 313 nm light. (oli1+oli2 individually exposed to UV for 0,5,10,15 min / Blue, Green, Pink, Maroon); (oli3 only UV for 0,15 min / Yellow, Gray); (Red = oli 1 only UV min); (Lavender = oli 2+ oli 3 UV 0min); 5'-3' Oligonucleotide 1:GCA GTA CGT TAG TGA CAC G / Oligo 2-CGT GTC ACT AAC GTA CTG C / Oligo 3-CGT GTC ACT GCC GTA CTG C. Oligos 2 and 3 compliment oligo 1 except at underlined regions. Evagreen dye (1x) used without polymerase at 10 µL reaction volume. ssDNA quantity constant between samples at 1 µg/well.

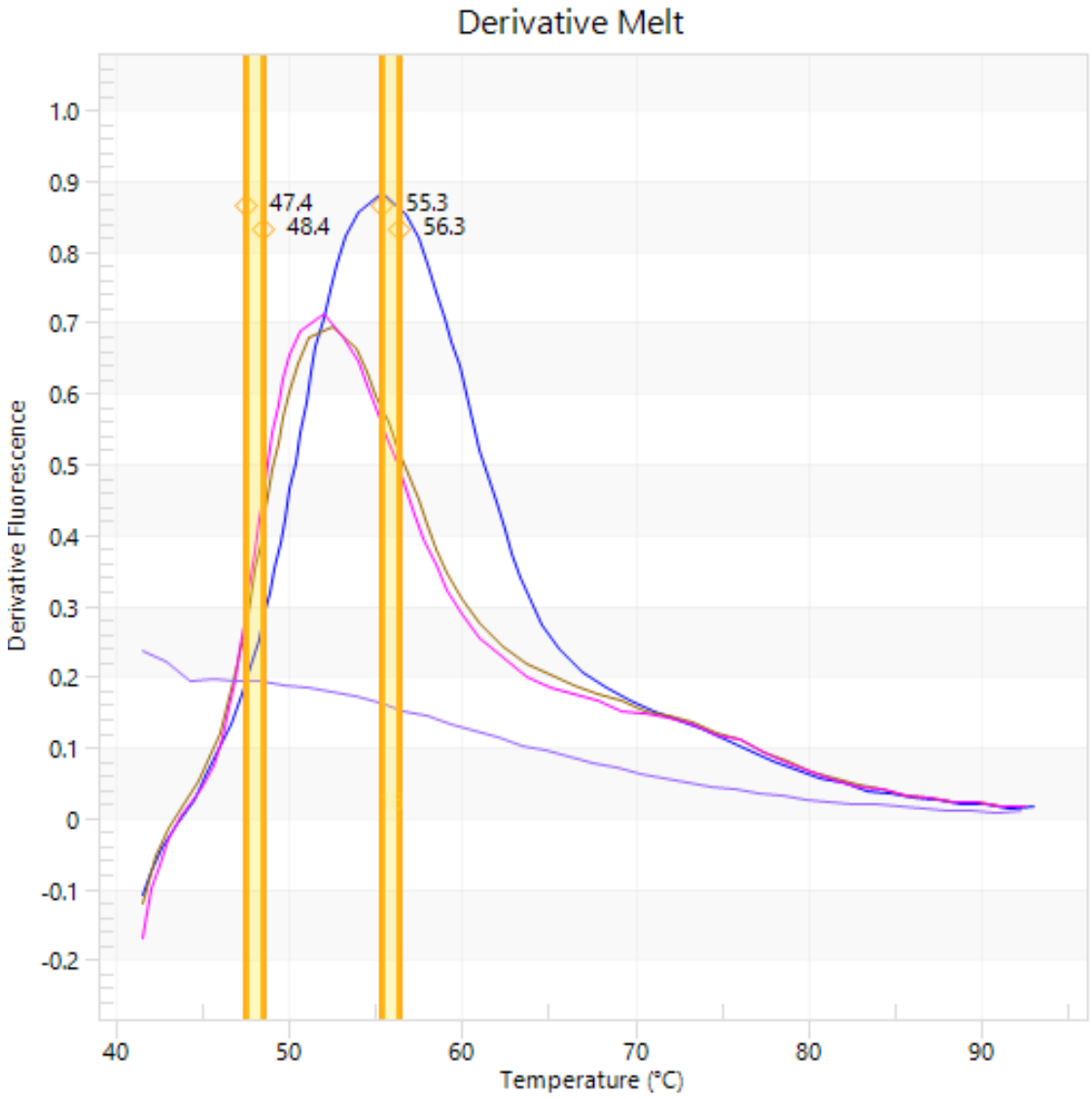

Figure 5.4: Derivative melt curve to identify action at 313nm on a single strand: Blue = oli1+oli2 0 min 313nm, pink = oli1+oli2 exposed to 313nm 15 min / maroon = oli1+oli2 and only primer 2 exposed to 313nm 15 min / lavender = oli1+oli3 0 min 313 nm. 5'-3' Oligonucleotide 1:GCA GTA CGT TAG TGA CAC G / Oligo 2-CGT GTC ACT AAC GTA CTG C / Oligo 3-CGT GTC ACT GCC GTA CTG C. Oligos 2 and 3 compliment oligo 1 except at underlined regions. Evagreen dye (1x) used without polymerase at 10 µL reaction volume.

This approximation of a positive CPD experimental control was designed as a dual sequential nucleotide mismatch at the thymine dimer site with the same complementary strand. As expected, this control only focuses on hydrogen binding interference at the effective location, while excluding

some critical aspects; axial nucleotide alignment caused by the cyclo-butyl ring of CPD, which disrupts the sugar-phosphate backbone, and any partial hydrogen bonding by the nucleotide bases tilted to accommodate formation of the cyclo-butyl ring. Despite these differences, the experimental sample should more closely match the positive control and not reveal multiple peaks. Though HRM derivative peaks are dependent on the concentration of species in solution, concentration changes of 10 fold at the tested concentration in buffer, yields a derivative peak with less than one degree of difference (Figure SI 5.6). The culmination of this evidence suggested that an unfiltered spectrum was insufficient to produce a useable photoproduct for reversible DNA photochemistry. Influenced by Matsunaga 1991[123], 313 nm light was chosen to transform the ssDNA containing the thymine dimer pair to reveal a single narrower-peak product annealing 5°C cooler from the negative control which indicated weaker binding affinity to the complement strand and thought to be caused by T<>T disruption (Figure 5.3). This 5°C value is closer to the 2.3˚C / nucleotide approximation from the IDT algorithm (2.3˚C x 2 bases = 4.6˚C) and indicates a hydrogen-bonding disruption similar to the experimental positive control. DNA strands not containing a sequential thymine pair do not appear to have binding affected by 313 nm radiation during the 15 minutes exposure time with the filtered halogen lamp source as seen in Figure 5.4, where ssDNA containing the 313 nm irradiated thymine pair was mixed with the non-irradiated complementary DNA strand to yield a similar melting product as found in Figure 5.3. Based on this work, DOPsL is capable of

transforming normal DNA with sequential thymine nucleotides into a single “non-binding” state thermal product, while not affecting non-sequential thymine pairs and demonstrating programmed specificity. Based on Matsunga’s work, this “non-binding” thermal product should be capable of numerous reversible cycles via Sancar’s *V. cholerae* photolyase (VcPhr). VcPhr may provide true reversibility for DNA or a DNA analogue polymer that has never been seen before in 3D fabrication.

Personalized medicine also would benefit from inexpensive receptor fabrication. Conventional means of procuring protein receptors for efficacy assays, such as ELISA (enzyme linked immune-sorbent assays) involve animal harvesting or transgenic host cells [*e.g.* E. coli, Chinese hamster ovary (CHO), or insect lines]. Both means are moderately expensive and can be complicated by host post-translational modification (*e.g.* glycosylation). However, nucleic acid aptamers might provide a possible answer. Originating from a natural biological mechanism of folded mRNA which interacts with riboswitches for epigenomic regulation, increasingly more synthetic aptamer variants have been used to bind other protein receptors. Even DNA has been used to form suitable shape and charge permutations to function in receptor binding. Aptamers are a strong candidate for future involvement in receptors for biosensors, substrate ligands for lab-on-chip devices, and regenerative medicine to up-regulate genes in natural or artificial tissue. This permutation based iterative selection process has already shown use in devices and

sensors with thrombin interaction normally involved in clotting[138–140]. Given the sequence tunable nature of DNA aptamers, combination with photo-induced T<>T binding interference has legitimate potential to create a truly reversible ligands that can be designed to fit virtually any receptor site via SERRS screening[141]. By inserting or substituting a single thymine nucleotide next to an existing thymine within a non-loop, bound aptamer region and adding a complementary adenine in the corresponding structure arm of the aptamer, the aptamer can be tuned to destabilize that region with exposure to 313 nm light. Repeated in multiple regions, the aptamer can theoretically be designed to completely unfold and refold, thus unbinding and binding multiple times with 313 nm light, the photolyase from *V. cholerae* (VcPhr), 366 nm light required for VcPhr reversal and possibly $FADH_2$.

Though limitations of DNA as a future polymer for 3D fabrication of biomaterial scaffolds do exist, most notably the issue of non-covalent annealing, these hydrogen bond limitations are also responsible for many exceptional material properties found in extremely elastic alginate and even self-healing polymers. Additionally, these limitations can be remedied with the existing DNA chemistries, such as using incorporated cinnamate photo-crosslinking. Regardless, the immense advantage of nucleotide permutation determined specificity to target material coatings with the existing chemistry library of DNA conjugations can be leveraged toward a DNA polymer or a synthetic DNA polymer analogue. Combining these existing properties with

self assembly, sequence defined photo-reversible binding, and receptors capable of switchable on/off designs in the form of aptamers, makes the potential of DNA as a bio-scaffold polymer or similar material undeniable. This is where the future of synthetic regenerative personal medicine lies, in a concerted effort to fabricate complex 3D organs without reliance on animal harvesting.

5.1 SUPPORTING INFORMATION

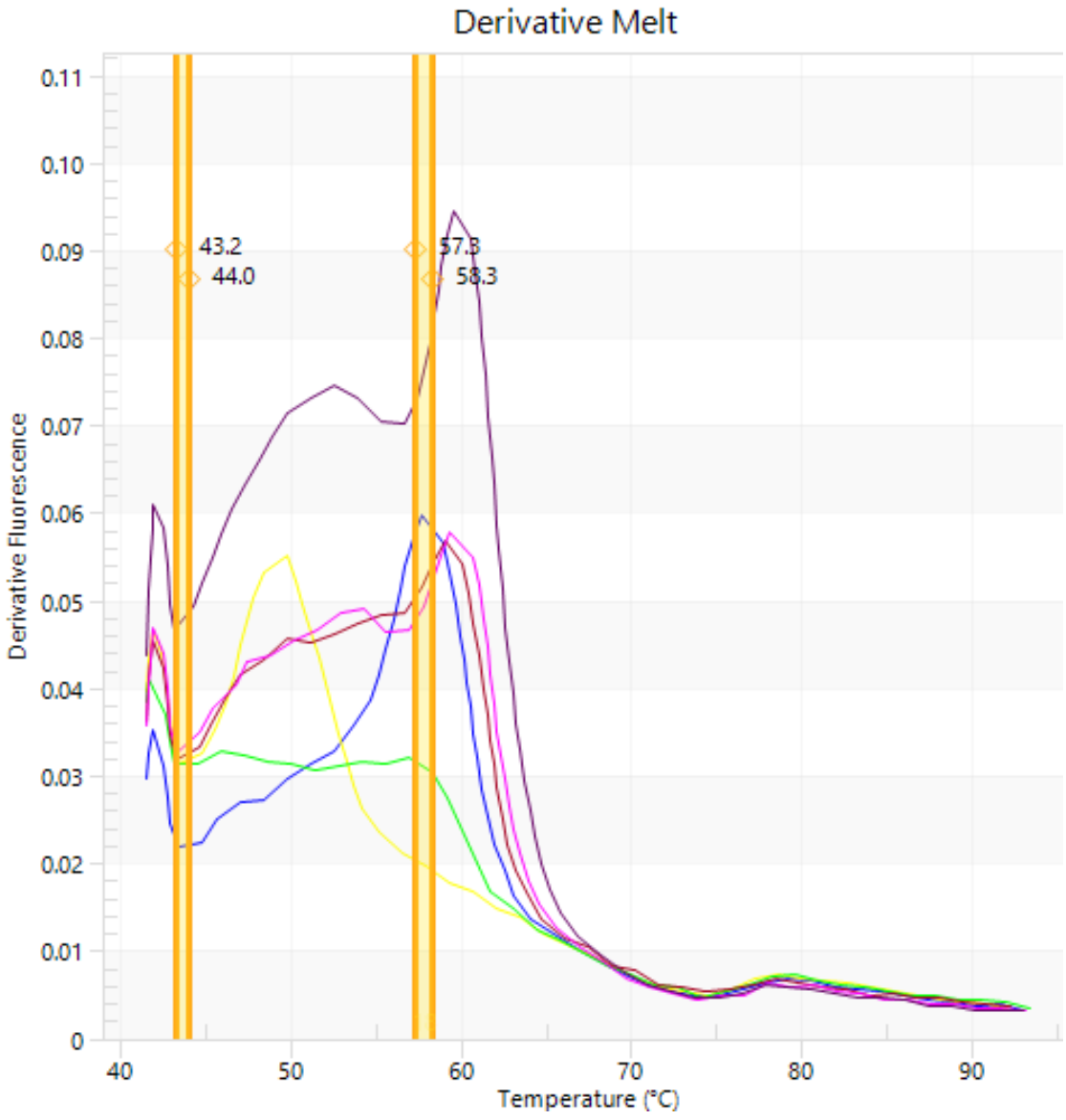

Figure 5.5: Derivative melt curve of mixed ssDNA exposed to ~250nm-600nm, unfiltered light from halogen source. Blue = oli1+oli2 with 0 minutes of UV light exposure; Green = oli1+oli2 with UV 5 min; Maroon = oli1+oli2 with UV 10 min; Pink = oli1+oli2 with UV 15 min; Yellow = oli1+oli3 with UV 0 min; Purple = oli1+oli3 with UV 15 min; Oligonucleotide 1-GCA GTA CGT TAG TGA CAC G / Oligo 2-CGT GTC ACT AAC GTA CTG C / Oligo 3-CGT GTC ACT GCC GTA CTG C. Primer 2 and 3 compliment primer 1 except at underlined regions. Evagreen dye (1x) used without polymerase at 10 µL reaction volume. ssDNA quantity constant between samples at 0.5 ng. Expected annealing temperature of intended product is between 50°C (yellow) and 58°C (blue). Annealing present after 10 min of UV, however is not expected to persist in oli1+oli3 combination with UV. Annealing product at 59°C suggests unexpected photochemistry.

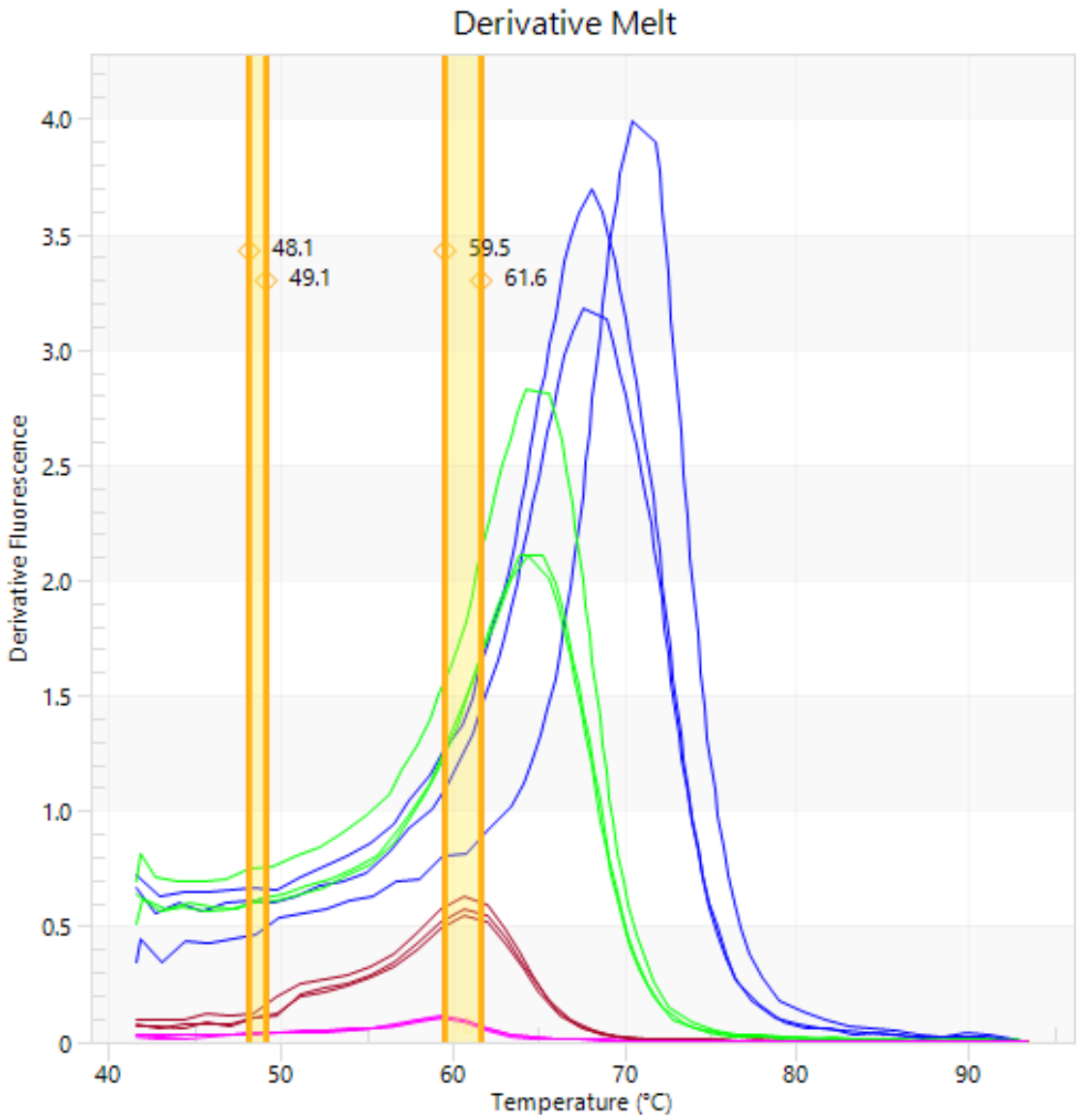

Figure 5.6: Derivative melt curve of complementary ssDNA (oli1 + oli2) at various concentrations 250 µg / 25 µg / 2.5 µg /0.25 µg per 10 µL well. (Blue/Green/Maroon/Pink). **;** Oligonucleotide 1-GCA GTA CGT TAG TGA CAC G / Oligo 2-CGT GTC ACT AAC GTA CTG C. Primer 2 compliments primer 1 except at underlined regions. Evagreen dye (1x) used without polymerase at 10 µL reaction volume. No UV light.

References:

1. Chen Q, Liang S, Thouas GA. Elastomeric biomaterials for tissue engineering. *Prog Polym Sci*. 2013;38(3-4):584-671. doi:10.1016/j.progpolymsci.2012.05.003.

2. Vanderhooft JL, Alcoutlabi M, Magda JJ, Prestwich GD. Rheological properties of cross-linked hyaluronan-gelatin hydrogels for tissue engineering. *Macromol Biosci*. 2009;9(1):20-28. doi:10.1002/mabi.200800141.

3. Young JL, Engler AJ. Hydrogels with time-dependent material properties enhance cardiomyocyte differentiation in vitro. *Biomaterials*. 2011;32(4):1002-1009. doi:10.1016/j.biomaterials.2010.10.020.

4. Ramón-Azcón J, Ahadian S, Obregón R, Camci-Unal G, Ostrovidov S, Hosseini V, Kaji H, Ino K, Shiku H, Khademhosseini A, Matsue T. Gelatin methacrylate as a promising hydrogel for 3D microscale organization and proliferation of dielectrophoretically patterned cells. *Lab Chip*. 2012;12(16):2959. doi:10.1039/c2lc40213k.

5. Yahia LH, Chirani N, Gritsch L, Motta FL, Natta CG. History and Applications of Hydrogels. *iMedPub Journals*. 2015;4(2:13):1-23.

6. Fo HOS, Novaes AB, De Castro LMS, Rosa AL, De Oliveira PT. In vitro osteogenesis on a microstructured titanium surface with additional submicron-scale topography. *Clin Oral Implants Res*. 2007;18(3):333-344. doi:10.1111/j.1600-0501.2006.01313.x.

7. Meyer W, Engelhardt S, Novosel E, Elling B, Wegener M, Krüger H. Soft Polymers for Building up Small and Smallest Blood Supplying Systems by Stereolithography. *J Funct Biomater*. 2012;3(4):257-268. doi:10.3390/jfb3020257.

8. Fang NT, Xie SZ, Wang SM, Gao HY, Wu CG, Pan LF. Construction of tissue-engineered heart valves by using decellularized scaffolds and endothelial progenitor cells. *Chin Med J (Engl)*. 2007;120(8):696-702. doi:10.3111/13696998.2012.709204.

9. Butcher JT, Penrod AM, García AJ, Nerem RM. Unique Morphology and Focal Adhesion Development of Valvular Endothelial Cells in Static and Fluid Flow Environments. *Arterioscler Thromb Vasc Biol*. 2004;24(8).

10. Robinson R. Link between Cell Junctions and Microtubule Cytoskeleton Is Critical for Epithelial Morphogenesis. *PLOS Biol*. 2015;13(3):e1002088. doi:10.1371/journal.pbio.1002088.

11. Liu Z, Tan JL, Cohen DM, Yang MT, Sniadecki NJ, Ruiz SA, Nelson CM, Chen CS. Mechanical tugging force regulates the size of cell-cell junctions. *Proc Natl Acad Sci U S A*. 2010;107(22):9944-9949. doi:10.1073/pnas.0914547107.

12. Zhang CAP, Qu X, Soman P, Hribar KC, Lee JW, Chen S, He S. Rapid Fabrication of Complex 3D Extracellular Microenvironments by Dynamic Optical Projection Stereolithography. *Adv Mater*. 2012;(24):4266-4270. doi:10.1002/adma.201202024.

13. Hribar KC, Soman P, Warner J, Chung P, Chen S, Chin CD, Linder V, Sia SK, Ghaemmaghami AM, Hancock MJ, Harrington H, Kaji H, Khademhosseini A, Ingber DE, Whitesides GM, Baker M, … Gu M. Light-assisted direct-write of 3D functional biomaterials. *Lab Chip*. 2014;14(2):268-275. doi:10.1039/C3LC50634G.

14. Takahashi H, Hasegawa S, Takita A, Hayasaki Y. Sparse-exposure technique in holographic two-photon polymerization. *Opt Express, Vol 16, Issue 21, pp 16592-16599*. 2008;16(21):16592-16599. doi:10.1364/OE.16.016592.

15. Zhou J, Niklason LE. Microfluidic artificial “vessels” for dynamic mechanical stimulation of mesenchymal stem cells. *Integr Biol*. 2012;4(12):1487-1497. doi:10.1039/C2IB00171C.

16. Falconer K. *Fractal Geometry Mathematical Foundations and Applications*. Vol 46.; 1990. doi:10.2307/2532125.

17. Mandelbrot BB. The Fractal Geometry of Nature. *Am J Phys*. 1983;51(3):286. doi:10.1119/1.13295.

18. Yasar O, Lan S-F, Starly B. A Lindenmayer system-based approach for the design of nutrient delivery networks in tissue constructs. *Biofabrication BIOFABRICATION Biofabrication*. 2009;1(1):45004-45009. doi:10.1088/1758-5082/1/4/045004.

19. Bennett SH, Bennett SH, Eldridge MW, Eldridge MW, Puente CE, Puente CE, Riedi RH, Riedi RH, Nelson TR, Nelson TR, Beotzman B, Beotzman B, Milstein J, Milstein J, Singhal SS, Singhal SS, … Woldenberg MJ. Origin of fractal branching complexity in the lung. *Preprint*. 2000. http://scholar.google.com/scholar?hl=en&btnG=Search&q=intitle:Origin+of+fractal+branching+complexity+in+the+lung#0. Accessed March 8, 2016.

20. Nelson TR, West BJ, Goldberger AL. The fractal lung: universal and species-related scaling patterns. *Experientia*. 1990;46(3):251-254. doi:10.1007/BF01951755.

21. Alt W, Adler F, Chaplain M, Deutsch A, Dress A, Krakauer D, Tranquillo RT, Losa G a., Merlini D, Nonnenmacher TF, Weibel ER, Hou C, Gheorghiu S, Coppens M-O, Huxley VH, Pfeifer P. *Fractals in Biology and Medicine*. (Losa GA, Merlini D, Nonnenmacher TF, Weibel ER, eds.). Basel: Birkhäuser Basel; 2005. doi:10.1007/3-7643-7412-8.

22. Vozzi G, Previti A, Ciaravella G, Ahluwalia A. Microfabricated fractal branching networks. *J Biomed Mater Res - Part A*. 2004;71(2):326-333. doi:10.1002/jbm.a.30167.

23. Sun W, Darling A, Starly B, Nam J. Computer-aided tissue engineering: overview, scope and challenges. *Biotechnol Appl Biochem*. 2004;39(Pt 1):29-47. doi:10.1042/BA20030108.

24. Cheung N, Donaghue KC, Liew G, Rogers SL, Wang JJ, Lim SW, Jenkins AJ, Hsu W, Lee ML, Wong TY. Quantitative Assessment of Early Diabetic Retinopathy Using Fractal Analysis. *Diabetes Care*. 2009;32(1):106-110. doi:10.2337/dc08-1233.

25. Karperien A, Jelinek HF, Leandro JJG, Soares JVB, Cesar RM, Luckie A. Automated detection of proliferative retinopathy in clinical practice. *Clin Ophthalmol*. 2008;2(1):109. doi:10.2147/OPTH.S1579.

26. Masters BR. Fractal analysis of the vascular tree in the human retina. *Annu Rev Biomed Eng*. 2004;6:427-452. doi:10.1146/annurev.bioeng.6.040803.140100.

27. Hayashi T, Carthew RW. Surface mechanics mediate pattern formation in the developing retina. *Nature*. 2004;431(7009):647-652. doi:10.1038/nature02952.

28. Prusinkiewics P, Lindenmayer A, Hanan J, Fracchia F, Fowler D, de Boer M, Mercer L. The Algorithmic Beauty of Plants. *PhD Propos*. 1996;1. doi:10.1017/CBO9781107415324.004.

29. Vogel H. A better way to construct the sunflower head. *Math Biosci*. 1979;44(3):179-189. doi:10.1016/0025-5564(79)90080-4.

30. Unadkat H V, Hulsman M, Cornelissen K, Papenburg BJ, Truckenmüller RK, Carpenter AE, Wessling M, Post GF, Uetz M, Reinders MJT, Stamatialis D, van Blitterswijk CA, de Boer J. An algorithm-based topographical biomaterials library to instruct cell fate. *Proc Natl Acad Sci U S A*. 2011;108(40):16565-16570. doi:10.1073/pnas.1109861108.

31. Kumar G, Waters MS, Farooque TM, Young MF, Simon CG. Freeform fabricated scaffolds with roughened struts that enhance both stem cell proliferation and differentiation by controlling cell shape. *Biomaterials*. 2012;33(16):4022-4030. doi:10.1016/j.biomaterials.2012.02.048.

32. Eden M. A two-dimensional growth process. *Berkeley Symp Math Stat Probab*. 1961;4:223-239.

33. Ben-Jacob E, Schochet O, Tenenbaum a, Cohen I, Czirók a, Vicsek T. Generic modelling of cooperative growth patterns in bacterial colonies. *Nature*. 1994;368(6466):46-49. doi:10.1038/368046a0.

34. O'Brien FJ, Harley BA, Yannas I V., Gibson L. Influence of freezing rate on pore structure in freeze-dried collagen-GAG scaffolds. *Biomaterials*. 2004;25(6):1077-1086. doi:10.1016/S0142-9612(03)00630-6.

35. Billiet T, Vandenhaute M, Schelfhout J, Van Vlierberghe S, Dubruel P. A review of trends and limitations in hydrogel-rapid prototyping for tissue engineering. *Biomaterials*. 2012;33(26):6020-6041. doi:10.1016/j.biomaterials.2012.04.050.

36. Lee SB, Kim YH, Chong MS, Hong SH, Lee YM. Study of gelatin-containing artificial skin V: Fabrication of gelatin scaffolds using a salt-leaching method. *Biomaterials*. 2005;26(14):1961-1968. doi:10.1016/j.biomaterials.2004.06.032.

37. Moroni L, De Wijn JR, Van Blitterswijk CA. 3D fiber-deposited scaffolds for tissue engineering: Influence of pores geometry and architecture on dynamic mechanical properties. *Biomaterials*. 2006;27(7):974-985. doi:10.1016/j.biomaterials.2005.07.023.

38. Zong X, Bien H, Chung CY, Yin L, Fang D, Hsiao BS, Chu B, Entcheva E. Electrospun fine-textured scaffolds for heart tissue constructs. *Biomaterials*. 2005;26(26):5330-5338. doi:10.1016/j.biomaterials.2005.01.052.

39. Altomare L, Gadegaard N, Visai L, Tanzi MC, Farè S. Biodegradable microgrooved polymeric surfaces obtained by photolithography for skeletal muscle cell orientation and myotube development. *Acta Biomater*. 2010;6(6):1948-1957. doi:10.1016/j.actbio.2009.12.040.

40. Deligkaris K, Tadele TS, Olthuis W, van den Berg A. Hydrogel-based devices for biomedical applications. *Sensors Actuators, B Chem*. 2010;147(2):765-774. doi:10.1016/j.snb.2010.03.083.

41. Liska R, Schuster M, Inführ R, Turecek C, Fritscher C, Seidl B, Schmidt V, Kuna L, Haase A, Varga F, Lichtenegger H, Stampfl J. Photopolymers for rapid prototyping. *J Coatings Technol Res*. 2007;4(4):505-510. doi:10.1007/s11998-007-9059-3.

42. Melchels FPW, Feijen J, Grijpma DW. A review on stereolithography and its applications in biomedical engineering. *Biomaterials*. 2010;31(24):6121-6130. doi:10.1016/j.biomaterials.2010.04.050.

43. Landers R, Hübner U, Schmelzeisen R, Mülhaupt R. Rapid prototyping of scaffolds derived from thermoreversible hydrogels and tailored for applications in tissue engineering. *Biomaterials*. 2002;23(23):4437-4447. doi:10.1016/S0142-9612(02)00139-4.

44. Tasaki S, Maeda C, Kirihara S. Biofluid Flow Simulation of Tissue Engineering Scaffolds with Dendrite Structures. *Adv Bioceram Porous Ceram*. 2013;V:117-121.

45. Kumar GS, Pandithevan P, Ambatti AR. Fractal raster tool paths for layered manufacturing of porous objects. *Virtual Phys Prototyp*. 2009;4(2):91-104. doi:10.1080/17452750802688215.

46. Han L-H, Mapili G, Chen S, Roy K. Projection Microfabrication of Three-Dimensional Scaffolds for Tissue Engineering. *J Manuf Sci Eng*. 2008;130(2):21005. doi:10.1115/1.2823079.

47. Sun C, Fang N, Wu DM, Zhang X. Projection micro-stereolithography using digital micro-mirror dynamic mask. *Sensors Actuators A Phys*. 2005;121(1):113-120. doi:10.1016/j.sna.2004.12.011.

48. Choi JW, Wicker R, Lee SH, Choi KH, Ha CS, Chung I. Fabrication of 3D biocompatible/biodegradable micro-scaffolds using dynamic mask projection microstereolithography. *J Mater Process Technol*. 2009;209(15-16):5494-5503. doi:10.1016/j.jmatprotec.2009.05.004.

49. Ma X, Qu X, Zhu W, Li Y-S, Yuan S, Zhang H, Liu J, Wang P, Lai CSE, Zanella F, Feng G-S, Sheikh F, Chien S, Chen S. Deterministically patterned biomimetic human iPSC-derived hepatic model via rapid 3D bioprinting. *Proc Natl Acad Sci*. 2016:201524510. doi:10.1073/pnas.1524510113.

50. Qu X, Zhu W, Huang S, Li YS, Chien S, Zhang K, Chen S. Relative impact of uniaxial alignment vs. form-induced stress on differentiation of human adipose derived stem cells. *Biomaterials*. 2013;34(38):9812-9818. doi:10.1016/j.biomaterials.2013.09.009.

51. Soman P, Chung PH, Zhang AP, Chen S. Digital microfabrication of user-defined 3D microstructures in cell-laden hydrogels. *Biotechnol Bioeng*. 2013;110(11):3038-3047. doi:10.1002/bit.24957.

52. Lu Y, Mapili G, Suhali G, Chen S, Roy K. A digital micro-mirror device-based system for the microfabrication of complex, spatially patterned tissue engineering scaffolds. *J Biomed Mater Res - Part A*. 2006;77(2):396-405. doi:10.1002/jbm.a.30601.

53. West GB, Brown JH, Enquist BJ. A general model for the origin of allometric scaling laws in biology. *Science (80-)*. 1997;276(5309):122-126. doi:10.1126/science.276.5309.122.

54. Marxen M, Henkelman RM. Branching tree model with fractal vascular resistance explains fractal perfusion heterogeneity. *Am J Physiol Heart Circ Physiol*. 2003;284(5):H1848-57. doi:10.1152/ajpheart.00510.2002.

55. J. Liu, H. H. Hwang, P. Wang, G. Whang SCC. Direct 3D Printing of Cell-laden Constructs in Microfluidic Architectures. *Lab Chip*. 2016;16:1430-1438. doi:10.1039/C6LC00144K.

56. Albro MB, Cigan AD, Nims RJ, Yeroushalmi KJ, Oungoulian SR, Hung CT, Ateshian GA, Angale P, Schumann D, Angele M, Kinner B, Englert C, Hente R, Fuchtmeier B, Nerlich M, Neumann C, … Mooney DJ. Environment-sensitive hydrogels for drug delivery. *Biomaterials*. 2012;41(3):2706-2715. doi:10.1016/j.berh.2014.01.004.

57. Soo SC, Yu KM. Rapid prototyping for self-similarity design. *J Mater Process Technol*. 2003;139(1-3 SPEC):219-225. doi:10.1016/S0924-0136(03)00223-1.

58. Sun W, Lal P. Recent development on computer aided tissue engineering — a review. *Comput Methods Programs Biomed*. 2002;67(2):85-103. doi:10.1016/S0169-2607(01)00116-X.

59. Díaz Lantada A, Pareja Sánchez B, Gómez Murillo C, Urbieta Sotillo J. Fractals in tissue engineering: toward biomimetic cell-culture matrices, microsystems and microstructured implants. *Expert Rev Med Devices*. 2013;10(5):629-648. doi:10.1586/17434440.2013.827506.

60. Liu Y, Hu H. A review on auxetic structures and polymeric materials. *Sci Res Essays*. 2010;5(10):1052-1063.

61. Shan S, Kang SH, Zhao Z, Fang L, Bertoldi K. Design of planar isotropic negative Poisson's ratio structures. *Extrem Mech Lett*. 2015;4:96-102. doi:10.1016/j.eml.2015.05.002.

62. Liu Q. Literature review: materials with negative poisson's ratios and potential applications to Aerospace and Defence. *Aust Gov Dep Def*. 2006:1-47. http://oai.dtic.mil/oai/oai?verb=getRecord&metadataPrefix=html&identifier=ADA460791.

63. Mcmullan PJ, Kumar S, Griffin AC. Textile Fibers Engineered From Molecular Auxetic Polymers. 2004. http://www.ptfe.gatech.edu/faculty/mcmullan/paper.php. Accessed December 8, 2016.

64. Gatt R, Vella Wood M, Gatt A, Zarb F, Formosa C, Azzopardi KM, Casha A, Agius TP, Schembri-Wismayer P, Attard L, Chockalingam N, Grima JN. Negative Poisson's ratios in tendons: An unexpected mechanical response. *Acta Biomater*. 2015;24:201-208. doi:10.1016/j.actbio.2015.06.018.

65. Thorpe CT, Klemt C, Riley GP, Birch HL, Clegg PD, Screen HRC. Helical sub-structures in energy-storing tendons provide a possible mechanism for efficient energy storage and return. *Acta Biomater*. 2013;9(8):7948-7956. doi:10.1016/j.actbio.2013.05.004.

66. Zhang W, Soman P, Meggs K, Qu X, Chen S. Tuning the Poisson's Ratio of Biomaterials for Investigating Cellular Response. *Adv Funct Mater*. 2013;23(25):3226-3232. doi:10.1002/adfm.201202666.

67. Clausen A, Wang F, Jensen JS, Sigmund O, Lewis JA. Topology Optimized Architectures with Programmable Poisson's Ratio over Large Deformations. *Adv Mater*. 2015;27(37):5523-5527. doi:10.1002/adma.201502485.

68. Warner J, Soman P, Zhu W, Tom M, Chen S. Design and 3D Printing of Hydrogel Scaffolds with Fractal Geometries. *ACS Biomater Sci Eng*. 2016:acsbiomaterials.6b00140. doi:10.1021/acsbiomaterials.6b00140.

69. Dymax®, Emergency Overview Biomar BR-7432GI30. 2013:1-7.

70. Cha C, Soman P, Zhu W, Nikkhah M, Camci-Unal G, Chen S, Khademhosseini A. Structural Reinforcement of Cell-Laden Hydrogels with Microfabricated Three Dimensional Scaffolds. *Biomater Sci*. 2014;2(5):703-709. doi:10.1039/C3BM60210A.

71. Ramón-Azcón J, Ahadian S, Obregón R, Camci-Unal G, Ostrovidov S, Hosseini V, Kaji H, Ino K, Shiku H, Khademhosseini A, Matsue T. Gelatin methacrylate as a promising hydrogel for 3D microscale organization and proliferation of dielectrophoretically patterned cells. *Lab Chip*. 2012;12(16):2959. doi:10.1039/c2lc40213k.

72. Chung I-M, Enemchukwu NO, Khaja SD, Murthy N, Mantalaris A, García AJ. Bioadhesive hydrogel microenvironments to modulate epithelial morphogenesis. *Biomaterials*. 2008;29(17):2637-2645. doi:10.1016/j.biomaterials.2008.03.008.

73. Xu R, Manias E, Snyder A, Runt J. New biomedical poly (urethane urea)-layered silicate nanocomposites. *Macromolecules*. 2001;34:337-339. doi:10.1021/ma0013657.

74. Pereira IHL, Ayres E, Patricio PS, Goes AM, Gomide VS, Junior EP, Orefice RL. Photopolymerizable and injectable polyurethanes for biomedical applications: Synthesis and biocompatibility. *Acta Biomater*. 2010;6(8):3056-3066. doi:10.1016/j.actbio.2010.02.036.

75. Tsukada M. Studies on some physical properties and structural characteristics of methyl methacrylate-grafted silk fiber. *J Appl Polym Sci*. 1988;35(4):965-972. doi:10.1002/app.1988.070350411.

76. Martínez-Hernández AL, Santiago-Valtierra AL, Alvarez-Ponce MJ. Chemical modification of keratin biofibres by graft polymerisation of methyl methacrylate using redox initiation. *Mater Res Innov*. 2008;12(4):184-191. doi:10.1179/143307508X362828.

77. Brinkman WT, Nagapudi K, Thomas BS, Chaikof EL. Photo-cross-linking of type I collagen gels in the presence of smooth muscle cells: Mechanical properties, cell viability, and function. *Biomacromolecules*. 2003;4(4):890-895. doi:10.1021/bm0257412.

78. Nichol JW, Koshy ST, Bae H, Hwang CM, Yamanlar S, Khademhosseini A. Cell-laden microengineered gelatin methacrylate hydrogels. *Biomaterials*. 2010;31(21):5536-5544. doi:10.1016/j.biomaterials.2010.03.064.

79. Yue K, Trujillo-de Santiago G, Alvarez MM, Tamayol A, Annabi N, Khademhosseini A. Synthesis, properties, and biomedical applications of gelatin methacryloyl (GelMA) hydrogels. *Biomaterials*. 2015;73:254-271. doi:10.1016/j.biomaterials.2015.08.045.

80. Ibrahim S, Kothapalli CR, Kang QK, Ramamurthi A. Characterization of glycidyl methacrylate - Crosslinked hyaluronan hydrogel scaffolds incorporating elastogenic hyaluronan oligomers. *Acta Biomater*. 2011;7(2):653-665. doi:10.1016/j.actbio.2010.08.006.

81. Ahmed EM. Hydrogel: Preparation, characterization, and applications: A review. *J Adv Res*. 2015;6(2):105-121. doi:10.1016/j.jare.2013.07.006.

82. Marsano E, Gagliardi S, Ghioni F, Bianchi E. Behaviour of gels based on (hydroxypropyl) cellulose methacrylate. *Polymer (Guildf)*. 2000;41(21):7691-7698. doi:10.1016/S0032-3861(00)00142-7.

83. Hoo SP, Loh QL, Yue Z, Fu J, Tan TTY, Choong C, Chan PPY. Preparation of a soft and interconnected macroporous hydroxypropyl cellulose methacrylate scaffold for adipose tissue engineering. *J Mater Chem B*. 2013;1(24):3107. doi:10.1039/c3tb00446e.

84. Khor E, Wu H, Lim LY, Guo CM. Chitin-methacrylate: Preparation, characterization and hydrogel formation. *Materials (Basel)*. 2011;4(10):1728-1746. doi:10.3390/ma4101728.

85. Elizalde-Pena EA, Flores-Ramirez N, Luna-Barcenas G, Vasquez-Garcia SR, Arambula-Villa G, Garcia-Gaitan B, Rutiaga-Quinones JG, Gonzolez-Hernandez J. Synthesis and characterization of chitosan-g-glycidyl methacrylate with methyl methacrylate. *Eur Polym J*. 2007;43(9):3963-3969. doi:10.1016/j.eurpolymj.2007.06.004.

86. Van Den Bulcke AI, Bogdanov B, De Rooze N, Schacht EH, Cornelissen M, Berghmans H. Structural and rheological properties of methacrylamide modified gelatin hydrogels. *Biomacromolecules*. 2000;1(1):31-38. doi:10.1021/bm990017d.

87. Tanaka T. Collapse of gels and the critical endpoint. *Phys Rev Lett*. 1978;40(12):820-823. doi:10.1103/PhysRevLett.40.820.

88. Dušek K, Patterson D. Transition in swollen polymer networks induced by intramolecular condensation. *J Polym Sci A2*. 1968;6(7):1209-1216. doi:10.1002/pol.1968.160060701.

89. Kade MJ, Burke DJ, Hawker CJ. The power of thiol-ene chemistry. *J Polym Sci Part A Polym Chem*. 2010;48(4):743-750. doi:10.1002/pola.23824.

90. Ravichandran R, Sundarrajan S, Venugopal JR, Mukherjee S, Ramakrishna S. Advances in Polymeric Systems for Tissue Engineering and Biomedical Applications. *Macromol Biosci*. 2012;12(3):286-311. doi:10.1002/mabi.201100325.

91. Alperin C, Zandstra PW, Woodhouse KA. Polyurethane films seeded with embryonic stem cell-derived cardiomyocytes for use in cardiac tissue engineering applications. *Biomaterials*. 2005;26(35):7377-7386. doi:10.1016/j.biomaterials.2005.05.064.

92. Kade MJ, Burke DJ, Hawker CJ. The power of thiol-ene chemistry. *J Polym Sci Part A Polym Chem*. 2010;48(4):743-750. doi:10.1002/pola.23824.

93. Kucinska-Lipka J, Gubanska I, Janik H, Sienkiewicz M. Fabrication of polyurethane and polyurethane based composite fibres by the electrospinning technique for soft tissue engineering of cardiovascular system. *Mater Sci Eng C*. 2015;46:166-176. doi:10.1016/j.msec.2014.10.027.

94. Singhal P, Small W, Cosgriff-Hernandez E, Maitland DJ, Wilson TS. Low density biodegradable shape memory polyurethane foams for embolic biomedical applications. *Acta Biomater*. 2014;10(1):67-76. doi:10.1016/j.actbio.2013.09.027.

95. Stevenson AT, Reese LM, Hill TK, McGuire J, Mohs AM, Shekhar R, Bickford LR, Whittington AR. Fabrication and characterization of medical grade polyurethane composite catheters for near-infrared imaging. *Biomaterials*. 2015;54:168-176. doi:10.1016/j.biomaterials.2015.03.020.

96. Richard E, Mead B, Zlotnikov E, Park H, Us NJ, Haders D, Nj S. (12) United States Patent. 2011;2(12). doi:10.1145/634067.634234.

97. Wechsung R. Biomedical Applications of Micro-Nano-Technologies. *Adv Sci Technol*. 2008;57:50-54. doi:10.4028/www.scientific.net/AST.57.50.

98. Panwar H, Raghuram G V., Jain D, Ahirwar AK, Khan S, Jain SK, Pathak N, Banerjee S, Maudar KK, Mishra PK. Cell cycle deregulation by methyl isocyanate: Implications in liver carcinogenesis. *Environ Toxicol*. 2014;29(3):284-297. doi:10.1002/tox.21757.

99. Heederik D, Henneberger PK, Redlich CA. Primary prevention: Exposure reduction, skin exposure and respiratory protection. *Eur Respir Rev*. 2012;21(124):112-124. doi:10.1183/09059180.00005111.

100. Lockey JE, Redlich CA, Streicher R, Pfahles-Hutchens A, Hakkinen PBJ, Ellison GL, Harber P, Utell M, Holland J, Comai A, White M. Isocyanates and Human Health. *J Occup Environ Med*. 2015;57(1):44-51. doi:10.1097/JOM.0000000000000278.

101. Pyo S-H, Persson P, Mollaahmad MA, Sörensen K, Lundmark S, Hatti-Kaul R. Cyclic carbonates as monomers for phosgene- and isocyanate-free polyurethanes and polycarbonates. *Pure Appl Chem*. 2011;84(3):637-661. doi:10.1351/PAC-CON-11-06-14.

102. Sigma-Aldrich CN 5888-33-5. Isobornyl acrylate | Sigma-Aldrich. http://www.sigmaaldrich.com/catalog/product/aldrich/392103?lang=en&region=US&gclid=CjwKEAjwmMS-BRCm5dn51JLbp1wSJACc61tFmsVS1L8h2nrEjA8zf942BSwk4emWuW6FT6XDm2g8qhoCmqzw_wcB. Accessed September 8, 2016.

103. Lombardo VM, Dhulst EA, Leitsch EK, Wilmot N, Heath WH, Gies AP, Miller MD, Torkelson JM, Scheidt KA. Cooperative catalysis of cyclic carbonate ring opening: Application towards non-isocyanate polyurethane materials. *European J Org Chem*. 2015;2015(13):2791-2795. doi:10.1002/ejoc.201500313.

104. Sheng X, Ren G, Qin Y, Chen X, Wang X, Wang F. Quantitative synthesis of bis(cyclic carbonate)s by iron catalyst for non-isocyanate polyurethane synthesis. *Green Chem*. 2015;17(1):373-379. doi:10.1039/C4GC01294A.

105. Kathalewar M, Sabnis A, D'Mello D. Isocyanate free polyurethanes from new CNSL based bis-cyclic carbonate and its application in coatings. *Eur Polym J*. 2014;57:99-108. doi:10.1016/j.eurpolymj.2014.05.008.

106. Hoyle CE, Bowman CN. Thiol-ene click chemistry. *Angew Chemie - Int Ed*. 2010;49(9):1540-1573. doi:10.1002/anie.200903924.

107. Kade MJ, Burke DJ, Hawker CJ. The power of thiol-ene chemistry. *J Polym Sci Part A Polym Chem*. 2010;48(4):743-750. doi:10.1002/pola.23824.

108. Campos LM, Meinel I, Guino RG, Schierhorn M, Gupta N, Stucky GD, Hawker CJ. Highly versatile and robust materials for soft imprint lithography based on thiol-ene click chemistry. *Adv Mater*. 2008;20(19):3728-3733. doi:10.1002/adma.200800330.

109. Boyd DA, Naciri J, Fontana J, Pacardo DB, Shields AR, Verbarg J, Spillmann CM, Ligler FS. Facile fabrication of color tunable film and fiber nanocomposites via thiol click chemistry. *Macromolecules*. 2014;47(2):695-704. doi:10.1021/ma401636e.

110. Riggs BC, Elupula R, Grayson SM, Chrisey DB. Photonic curing of aromatic thiol–ene click dielectric capacitors via inkjet printing. *J Mater Chem A*. 2014;2(41):17380-17386. doi:10.1039/C4TA04030A.

111. Dondoni A, Marra A. Recent applications of thiol–ene coupling as a click process for glycoconjugation. *Chem Soc Rev*. 2012;41(2):573. doi:10.1039/c1cs15157f.

112. Thirumurugan P, Matosiuk D, Jozwiak K. Click chemistry for drug development and diverse chemical-biology applications. *Chem Rev*. 2013;113(7):4905-4979. doi:10.1021/cr200409f.

113. Shih H, Lin CC. Cross-linking and degradation of step-growth hydrogels formed by thiol-ene photoclick chemistry. *Biomacromolecules*. 2012;13(7):2003-2012. doi:10.1021/bm300752j.

114. Pyo SH, Hatti-Kaul R. Chlorine-Free Synthesis of Organic Alkyl Carbonates and Five- and Six-Membered Cyclic Carbonates. *Adv Synth Catal*. 2016;358(5):834-839. doi:10.1002/adsc.201500654.

115. Pyo S-H, Persson P, Mollaahmad MA, Sörensen K, Lundmark S, Hatti-Kaul R. Cyclic carbonates as monomers for phosgene- and isocyanate-free polyurethanes and polycarbonates. *Pure Appl Chem*. 2011;84(3):637-661. doi:10.1351/PAC-CON-11-06-14.

116. Belfield KD, Yao S, Morales AR, Hales JM, Hagan DJ, Van Stryland EW, Chapela VM, Percino J. Synthesis and characterization of novel rigid two-photon absorbing polymers. *Polym Adv Technol*. 2005;16(2-3):150-155. doi:10.1002/pat.550.

117. Ochiai B, Nakayama JI, Mashiko M, Kaneko Y, Nagasawa T, Endo T. Synthesis and crosslinking reaction of poly(hydroxyurethane) bearing a secondary amine structure in the main chain. *J Polym Sci Part A Polym Chem*. 2005;43(23):5899-5905. doi:10.1002/pola.21078.

118. Bähr M, Mülhaupt R. Linseed and soybean oil-based polyurethanes prepared via the non-isocyanate route and catalytic carbon dioxide conversion. *Green Chem*. 2012;14(2):483. doi:10.1039/c2gc16230j.

119. Boyd DA, Naciri J, Fontana J, Pacardo DB, Shields AR, Verbarg J, Spillmann CM, Ligler FS. Facile Fabrication of Color Tunable Film and Fiber Nanocomposites via Thiol Click Chemistry. *Macromolecules*. 2014;47(2):695-704. doi:10.1021/ma401636e.

120. Senyurt AF, Wei H, Phillips B, Cole M, Nazarenko S, Hoyle CE, Piland SG, Gould TE. Physical and mechanical properties of photopolymerized thiol-ene/acrylates. *Macromolecules*. 2006;39(19):6315-6317. doi:10.1021/ma060507f.

121. Li Q, Zhou H, Wicks DA, Hoyle CE. Thiourethane-based thiol-ene high Tg networks: Preparation, thermal, mechanical, and physical properties. *J Polym Sci Part A Polym Chem*. 2007;45(22):5103-5111. doi:10.1002/pola.22252.

122. DeForest CA, Tirrell DA. A photoreversible protein-patterning approach for guiding stem cell fate in three-dimensional gels. *Nat Mater*. 2015;14(5):523-531. doi:10.1038/nmat4219.

123. Matsunaga T, Hieda K, Nikaido O. Wavelength Dependent Formation of Thymine Dimers and (6-4) Photoproducts in DNA by Monochromatic Ultraviolet Light Ranging from 150 TO 365 nm. *Photochem Photobiol*. 1991;54(3):403-410. doi:10.1111/j.1751-1097.1991.tb02034.x.

124. Freeman SE, Hacham H, Gange RW, Maytum DJ, Sutherland JC, Sutherland BM. Wavelength dependence of pyrimidine dimer formation in DNA of human skin irradiated in situ with ultraviolet light. *Proc Natl Acad Sci U S A*. 1989;86(14):5605-5609.

125. Yeh SR, Falvey DE. Model studies of DNA photorepair: radical anion cleavage of thymine dimers probed by nanosecond laser spectroscopy. *J Am Chem Soc*. 1991;113(22):8557-8558. doi:10.1021/ja00022a072.

126. Washington MT, Johnson RE, Prakash S, Prakash L. Accuracy of thymine-thymine dimer bypass by Saccharomyces cerevisiae DNA polymerase eta. *Proc Natl Acad Sci U S A*. 2000;97(7):3094-3099. doi:10.1073/pnas.050491997.

127. Kizilel R, Demir E, Azizoglu S, Asimgi H, Kavakli IH, Kizilel S. Investigation of Real-Time Photorepair Activity on DNA via Surface Plasmon Resonance. *PLoS One*. 2012;7(8). doi:10.1371/journal.pone.0044392.

128. Selby CP, Sancar A. A cryptochrome/photolyase class of enzymes with single-stranded DNA-specific photolyase activity. *Proc Natl Acad Sci U S A*. 2006;103(47):17696-17700. doi:10.1073/pnas.0607993103.

129. Chen Y, Kushner AM, Williams GA, Guan Z. Multiphase design of autonomic self-healing thermoplastic elastomers. *Nat Chem*. 2012;4(6):467-472. doi:10.1038/nchem.1314.

130. Hentschel J, Kushner AM, Ziller J, Guan Z. Supporting InformationSelf-Healing Supramolecular Block Copolymers. 2012:10713-10717. doi:10.1002/ange.201204840.

131. Ara??jo M, Van Vlierberghe S, Feiteira J, Graulus GJ, Van Tittelboom K, Martins JC, Dubruel P, De Belie N. Cross-linkable polyethers as healing/sealing agents for self-healing of cementitious materials. *Mater Des*. 2016;98:215-222. doi:10.1016/j.matdes.2016.03.005.

132. Rothemund PWK. Folding DNA to create nanoscale shapes and patterns. *Nature*. 2006;440(7082):297-302. doi:10.1038/nature04586.

133. Mizuno N, Baxa U, Steven AC. Structural dependence of HET-s amyloid fibril infectivity assessed by cryoelectron microscopy. *Proc Natl Acad Sci U S A*. 2011;108(8):3252-3257. doi:10.1073/pnas.1011342108.

134. Song Y, Takahashi T, Kim S, Heaney YC, Warner JJ, Chen S, Heller MJ. A Programmable DNA Double Write Material – Synergy of Photolithography and Self-Assembly Nanofabrication. 2016. doi:10.1021/acsami.6b11361.

135. Feng L, Romulus J, Li M, Sha R, Royer J, Wu K-T, Xu Q, Seeman NC, Weck M, Chaikin P. Cinnamate-based DNA photolithography. *Nat Mater*. 2013;12(8):747-753. doi:10.1038/nmat3645.

136. He D, He X, Wang K, Cao J, Zhao Y. A Light-Responsive Reversible Molecule-Gated System Using Thymine-Modified Mesoporous Silica Nanoparticles. doi:10.1021/la2047504.

137. Worthington EN, Kavakli IH, Berrocal-Tito G, Bondo BE, Sancar A. Purification and characterization of three members of the photolyase/cryptochrome family blue-light photoreceptors from vibrio cholerae. *J Biol Chem*. 2003;278(40):39143-39154. doi:10.1074/jbc.M305792200.

138. Sosic A, Meneghello A, Cretaio E, Gatto B. Human thrombin detection through a sandwich aptamer microarray: Interaction analysis in solution and in solid phase. *Sensors*. 2011;11(10):9426-9441. doi:10.3390/s111009426.

139. Chang Y-C, Yang C-Y, Sun R-L, Cheng Y-F, Kao W-C, Yang P-C. Rapid single cell detection of Staphylococcus aureus by aptamer-conjugated gold nanoparticles. *Sci Rep*. 2013;3:1863. doi:10.1038/srep01863.

140. Chang YM, Donovan MJ, Tan W. Using aptamers for cancer biomarker discovery. *J Nucleic Acids*. 2013;2013. doi:10.1155/2013/817350.

141. Cho H, Baker BR, Wachsmann-Hogiu S, Pagba C V., Laurence TA, Lane SM, Lee LP, Tok JB-H. Aptamer-Based SERRS Sensor for Thrombin Detection. *Nano Lett*. 2008;8(12):4386-4390. doi:10.1021/nl802245w.